ADVANCED HEALTHCARE MATERIALS
www.advhealthmat.de

# Effect of Polymer and Cell Membrane Coatings on Theranostic Applications of Nanoparticles: A Review

*Bahareh Rezaei, Asma Harun, Xian Wu, Poornima Ramesh Iyer, Shahriar Mostufa, Stefano Ciannella, Ioannis H. Karampelas, Jeffrey Chalmers, Indrajit Srivastava,* Jenifer Gómez-Pastora,* and Kai Wu**

**The recent decade has witnessed a remarkable surge in the field of nanoparticles, from their synthesis, characterization, and functionalization to diverse applications. At the nanoscale, these particles exhibit distinct physicochemical properties compared to their bulk counterparts, enabling a multitude of applications spanning energy, catalysis, environmental remediation, biomedicine, and beyond. This review focuses on specific nanoparticle categories, including magnetic, gold, silver, and quantum dots (QDs), as well as hybrid variants, specifically tailored for biomedical applications. A comprehensive review and comparison of prevalent chemical, physical, and biological synthesis methods are presented. To enhance biocompatibility and colloidal stability, and facilitate surface modification and cargo/agent loading, nanoparticle surfaces are coated with different synthetic polymers and very recently, cell membrane coatings. The utilization of polymer- or cell membrane-coated nanoparticles opens a wide variety of biomedical applications such as magnetic resonance imaging (MRI), hyperthermia, photothermia, sample enrichment, bioassays, drug delivery, etc. With this review, the goal is to provide a comprehensive toolbox of insights into polymer or cell membrane-coated nanoparticles and their biomedical applications, while also addressing the challenges involved in translating such nanoparticles from laboratory benchtops to in vitro and in vivo applications. Furthermore, perspectives on future trends and developments in this rapidly evolving domain are provided.**

## 1. Introduction

Progress and development in micro- and nanotechnologies have enabled the fabrication of advanced materials at the nanoscale level with outstanding properties.[1–7] Nanoparticles usually encompass materials with sizes below 100 nm, and often present enhanced features in comparison to their bulk material counterparts.[8–11] For instance, nanoparticles have a very high surface-area-to-volume ratio due to their small size, and size-dependent physicochemical attributes, making them particularly versatile, efficient, and reactive in comparison to the same material at the macroscopic level. Moreover, nanoparticles benefit from unique physical, chemical, electrical, mechanical, thermal, optical, and magnetic properties that have allowed the development of novel, highly efficient processes that take advantage of these outstanding properties.[12–15] Different fields, including medicine, biology, chemistry, physics, and engineering have exploited the use of nanoparticles for a wide range of applications, spanning from cancer treatment to energy harvesting, as well as

B. Rezaei, S. Mostufa, K. Wu
Department of Electrical and Computer Engineering
Texas Tech University
Lubbock, TX 79409, United States
E-mail: kai.wu@ttu.edu

A. Harun, I. Srivastava
Department of Mechanical Engineering
Texas Tech University
Lubbock, TX 79409, United States
E-mail: indrajit.srivastava@ttu.edu

The ORCID identification number(s) for the author(s) of this article can be found under https://doi.org/10.1002/adhm.202401213

DOI: 10.1002/adhm.202401213

A. Harun, I. Srivastava
Texas Center for Comparative Cancer Research (TC3R)
Amarillo, Texas 79106, United States

X. Wu, P. R. Iyer, J. Chalmers
Department of Chemical and Biomolecular Engineering
The Ohio State University
Columbus, OH 43210, United States

S. Ciannella, J. Gómez-Pastora
Department of Chemical Engineering
Texas Tech University
Lubbock, TX 79409, United States
E-mail: jenifer.gomez@ttu.edu

I. H. Karampelas
Nemak USA, Inc.
Sheboygan, WI 53081, United States

 

manufacturing, and environmental applications like pollutant remediation.[16–19] Notably, the promising role of these materials in several biomedical scenarios has accelerated the progress in the development of multifunctional nanoparticles for a variety of applications including imaging, therapy, diagnosis, sensing, etc.[19,20]

To bring these technologies a step forward, nanomaterials with controlled properties and characteristics are required so that reproducible processes can be designed, especially for biomedical applications, as materials with controlled size distributions, biocompatibility, chemical stability, and specially designed surface chemistries are demanded.[21–26] To achieve these desired properties, nanoparticles are generally coated with a layer of organic materials, and polymeric coatings have proven to enhance the bare nanoparticle's biocompatibility, colloidal stability, as well as their physicochemical properties, in addition to providing a functionalizable surface that can be conjugated with proteins, enzymes, antibodies, drugs, etc.[27] Since the core and coating material's characteristics can greatly affect the physical behavior, chemical properties, and performance of the nanoscale composites, it is crucial to monitor the synthesis details of the material accurately and precisely, including their surface functionalization, as well as their application to biological systems.

The synthesis of polymer-coated nanoparticles is a research topic that is gaining increased attention in the field, and multiple synthesis techniques are nowadays available, each with its advantages and disadvantages.[28,29] The "top-down" and "bottom-up" approaches have been developed, which differ in the size of the starting materials in comparison to the size of the final, synthesized product. These methods are also divided into three groups: chemical, physical, and biological routes. While chemical and physical routes have been explored for several decades, they suffer from several limitations that newer biological approaches are trying to overcome. Concerning the application of these nanomaterials in biomedical fields, novel processes such as cancer diagnosis, cancer treatment via drug delivery or magnetic hyperthermia, and sensing of biomolecules in biological fluids for disease diagnosis, have integrated polymeric nanomaterials to increase their efficiency while reducing unwanted side effects.[27]

This review summarizes recent advancements in the synthesis and application of polymer-coated gold nanoparticles (AuNPs) and magnetic nanoparticles (MNPs) in biomedicine, highlighting their roles in theranostic applications. MNPs enable targeted drug delivery via magnetic manipulation and provide high-resolution medical imaging. They are also essential for hyperthermia applications with alternating magnetic fields due to their effective heating rates. In contrast, AuNPs, with their strong optical properties, facilitate imaging techniques such as photoacoustic imaging and surface-enhanced Raman scattering and serve as carriers for therapeutic payloads. Both MNPs and AuNPs exhibit biocompatibility, ensuring safe use in vivo, and their versatile surface chemistry allows precise functionalization for targeted delivery and imaging. It is structured as shown in **Figure 1**. After this brief introduction, in Section 2, we provide an overview of the different methods for the synthesis of these nanomaterials, discussing their main advantages and drawbacks. Specifically, magnetic nanoparticles, gold nanoparticles, and hybrid materials are discussed, and their main synthesis routes are showcased. In Section 3, we review common polymeric coatings that have been used to encapsulate nanomaterials to protect their inner core as well as to enhance the chemical stability of the nanoparticle, its biocompatibility, and to functionalize its surface. Section 4 provides an overview of different applications of these polymer-coated nanomaterials, including medical imaging, hyperthermia, photothermal/hyperthermia cancer treatment, drug delivery, magnetic bioseparations, and magnetic bioassays. Finally, we present the main challenges of these materials for future clinical applications as well as a discussion on their biosafety in Section 5 before concluding in Section 6 with a summary of this work along with the future directions of these technologies that will facilitate their clinical implementation.

## 2. Synthesis Methods of Nanoparticles

### 2.1. Magnetic Nanoparticles (MNPs)

MNPs are composed of magnetic elements such as iron, cobalt, nickel, metal alloys (e.g., CoPt, FePt), metal oxides, or ferrites, all of which exhibit ferromagnetic or superparamagnetic properties.[30] Due to their high magnetic saturation, small size, unique characteristics, high surface area, ease of surface modification, and processability, MNPs are typically regarded as highly effective therapeutic treatments and diagnostic tools in biomedical applications. Targeted delivery of drugs or therapeutic agents, transfection of different viral/non-viral vectors and nucleic acids (called magnetofection), magnetic separation,[31,32] diagnostic imaging as contrast agents,[33] tissue engineering,[34,35] and various biosensing applications[10,36] are just a few of the uses for these MNPs. For therapeutic purposes, MNPs can be directed to target sites using an external magnetic field. They are utilized in cancer therapy to induce hyperthermia and to deliver various medications and bioactive substances into cells.

The synthesis method and design of MNPs for use in biomedical applications are challenging. At each stage of the synthesis method, numerous elements must be considered.[37] Although these elements can be adjusted in the early stages of design, they have the potential to significantly alter the anticipated result. Synthesis of MNPs is a multi-step procedure that needs to be done carefully to produce the desired results. It is one of the most significant obstacles in almost all applications since it defines the particles' size, shape, and surface chemistry as well as their magnetic properties. There are three primary ways for synthesizing MNPs: a) physical, b) chemical, and c) biological methods, as shown in **Figure 2**. The physical procedures are based on the "top-down" method, which starts with bulk material and uses it to create MNPs. In contrast, a "bottom-up" approach is used in chemical and biological processes to mix atoms and molecules to create different sizes of MNPs.[38–40]

The "top-down" method involves grinding bulky magnetic materials in a high-energy ball mill until the required nanoscale sizes are reached. This method's capacity to obtain a large number of particles in a single batch is its advantage. Its inability to control the size uniformity and the shape of the particles, which is a crucial component for biomedical applications, is a disadvantage. In contrast, a ferrous ($Fe^{2+}$) or ferric ($Fe^{3+}$) ion salt could be the starting point for the "bottom-up" method. To grow the particles to the necessary hydrodynamic sizes, the salt is subjected to an additional chemical process that promotes seed growth. Due

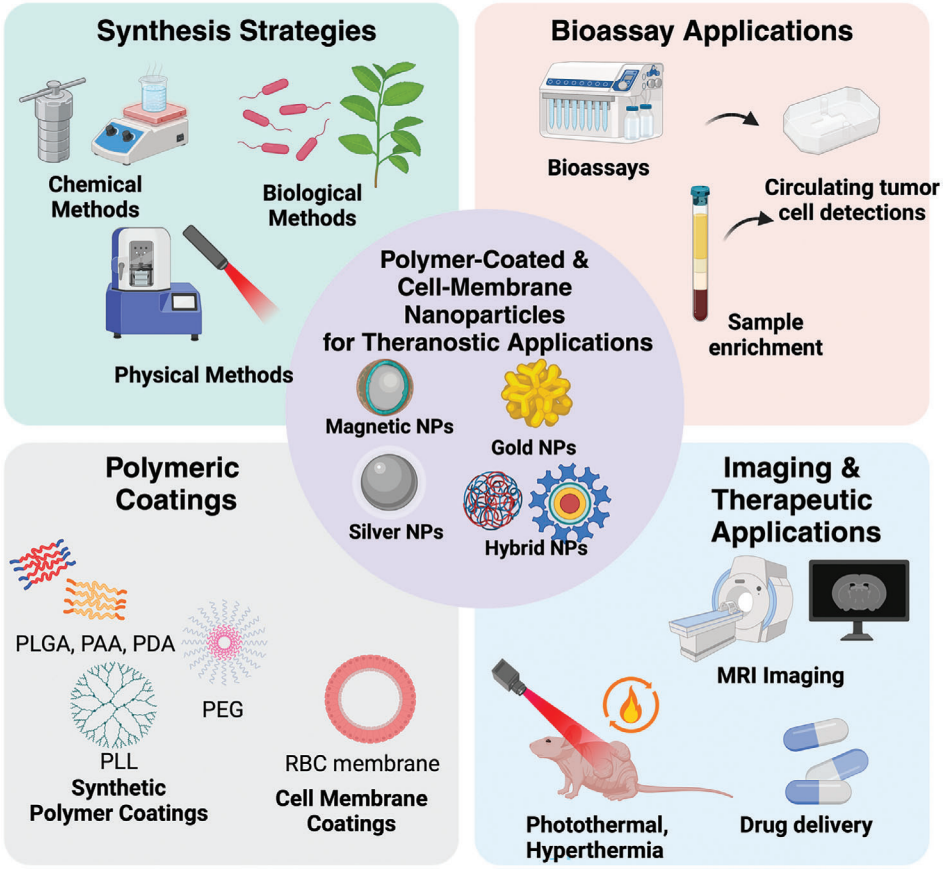


**Figure 1.** Illustration of contents covered in this review which provides an overview of the diverse synthesis and polymer coating options utilized for creating polymer-coated nanoparticles. These nanoparticles find applications in MRI, photothermal therapy, bioassays, and drug delivery. Original figure prepared by the authors, created with Biorender.com.

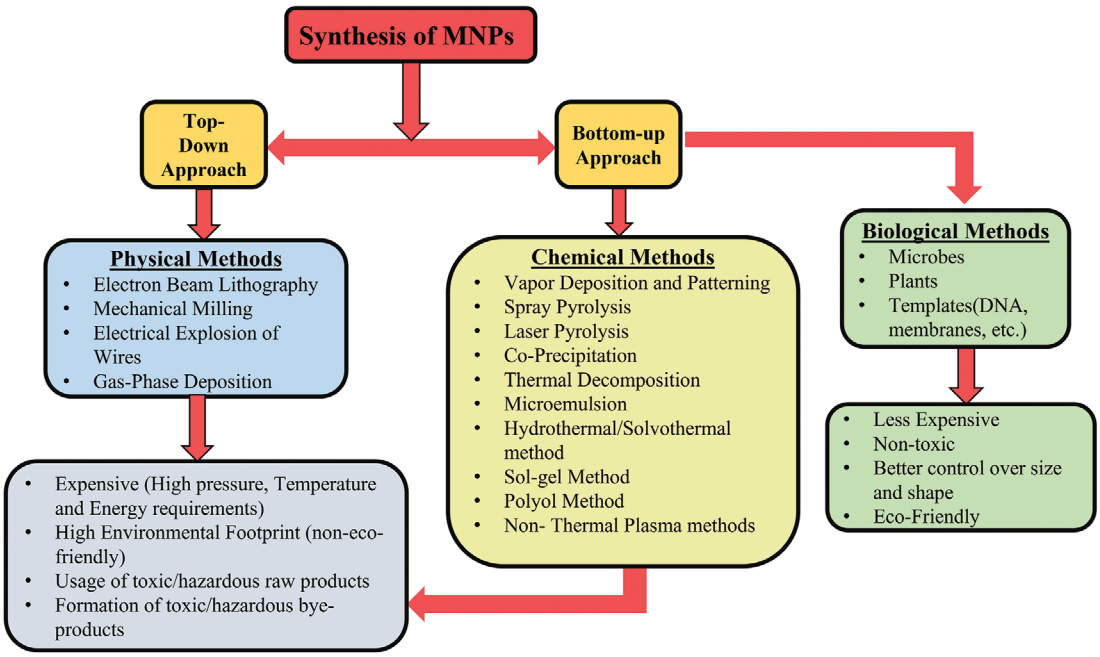


**Figure 2.** Classification of synthesis methods for MNPs and their key features. Figure adapted from ref. [38] under a Creative Commons license CC BY 4.0.

**Table 1.** Comparison of different wet-chemical synthesis methods for MNPs.

| Synthesis method | Solvent | Reaction temperature | Advantages | Disadvantages |
|---|---|---|---|---|
| Co-precipitation | Water | Ambient temperature | Simple, large quantity | No good shape control, wide size distribution, impurities, time consuming |
| Hydrothermal | Water/ethanol | 150-250 °C | Very narrow size distribution and very good shape control, good crystallinity | Marginal yield, requirement of high temperature, and pressure |
| Sol-gel | Water | Ambient conditions | Desired shape and length, useful for making hybrid MNPs, highly pure, good crystallinity | Products usually contain sol–gel matrix components at their surfaces, longer time, toxic organic solvents |
| Microemulsion | Organic compound | Ambient conditions | Narrow size distribution, thermodynamically stable | Low yield |
| Thermal decomposition | Organic compound | 100–330 °C | Narrow size distribution, good shape control, and highly scalable | Requirement of high temperature and inert atmosphere, toxic solvents |

to their complete process control, uniform size, and minimal energy loss, these wet approaches have the potential to be more cost-effective and efficient.[40] However, the request for ecologically friendly, low-cost, nontoxic, high-yield methods for the synthesis of MNPs has increased, and as a result, the biological methods for producing MNPs have gained significance. For the synthesis of MNPs, a wide range of biological resources found in nature, such as bacteria, fungi, yeast, plants, and plant products, could be used. However, there are still issues with raw material extraction, reaction time, and finished product quality.[41] In this section, we will review the chemical, physical, and biological methods for the synthesis of MNPs.

### *2.1.1. Chemical Methods*

Chemical synthesis methods use precursors in the solution phase and appropriate experimental conditions to handle chemical reactions. Since each chemical synthesis technique is unique, there is no universal guideline for these kinds of synthesis techniques.[42] Among diverse chemical techniques developed for magnetic nanomaterial synthesis, we herein highlight the co-precipitation, hydrothermal, sol-gel reactions, microemulsion, and thermal decomposition along with their specific advantages and disadvantages (see **Table 1**).

*Co-Precipitation*: Precipitation from solutions stands as one of the earliest methods for synthesizing nanoscale materials. This process involves dissolving metal precursors in a solvent, typically water, followed by the addition of a precipitating agent to induce the formation of insoluble solids. One of the key advantages of precipitation processes lies in their capacity to yield large quantities of nanoparticles.[43] Most commonly utilized to synthesize MNPs, co-precipitation has also been utilized to produce various metal oxide nanoparticles, including ZnO, $SnO_2$, $Y_2O_3$, and $CeO_2$.[44–46] Moreover, this method is characterized by its simplicity, widespread applicability, cost-effectiveness, and ease of implementation. For example, when synthesizing $Fe_3O_4$ and $\gamma$-$Fe_2O_3$, one could start with a standard 1:2 molar ratio of ferric/ferrous salt solution in basic-pH at either room temperature or elevated temperatures. To prevent oxidation and preserve the magnetic properties of nanoparticles, this process benefits from an inert gas environment. The size, morphology, and composition of the resulting MNPs are profoundly influenced by factors such as the ferric/ferrous ratio, the type of salt employed (e.g., chlorides, sulfates, or nitrates), reaction temperature, pH level, and ionic strength of the medium. If the synthesis conditions are well controlled, the quality of MNPs is completely repeatable.[47] The annealing temperature also plays an important role in the magnetic properties of these MNPs, and a temperature in the range of 900–1000 °C leads to the most promising results.[38] Additionally, the resulting iron oxide MNPs have a high amount of hydroxyl groups (-OH) on their surfaces and show good colloidal stability in water.[48]

The co-precipitation process is illustrated in **Figure 3A**, with the reaction represented as follows[49]:

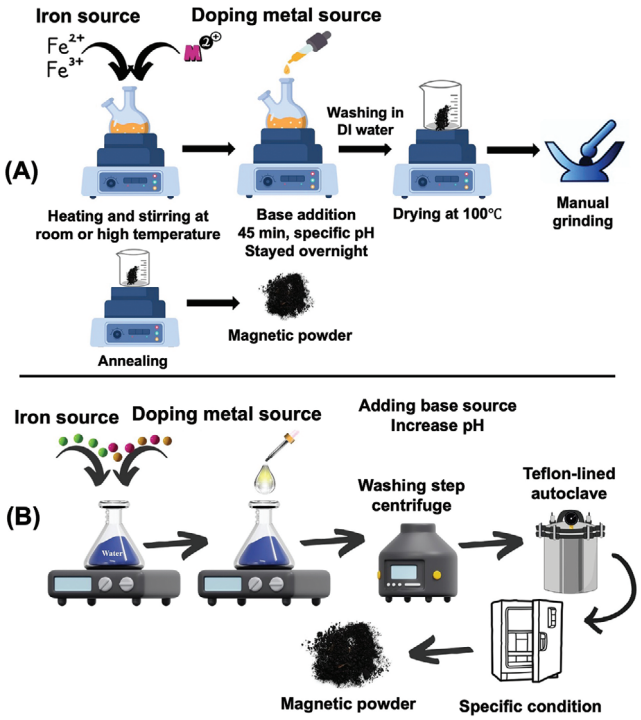


**Figure 3.** Schematic illustrations of MNPs synthesized by (A) co-precipitation and (B) hydrothermal methods. Original figure prepared by the authors.

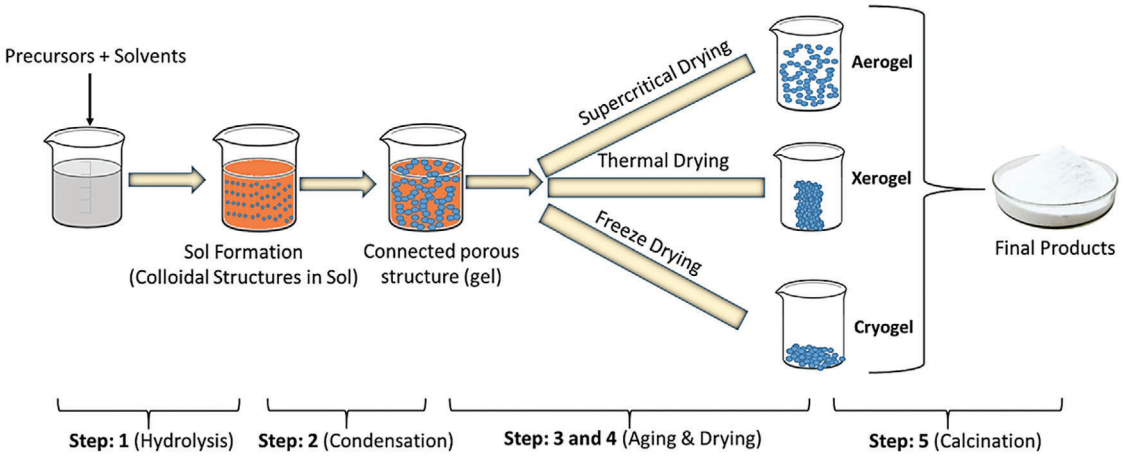


**Figure 4.** Schematic illustration of MNPs synthesized by the sol-gel method. Reproduced with permission.[55] Copyright 2020, Springer Science Business Media, LLC, part of Springer Nature.

$$Fe^{2+}(aq) + Fe^{3+}(aq) + 8\,OH^{-}(aq) \rightarrow Fe_3O_4(s) + 4\,H_2O(aq) \quad (1)$$

*Hydrothermal*: The hydrothermal approach involves the combination of specific concentrations of di-metal salt solutions with an aqueous suspension, followed by placement in a Teflon-lined autoclave to facilitate chemical processes, as shown in Figure 3B. The hydrothermal reactions occur in high-pressure reactors, capable of achieving temperatures above 150 °C and pressures over 2000 psi.[33,39,50] Within the Teflon-lined autoclave, the hydrolysis of ferrous ions leads to the formation of hydroxide intermediates ($Fe(OH)_n$), which subsequently dehydrate to produce the final iron oxide phase. The kinetics of hydrolysis reactions are accelerated at supercritical temperatures, where water serves as a reactant. Increased temperatures result in lower viscosity of the water, enhancing solubility and mobility of most ionic species. In hydrothermal conditions, MNPs can be synthesized through the neutralization of mixed metal hydroxides or via hydrolysis and dehydration (refer to Equations 2 and 3).[51] Except for the iron (II) salts employed in the second procedure, these two approaches are highly similar.[39]

$$\text{(Hydrolysis)}\ M(NO)_x(aq) + xH_2O \rightarrow M(NO)_x(s) + xHNO \quad (2)$$

$$\text{(Dehydration)}\ M(OH)_x(s) \rightarrow M(O)_{x/2}(s) + x/2H_2O \quad (3)$$

The hydrothermal process yields enhanced crystalline structures, such as magnetite nanorods and nanospheres, with a low cost of raw materials and simple operation. Moreover, this method enables the production of MNPs with a narrow size distribution and without the necessity for chemical solvents.[33,39,50] Additionally, in hydrothermal processes, parameters such as temperature, time, solvent type, reactant concentration, and stoichiometry affect the size and morphology of the product, while the phase purity of nanoparticles is affected by pH and precursor material reaction conditions.[50] This method has been utilized to synthesize metal (Au, Ag, Pd, In, Pt, Si, Ge, Cu), metal oxide ($TiO_2$, ZnO, $Fe_2O_3$, $Fe_3O_4$, $Co_3O_4$, NiO, $ZrO_2$, $LiCoO_2$ $CeO_2$, CuO, $Al_2O_3$), metal chalcogenide and sulfides (ZnSe, CdSe, CdS, PbS, InS, $Ag_2S$, $MoS_2$), and carbon nanotubes.[52,53]

*Sol–Gel*: The sol–gel process is a highly distinctive wet chemical technique used in many fields to synthesize cutting-edge materials.[54] It is one of the most-studied synthetic methods for preparing superior MNPs, metal oxide nanoparticles (e.g., $TiO_2$, ZnO, $SnO_2$, $WO_3$), silica nanoparticles, metal chalcogenide quantum dots, metal nitride, carbide nanostructures, etc. This method allows for precise control over the texture and surface characteristics of these materials.[55–57] This process first produces a "sol" of nanosized particles by hydroxylating and condensing chemical precursors in solution. Then, the "sol" is "gelled" or dried by a chemical reaction or solvent removal to create a three-dimensional metal oxide network, as shown in **Figure 4**. The structure formed during the "sol" stage of the sol-gel process has a significant impact on the gel's properties. Furthermore, the strengthening of the "gel" and the purification and stability of the "sol" can be accomplished.

Although water is typically used as a solvent, an acid or base can also hydrolyze the precursors. However, the percentage of water has a significant impact on the gel formation, with a higher water percentage favoring the creation of a higher ratio of bridging to nonbridging oxygens, which results in a more polymerized and branched structure at the condensation stage.[55,58] The general chemical reaction for the hydrolysis and condensation process is given as:

$$\text{(Hydrolysis)}\ M - OR + H_2O \rightarrow M - OH + R - OH \quad (4)$$

where M = metal, R = alkyl group ($C_nH_{2n+1}$).

$$\text{(Condensation)}\ M - OH + XO - M \rightarrow M - O - M + X - OH \quad (5)$$

where X = H or alkyl Group ($C_nH_{2n+1}$).

*Microemulsion*: Microemulsions are composed of at least three components: a polar phase (often water), a nonpolar phase (typically oil), and an emulsifier or surfactant. Emulsifiers and

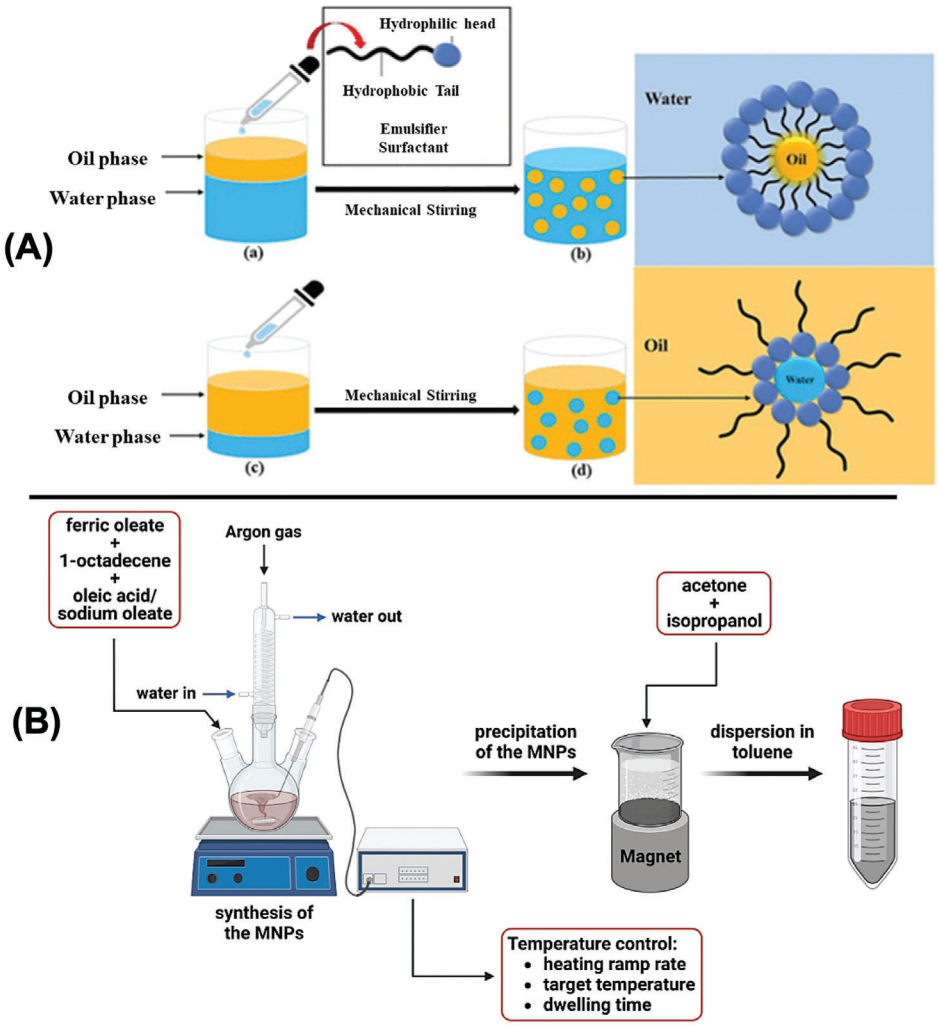


**Figure 5.** Schematic illustrations of MNPs synthesized by A) microemulsion and B) thermal decomposition methods. A) Reproduced with permission,[62] under a Creative Commons license CC BY-NC-ND 4.0. B) Reproduced with permission,[63] under a Creative Commons license CC BY 4.0.

surfactants are isotropic, macroscopically homogeneous, and thermodynamically stable solutions that are distinguished by their ability to solubilize both water and oil components, huge interfacial area, and ultra-low interfacial tension.[59] The polar and non-polar domains are separated on a microscopic level by an interfacial film formed by the surfactant molecules. This interfacial layer creates a variety of microstructures, from water droplets scattered in a continuous oil phase to droplets of oil dispersed in a continuous water phase over a "sponge" phase. Thus, different microemulsion forms including water-in-oil (W/O) and oil-in-water (O/W) are recognized.[60] The W/O microemulsions are a new and great reaction medium for creating nanoparticles because, as **Figure** 5A illustrates, the surfactant monolayer's steric barrier limits the growth of precipitated particles and prevents inter-grain coagulation.[61] In contrast, O/W that exhibit thermodynamic stability, known as microemulsions, have droplet sizes between 10 nm and 100 nm, which are smaller than those of typical emulsions (macroemulsions: 1 μm – 100 μm) and mini-emulsions (50 nm – 500 nm).

Short-chain alcohols (e.g., n-pentanol) and other surfactants, along with significant concentrations of anionic or cationic surfactants (>10–20% in the formulation or at similar levels as the monomer), are used to generate a stable microemulsion. Since the elasticity of the surfactant film depends on the type of surfactant, thermodynamic conditions, and additive presence, the size and shape of the dispersed nanodroplets are primarily determined by the curvature free energy, which is estimated using the elastic constant and the curvatures of the surfactant film. It is known that nanodroplets are templates for nanoparticles. Therefore, the size of the dispersed nanoparticles depends directly on the size of the nanodroplets, which in turn depends on the kind, quantity, and thermodynamic conditions of the surfactant. As a result, by adjusting the surfactant type, concentration, and water-to-surfactant molar ratio (while maintaining the same surfactant), nanoparticles can be customized.[61] This technique can be used to synthesize polymeric nanoparticles, lipid nanoparticles, biopolymer nanoparticles (e.g., chitosan, alginate, cellulose), and metal nanoparticles (e.g., Fe, Pt, Cd, Pd, Ag, Cu, Ni, Au).[64–66]

*Thermal Decomposition*: The process of using heat to break down a compound's chemical bonds is known as thermal decomposition. This method is widely used to synthesize a variety of nanoparticles, including metal nanoparticles like Au[67] and Ag,[68] metal oxide nanoparticles such as iron oxide (e.g., $Fe_3O_4$, $Fe_2O_3$),[69] zinc oxide (ZnO),[70] and titanium dioxide ($TiO_2$),[71] and metal sulfide nanoparticles like cadmium sulfide (CdS).[72] It also produces bimetallic and alloy nanoparticles, such as gold-silver (Au-Ag) and platinum-nickel (Pt-Ni),[73] and quantum dots.[74] The synthesis of small-sized, monodispersed MNPs via thermal decomposition involves the controlled, heating-induced decomposition of organometallic compounds within organic solvents characterized by high boiling points, typically conducted in the presence of stabilizing agents such as surfactants, as shown in Figure 5B. However, it is a clever way to synthesize nanoparticles with the possibility of making varied-sized products from the same precursor solution.[75] Various organometallic precursors are utilized, including those derived from acetylketonates, N-nitrosophenylhydroxylamine (cupferronates), and carbonyls, among others, featuring metallic centers such as $Fe^{2+/3+}$, $Mn^{2+/3+}$, $Co^{2+/3+}$, and $Ni^{2+/3+}$. Stabilizing agents such as fatty acids, oleic acids, and hexadecylamine are commonly employed to control the size, shape, and stability of the resulting nanoparticles. This methodology enables the synthesis of MNPs with precisely tuned characteristics suitable for a wide range of applications spanning from catalysis to biomedicine.[76,77]

The size distributions of MNPs synthesized at higher temperatures are often more uniform. Separating the nucleation and growth phases results in highly crystalline, monodispersed MNPs with a narrow size distribution, which is one of the main benefits of this method over co-precipitation.[4,43,78,79] The temperature, reaction time, and aging period are some of the variables that affect how precisely the size and morphological distribution of the nanoparticles are controlled. Accurate control over the size and size distribution, as well as the structure and magnetic characteristics of the resultant MNPs, can be achieved by adjusting the annealing temperatures used throughout the synthesis process.[4]

### 2.1.2. Physical Methods

In this section, we provide an overview of several physical methods commonly employed for the synthesis of MNPs. While each synthesis method has a rich literature base that could yield comprehensive review studies, our focus here is to offer a brief discussion of their main characteristics. The physical methods usually follow a "top-down" approach wherein the synthesis commences with a bulk, larger material and gradually diminishes to yield nanoparticles. However, there are instances of physical methods that follow a "bottom-up" approach, such as the gas-phase condensation and self-assembly processes.[80,81] Physical methods are often favored for the large-scale production of nanoparticles due to their simplicity. However, these methods come with significant drawbacks such as fairly dispersed particle size distribution and the use of time-consuming and costly technologies, which pose major limitations in the production of MNPs.[30,82] Among the physical synthesis techniques, several approaches including but not limited to ball milling, laser evaporation (or ablation), and gas-phase deposition are highlighted in this section.

Briefly, ball milling involves the mechanical grinding of precursor materials in the presence of milling media, enabling the production of MNPs with controlled sizes.[83] However, it is hard to have fine control over the nanoparticles' shapes obtained via this mechanical approach.[84] Laser ablation is a method that produces MNPs through high-energy laser pulses applied over the surface of a bulk material, which generates nanoparticles by nucleation of laser-vaporized species in a viscous media (gas or liquid).[85] Gas-phase synthesis techniques involve the nucleation and growth of MNPs from precursor vapors in a controlled atmosphere.[86]

*Ball/Mechanical Milling*: Ball milling presents a convenient and straightforward approach to synthesizing powdered MNPs. It can be found denoted in the literature as mechanical alloying, attrition, ultrafine grinding, or nanosizing.[82] The ball milling technique allows for the fabrication of various nanomaterials, including metallic, multi-metallic, alloyed, ceramic, oxide, sulfide, and carbonate nanocomposites.[87] This high-throughput fabrication method is commonly employed to produce different types of materials based on various precursors, leading to the development of metallic granular alloys. The mechanical grinding process, initially developed in 1970, involves enclosing raw materials within a small hollow cylindrical jar filled with steel balls as the grinding material.[84] Continuous collisions between the steel balls and solid materials impart kinetic energy, resulting in the formation of nano/micro-sized powder. Key parameters such as ball-to-powder ratio, ball size, milling speed, and milling time significantly influence the formation process of nano/micro-size crystals.[88]

As depicted in **Figure 6A**, a typical ball mill comprises a hollow cylindrical chamber filled with balls of varying dimensions, with container and ball materials chosen based on the characteristics of the materials to be milled. To prevent reactions with the container walls, liners based on manganese, steel, or rubber material can be utilized.[88] In reactive mechanochemical milling, low vacuum or specialized gases such as argon, hydrogen, and nitrogen may be deployed during the milling process. Various ball mill types, including attrition (Figure 6B), low-energy tumbling mills (Figure 6C), planetary (Figure 6D), and vibratory (Figure 6E), offer flexibility in handling variable temperatures and pressures, facilitating in-situ processing and optimization.[89]

Through mechanochemical pulverization, the process disrupts chemical bonds through the kinetic energy of impacted balls, yielding small particles and generating new surfaces and properties. This mechanical approach offers several advantages, including simplicity, cost-effectiveness, and scalability, rendering this "top-down" route highly appealing. With proper control of optimization parameters, it becomes feasible to synthesize a diverse range of nanocomposite materials, spanning polymeric, ceramic, metallic, and other categories, with tailored size and shape. Researchers have utilized ball milling techniques to fabricate iron oxide nanoparticles with uniform and small sizes.[90,91] However, a notable disadvantage of this method is the contamination of the product and the wider size distribution of particles compared to those synthesized by chemical methods.[92] Besides, the milling process might induce lattice defects, resulting in

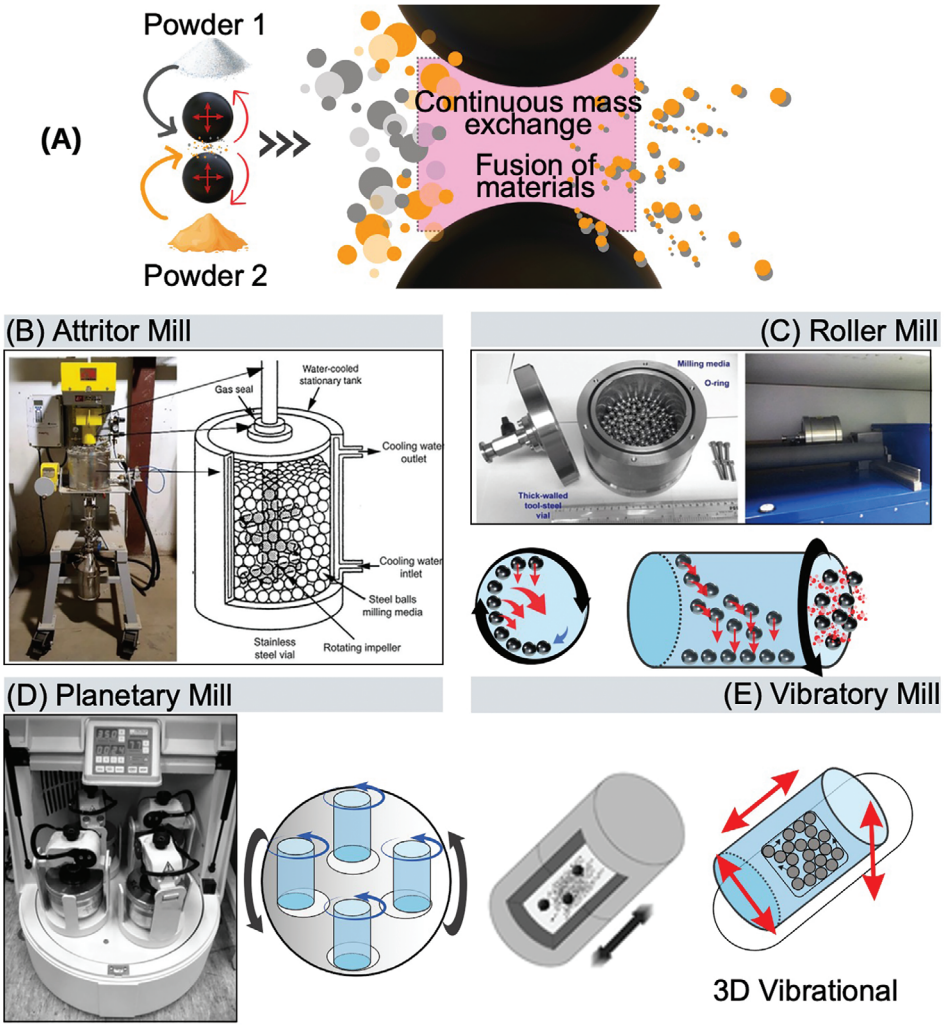


**Figure 6.** A) Schematic of ball milling. Examples of ball milling techniques commonly used for the physical synthesis of nanoparticles or nanocomposite materials are B) attrition, C) low-energy tumbling mills, D) planetary, and E) vibratory. A) is an original figure prepared by the authors. B–D) Reproduced with permission,[96] under a Creative Commons license CC BY 4.0. E) Reproduced with permission,[97] under a Creative Commons license CC BY 3.0.

deviations in the magnetic properties when compared to regular particles of identical size.[93–95]

*Laser Ablation*: Laser ablation (or evaporation) consists, in simple terms, of irradiating a solid material with a laser beam to synthesize nanomaterials from solid bulk precursors. This method is advantageous as it vaporizes materials challenging to evaporate, yields high-purity nanomaterials, accommodates various target materials alone or combined, and enables the production of nanoparticles with diverse compositions.[98] The types of laser that are commonly used for laser ablation applications include the Nd:YAG (neodymium-doped yttrium aluminum garnet), titanium-doped sapphire, and copper vapor lasers.[82] It is considered an environmentally sustainable bottom-up method for producing MNP powders due to its minimal waste generation and precise control over nanoparticle size, all while minimizing the utilization of hazardous chemicals.[84,99] In addition to MNPs, laser ablation can be used to synthesize metal nanoparticles (e.g., Ag, Au, Cu), carbon nanomaterials, silicon nanoparticles, and compound nanoparticles.[100–102]

This technique begins with coarse metal oxide powders comprising particles of a few micrometers in size, subjected to laser evaporation while immersed in a liquid medium as demonstrated in. **Figure 7** Here, the laser's intense energy swiftly vaporizes the source material into the gas phase, followed by its rapid condensation and nucleation due to the sharp temperature gradient surrounding the evaporation zone, ultimately culminating in the formation of nanoparticles through supersaturated vapor nucleation.[99,103,104] The resulting mean particle sizes, typically ranging from 2 to 50 nm, can be finely adjusted by controlling parameters such as laser source, wavelength, fluence, pulse width, frequency, and light absorption efficiency of the target material.[85]

For laser ablation conducted in a liquid solution, distilled or deionized water stands out as the predominant medium for synthesizing metal nanoparticles.[105] Organic solvents such as ethanol, isopropanol, acetonitrile, and ethylene glycol have garnered attention for laser ablation processes, with studies indicating that their higher dipole moment contributes

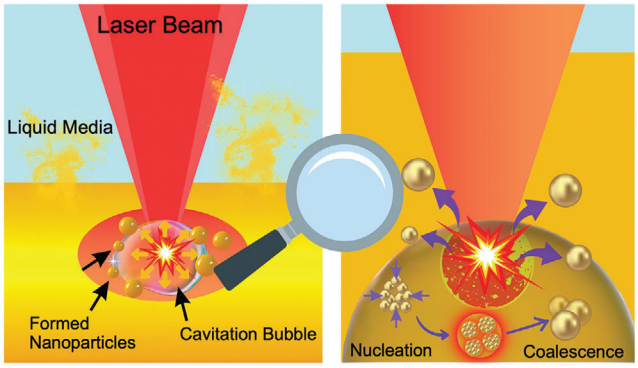


**Figure 7.** Schematics of laser ablation in liquid. Nanoparticles are formed from the substrate layer (target) inside the cavitation bubbles through nucleation and coalescence mechanisms. Original figure prepared by the authors.

to increased ablation efficiency and the formation of smaller particles.[106]

Laser ablation also enables the synthesis of finely dispersed colloid nanomaterials in liquids through continuous synthesis techniques, ensuring occupational safety when implemented within a sealed environment. With the decreasing prices of lasers due to rapid technological advancements, laser ablation has become increasingly affordable and accessible for MNP synthesis.[104] Additionally, its advanced capabilities in controlling nanoparticle morphologies contribute to its efficacy in producing MNPs from transition metals and metal alloys. However, for industrial scalability, efforts must be directed toward increasing productivity, which currently stands at a few grams per hour while demanding considerable energy consumption.[107] Recent advancements in laser ablation in liquid solutions for gold nanoparticle (AuNP) synthesis using microchip laser systems have shown promise in low power consumption and high ablation efficiency through low repetition and short pulse duration.[108] Nonetheless, further research is needed to enhance yield in this process.

*Gas-Phase (Condensation) Deposition*: The gas-phase deposition method encompasses both physical vapor deposition (PVD) and chemical vapor deposition (CVD). This technique has been widely used to synthesize metal, metal oxide, metal nitride, metal hydride, metal chalcogenide, metal sulfide, and carbon-made nanomaterials.[109–111] When employing metals like iron as raw materials, each method yields distinct outcomes. PVD typically generates fine iron oxide nanoparticles, whereas CVD is adept at producing high-quality iron oxide thin films or nanotubes.[112] Gas-phase synthesis methods offer a diverse range of strategies for the production of MNPs, with each approach tailored to specific products and characterized by distinct mechanisms and advantages. These methods are often categorized based on whether particle formation occurs via nucleation and condensation reactions of precursor gases or from reactions of dissolved substances in the form of droplets.[113,114]

Typically, gas-phase synthesis involves vaporizing the precursor in an inert gas flow to achieve supersaturation, followed by condensation into nanoparticles, with vapor generation mechanisms ranging from exclusively thermal sources to high-voltage sparks.[115] **Figure 8** depicts general schematics of the mechanism through which gas-phase synthesis of nanoparticles becomes possible.

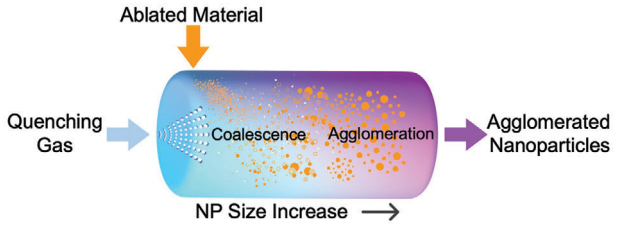


**Figure 8.** Schematics illustrating the generation of single and agglomerated nanoparticles through the gas-phase synthesis of ablated material at atmospheric pressure. Original figure prepared by the authors.

More specifically, supersaturation is commonly achieved by introducing an inert gas at a higher pressure than the material vapor pressure and triggers homogenous nucleation to produce seed particles essential for further growth. Nucleation, a fundamental step in gas-phase synthesis akin to that in liquid-phase synthesis, initiates once the supersaturation of the condensable precursor species in the reaction zone reaches a critical threshold, yielding high-purity and nonporous primary particles in the nanometer regime.[113] Finally, gas aggregation enables the formation of clusters, which, upon reaching sizes exceeding several tens of constituents, are referred to as nanoparticles. This process was facilitated by magnetron sputter discharge technique development, particularly prominent since the 1990s.[114] The flexibility and precision offered by gas-phase synthesis methods allow for the production of multi-element MNPs without the need for ligands or surfactants, which may alter their properties, although historically limited by relatively low yields.[115]

Compared to liquid-based syntheses, gas-phase deposition results in purer particles, as water introduces fewer unwanted microbes and impurities.[81,112,116] Despite their historical limitations in yield, gas-phase synthesis methods are favored for their ability to produce high-purity nanomaterials with high melting points in short reaction times.[98] An advantage of gas-phase deposition is its ability to synthesize particles in bulk with ease. A drawback is the challenge of maintaining nanoscale particle size consistency throughout the synthesis process.[112] However, they are constrained by their batch or unit time production capacity, making them less suitable for large-scale industrial applications that demand high throughput.[113]

Signorini et al. reported ion gas condensation (IGC) for synthesizing $Fe/Fe_xO_y$ core–shell nanoparticles.[117] The researchers evaporated highly pure iron in a high-pressure chamber, gradually introducing oxygen post-synthesis to form an iron oxide shell. By adjusting the evaporator's heating current, they controlled the evaporation rate, influencing nanoparticle size. Core–shell nanoparticles with core sizes ranging from 7 to 21 nm and oxide shells of 3 nm thickness were produced. The shell comprised magnetite ($Fe_3O_4$) and maghemite ($\gamma$-$Fe_2O_3$) phases, with maghemite dominating as the core size decreased.

### 2.1.3. Biological Methods

Traditional chemical and physical approaches, while effective, often come with inherent drawbacks, prompting the exploration

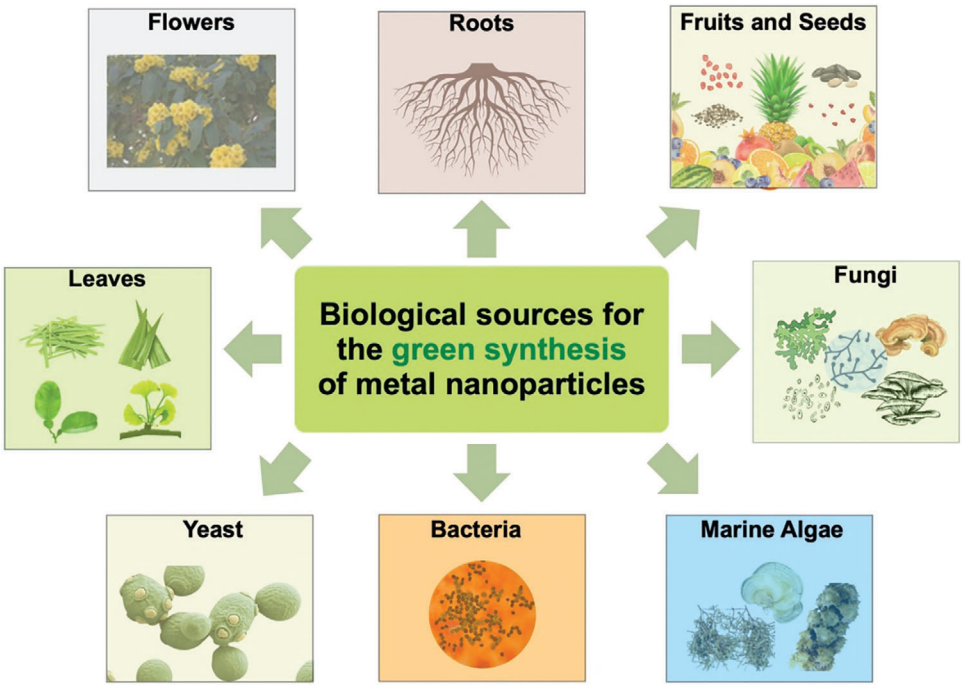


**Figure 9.** Summary of biomass used in the green synthesis of metal nanoparticles. Original figure prepared by the authors.

of alternative routes. Biological synthesis methods offer an increasingly popular, eco-friendly avenue for producing metal nanoparticles as an alternative to traditional chemical and physical approaches.[38,118] These methods, often referred to as green synthesis, circumvent the drawbacks associated with conventional methods, such as high production costs, toxicity concerns, and the generation of hazardous byproducts.[82] These methods can be categorized into microorganism-based and plant-based synthesis,[119] and are briefly exposed throughout the next lines. **Figure 9** summarizes the main sources of biomass used in the green synthesis of metal nanoparticles.

*Microorganism-Based Synthesis*: Within microorganism-based synthesis, various organisms such as bacteria, algae, and fungi have garnered significant attention due to their metabolic capabilities and widespread availability.[120,121] By utilizing enzymes, microorganisms can reduce metal salts to metal nanoparticles, a process that can occur either extracellularly or intracellularly.[122,123] Extracellular synthesis is favored for its simplicity and eliminates the need for downstream processing to recover the nanoparticles from cells.[123] For example, bacteria like *Rhodopseudomonas capsulata* have been shown to mediate the extracellular synthesis of AuNPs through enzyme secretion.[124] In addition to AuNPs, other metal-based nanoparticles, such as Ag, Au-Ag (bimetallic), $Fe_3O_4$, ZnO, $TiO_2$ CdS, ZnS, have been synthesized using bacteria.[121,125,126] Fungi exhibit greater resourcefulness compared to bacteria in nanoparticle biosynthesis, attributed to the abundance of bioactive metabolites, increased accumulation, and enhanced production capabilities.[127] Using fungi, various metal-based nanoparticles have been synthesized, including Ag, Au, Ag-Au (bimetallic), Cu, Pt, ZnO, $Fe_3O_4$, MgO, $TiO_2$, $ZrO_2$, and CdS.[121,125,126] On one hand, the intracellular synthesis processes involving fungi and metal salts undergo conversion into less toxic forms within the mycelia, making them readily usable by the fungi.[128] On the other hand, extracellular biosynthesis methods involve the utilization of fungal extracts. Further, studies have demonstrated the potential of microorganisms in synthesizing metal nanoparticles with specific properties.

Singh et al. investigated the synthesis of silver nanoparticles (AgNPs) using *Acinetobacter calcoaceticus*, emphasizing their enhanced antibacterial activity, particularly against Gram-negative bacteria.[123] Niknejad et al. synthesized AgNPs using *Saccharomyces cerevisiae*, showcasing their promising antifungal properties.[129] Prema et al. employed *Klebsiella pneumoniae* for the microbial-mediated synthesis of AuNPs, highlighting their antimicrobial efficacy.[130] Fatemi et al. demonstrated the synthesis of magnetic iron oxide nanoparticles (IONPs) using bacteria supernatant from *Bacillus cereus*, revealing their potential for drug delivery applications.[131] Characterization techniques confirmed the stability and cytotoxicity of the synthesized nanoparticles, suggesting their suitability for biomedical applications. These studies collectively underscore the significant strides made in utilizing biological synthesis methods for producing metal nanoparticles with low toxicity with diverse applications in nanomedicine.

*Plant-Based Synthesis*: Plant-mediated synthesis has emerged as a highly efficient and versatile method for the rapid production of nanoparticles, leveraging a plethora of plant substrates ranging from callus and leaves to fruits and seed extracts.[132,133] For example, green synthesis methods have yielded $Fe_3O_4$ nanoparticles with saturation magnetizations spanning from 13 to 70 emu $g^{-1}$ and average particle sizes measured in the tens of nanometers, rendering them amenable for diverse biological applications such as drug delivery and cancer cell targeting.[133] In

addition to $Fe_3O_4$ nanoparticles, other metal-based nanoparticles synthesized from plants include Au, Ag, Cu, Pd, Pt, Au/Ag, Cu/Ag, CuO, ZnO, and $TiO_2$.[134–136] Whether utilizing live or dead/inactive plant forms, the synthesis process typically involves mixing plant biomass or extract with a metal salt solution under controlled conditions.[137]

The reduction of metal ions to nanoparticles in plant-mediated synthesis is facilitated by a spectrum of bioactive constituents present in the plant extracts, including polyphenols, amino acids, and reducing sugars, showcasing the multifaceted roles of plant metabolites in nanoparticle formation.[82,138,139] Additionally, various secondary metabolites found abundantly in plants, such as terpenoids, alkaloids, phenols, and alcohols, actively participate in the reduction process, further enhancing the efficacy and yield of metal-based nanoparticles. The synthesis process and the properties of the resulting nanoparticles are significantly influenced by several factors, including the type and concentration of the plant extract, pH, metal salt concentration, contact time, and temperature, emphasizing the importance of optimizing these parameters for desired nanoparticle characteristics.[118,137,140] Across a wide spectrum of plant species, including lemon grass, mustard, coriander, grape, neem, oats, and many others, plant-mediated synthesis has demonstrated remarkable versatility and potential, offering a sustainable and eco-friendly route for the production of nanoparticles tailored for various biomedical and environmental applications.[141]

Furthermore, green-synthesized nanoparticles have been explored for a variety of biomedical applications, including their roles as anticancer, antioxidant, anti-inflammatory, and antiviral agents, with their therapeutic efficacy attributed to the presence of phytochemicals and other bioactive materials inherent in the plant substrates.[142] Moacă et al. demonstrated the synthesis of IONPs using aqueous extracts from wormwood, highlighting their potential for hyperthermia treatments.[140] Tatarchuk et al. presented the synthesis and characterization of spinel magnesium ferrite nanoparticles with promising hyperthermic properties, suggesting their utility in medical applications, particularly in cancer treatment.[143] Sharmila et al. introduced a green synthesis method for zinc oxide nanoparticles using leaf extract, exhibiting excellent antibacterial and anticancer activities, emphasizing their potential in biomedical and nano-drug delivery systems.[144] Umadevi et al. highlighted the green synthesis of AgNPs using tomato fruit extract, shedding light on the role of natural extracts in producing nanoparticles with well-defined structural and chemical properties for various applications.[145] These studies collectively underscore the efficacy, versatility, and burgeoning potential of plant-mediated synthesis in advancing nanoparticle technology toward greener and more sustainable practices.

### 2.2. Gold Nanoparticles (AuNPs)

Gold nanoparticles (AuNPs) can be developed into a variety of anisotropic morphologies, as shown in **Figure 10**A–F, with gold nanospheres being the most prevalent shape. Despite their stable, shiny, and yellow appearance in bulk form, AuNPs display distinct properties when reduced to the nanoscale. AuNPs find extensive applications in cancer theranostics due to the versatility and controllability of their synthesis methods. These nanoparticles offer a wide range of applications including targeted delivery, imaging capabilities, and photothermal therapy, rendering them valuable tools for cancer diagnosis, imaging, and treatment. By maintaining a spherical shape, Au nanospheres exhibit high stability and possess a relatively small specific surface area.

#### *2.2.1. Chemical Reduction Method*

The preparation of AuNPs via the chemical reduction method involves two main steps:

(a) Reduction by Agents. This step entails using reducing agents to convert gold ions into AuNPs. Common reducing agents include borohydrides, amino boranes, formaldehyde, hydrazine, hydroxylamine, polyols, citric and oxalic acids, sugars, hydrogen peroxide, carbon monoxide, sulfites, hydrogen, acetylene, electron-rich transition-metal sandwich complexes.

(b) Stabilization via Agents. To prevent the nanoparticles from aggregating, stabilizing agents are added. These agents help to maintain the dispersion and stability of the nanoparticles. Common stabilizing agents include trisodium citrate dihydrate, sulfur ligands (especially thiolates), phosphorus ligands, dendrimers, polymers, surfactants (particularly cetyltrimethylammonium bromide, CTAB), and very recently, cell membrane coatings. The use of stabilizing agents is crucial to avoid the aggregation of the gold nanoparticles, ensuring their stability and functionality.[147]

#### *2.2.2. Turkevich–Frens Method*

Maintaining a spherical shape, Au nanospheres exhibit high stability and possess a relatively small specific surface area. Synthesis methods such as the Turkevich–Frens method[148] enable precise control over Au nanospheres productions by modulating the ratio of citrate-to-gold chloride. The Turkevich method, introduced in 1951, is a well-known technique for synthesizing AuNPs by reducing $HAuCl_4$ with citrate in water. The process involves boiling an $HAuCl_4$ solution and rapidly adding trisodium citrate dihydrate under vigorous stirring. The solution color changes from light yellow to wine red, producing AuNPs ≈20 nm in diameter. Citrate ions serve dual roles as both reducing and stabilizing agents. In 1973, Frens modified this method to control the size of AuNPs (15–150 nm) by adjusting the trisodium citrate/gold ratio.[149] Subsequent research demonstrated that higher citrate concentrations stabilize smaller AuNPs, while lower concentrations lead to particle aggregation.[150] Recent studies highlighted the influence of sodium citrate on solution pH and nanoparticle size control.[151–154] An inverse sequence method, adding $HAuCl_4$ into boiling sodium citrate, results in smaller, uniformly sized AuNPs.[155] Factors affecting AuNP properties synthesized using such a route include temperature, pH, citrate concentration, and gold chloride concentration, as explored in various studies.[156–159]

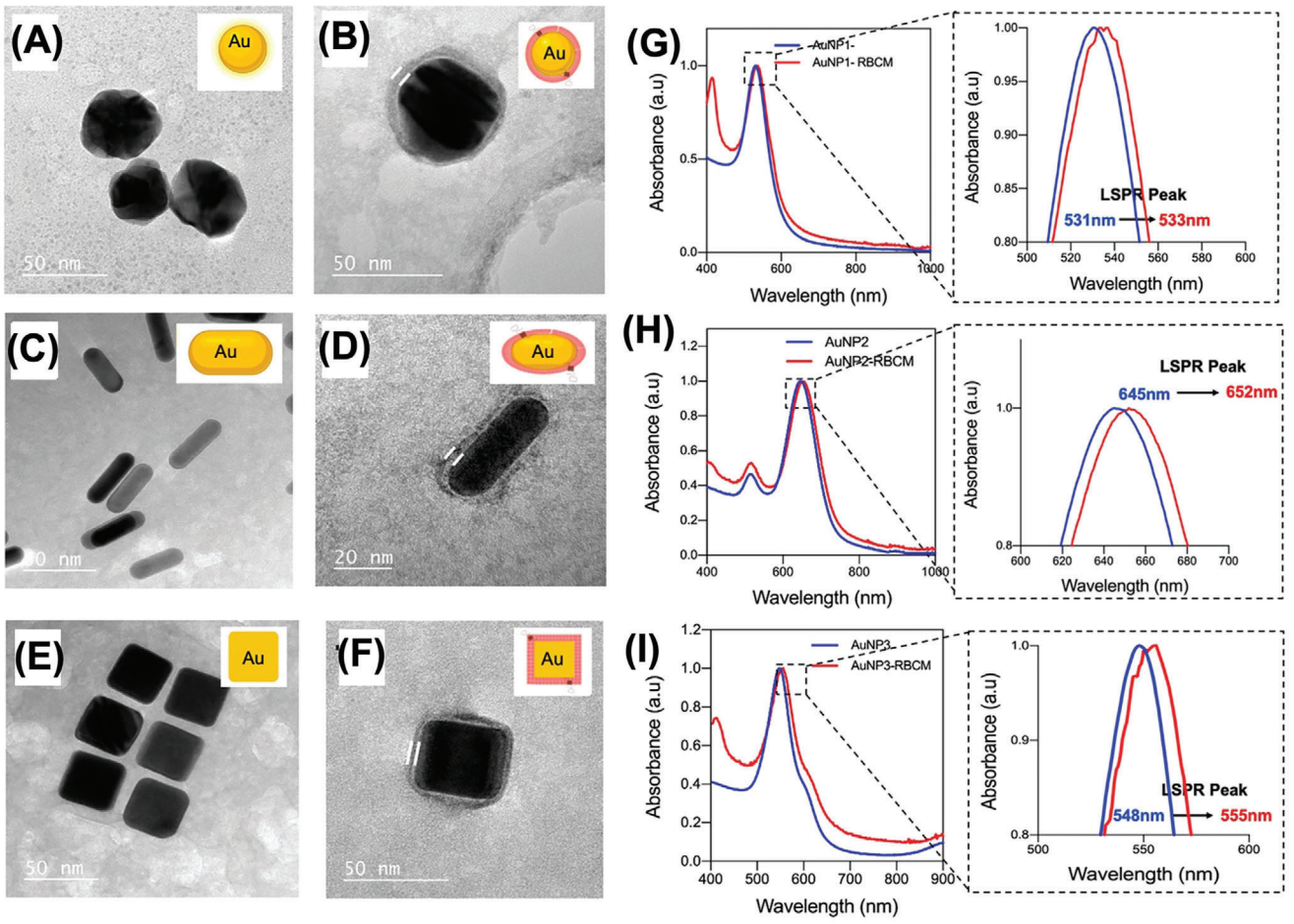


(J)

| Samples | Hydrodynamic Diameter (nm) | | Zeta Potential (mV) | |
|---|---|---|---|---|
| | -RBCM | +RBCM | -RBCM | +RBCM |
| AuNP1 | 44 ± 5 | 64 ± 4 | -37 ± 6 | -28 ± 3 |
| AuNP2 | 54 ± 4 | 66 ± 4 | -38 ± 6 | -27 ± 4 |
| AuNP3 | 53 ± 5 | 68 ± 4 | -40 ± 6 | -30± 2 |

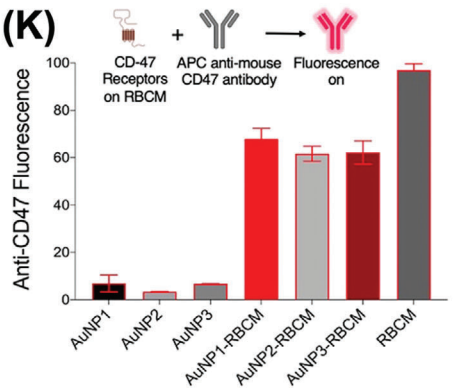


**Figure 10.** Physicochemical characterization of anisotropic red blood cell membrane (RBCM)-coated AuNPs. Negative-stained transmission electron micrographs of A) AuNP1-Citrate, B) AuNP1-RBCM, C) AuNP2-Cit, D) AuNP2-RBCM, E) AuNP3-Cit, and F) AuNP3-RBCM, with the membrane coating in (B, D, F) highlighted with white lines. G–I) UV–vis absorbance spectra of AuNP's and AuNP-RBCM's, with the inset boxes zoomed. The inset shows the intrinsic plasmonic absorbance peak shift for different anisotropic AuNPs upon RBCM coating. J) Hydrodynamic diameter and $\zeta$ potential measurements for AuNPs before and after RBCM coating. K) Anisotropic AuNPs uncoated and coated with RBCM were stained with a fluorescent anti-CD47 antibody. Data are shown as mean ± standard deviation, $n = 3$. Reproduced with permission.[146] Copyright 2022, American Chemical Society.

### 2.2.3. The Brust–Schiffrin Method and Seeding Growth Method

Alternatively, for the synthesis of molecules smaller than 5 nm, various protocols including the Brust-Schiffrin approach,[160] or the seeded growth method[161,162] can be employed. These tiny Au nanospheres are occasionally referred to as gold nanoclusters, and some of them even exhibit near-infrared (NIR) fluorescence properties.[163,164] Au nanospheres further exhibit a phenomenon known as localized surface plasmon resonance (LSPR), that leads to strong interactions with light at specific wavelengths. Accord-

ing to Mie theory, the extinction spectra of Au nanospheres can be calculated, showing that the LSPR peak typically occurs around 520 nm but shifts slightly towards the red and broadens with increasing nanoparticle size (see Figure 10G–J).[146]

Au nanorods (AuNRs) exhibit distinctive optical properties due to their anisotropic morphology, exhibiting both longitudinal and transverse LSPR peaks.[165] The aspect ratio, which dictates the proportions of these modes, governs the positioning of the longitudinal LSPR band.[166,167] Diverse synthesis techniques, such as seed-mediated growth,[161] facilitate the production of AuNRs with varying aspect ratios. In contrast to Au nanospheres, AuNRs offer superior extinction coefficients, narrower line widths, and enhanced sensitivity to alterations in the local dielectric constant.[168] These properties make AuNRs valuable for applications in spectroscopic detection of tumor cells and photothermal therapy in cancer treatment.[169]

Another type of AuNPs, gold nanoshells, is typically synthesized by encapsulating a silica nanoparticle core with a gold shell.[170,171] Halas et al. pioneered the production of gold nanoshells featuring a tunable LSPR peak within the NIR light spectrum by adjusting the ratio of shell thickness to core diameter or modulating the surface topology.[172,173] Due to the unique plasmonic property of gold nanoshells, they exhibit stronger NIR absorbers and scattering capabilities compared with Au nanospheres and gold nanoshells.

Gold nanocages (AuNCs) are one of the new classes of Au nanostructures developed in the early 2000s.[174,175] Synthesized using silver nanocubes as templates and reductive seeds, AuNCs' shell thickness and porosity are pivotal for controlling the positioning of the longitudinal LSPR band (400–1200 nm),[176] modifiable by adjusting the amount of gold sources. Augmenting the gold source leads to a redshift in the LSPR band. AuNCs' size, ranging from 20 to 500 nm, can be adjusted, impacting their cellular uptake and biodistribution.[177]

In addition to the commonly known gold nanostructures, several others have gained attention recently. Gold nanostars (AuNSr) feature multiple sharp branches at the nanoscale,[178] allowing size control from ≈45 nm to 116 nm and tuning the position of the longitudinal LSPR band within the NIR range from ≈725 to over 850 nm.[179] Gold nanoplates, prepared with $HAuCl_4$, sodium citrate, and poly(vinyl pyrrolidone) (PVP), are single crystals with planar widths of 80–500 nm and thicknesses of 10–40 nm, exhibiting a strong LSPR in the NIR spectrum of 700–2000 nm.[180,181] Gold nanoprisms (AuNPrs), synthesized via seeded growth[161] or photochemical methods,[162] boast particularly strong LSPR due to their sharp corners and edges. The edge length of AuNPrs can be adjusted in the range of 100–170 nm by altering the molar ratio of $HAuCl_4$ to the reducing agent.[182] Gold bellflowers (AuBFs), produced at a novel liquid-liquid-gas tri-phase interface, feature multiple-branched petals with ultra-strong NIR absorbance and ultrahigh photothermal conversion efficiency ($\eta$ = 74%).[183] Gold nano crosses, unlike gold nanorods growing along specific crystallographic directions, experience anisotropic growth along both 110 and 001, exhibiting pronounced NIR absorption extending to the mid-IR region.[184] Using a poly(ethylene glycol)-block-poly($\epsilon$ – caprolactone) polymer (PEG-b-PCL) terminated with a disulfide bond, Au nanospheres can be assembled into gold nanovesicles (AuNVs). This is a direct result of plasmonic coupling between adjacent gold nanospheres and enhancing LSPR absorption in the NIR region.[185]

The primary goal of these methods is to develop a variety of gold nanostructures with strong LSPR absorption or scattering within the visible-NIR range. This attribute is critical for achieving high photothermal conversion efficiency and outstanding bio-imaging capabilities. Notably, gold nanostructures with NIR absorption are preferred due to their capacity to minimize tissue penetration and enable deeper tissue visualization, particularly important for cancer theranostics, as skin and tissue exhibit lower absorption of NIR light compared to visible light. Strong LSPR absorption is observed in AuNRs with high aspect ratios, Au nanospheres, and specific AuNCs, as well as nanostructures with branching, sharp ends, or plasmonic coupling effects. These properties render them highly promising candidates for biomedical applications. Understanding the relationships between gold nanostructures and their associated characteristics can guide structural manipulation to achieve desired qualities tailored for cancer theranostics.

### 2.2.4. Electrochemical Method

The electrochemical production of nanoparticles was pioneered by Reetz et al. in 1994.[186] Their research demonstrated that the size of transition metal nanoparticles could be selectively controlled electrochemically using tetraalkylammonium salts as stabilizers in a nonaqueous medium. One application of this technique is the preparation of AuNPs on the surface of multiwalled carbon nanotubes with glassy carbon electrodes.[187] This is achieved using a simple two-electrode cell, where AuNPs are produced through the oxidation of the anode and reduction at the cathode.[188] The electrochemical synthesis of nanoparticles is considered superior to other methods due to its advantages such as requiring modest equipment, low cost, lower processing temperatures, high quality of nanoparticles produced, and ease of controlling the yield.[189–193]

### 2.2.5. Biological Method

Chemical methods are common for synthesizing metallic nanoparticles, but they often involve expensive and toxic reagents, limiting their applications, particularly in biomedicine due to potentially harmful effects. Therefore, there is a growing demand for eco-friendly and cost-effective methods that avoid toxic chemicals. Biological synthesis of nanoparticles has emerged as a green alternative, utilizing microorganisms, enzymes, and plant extracts. Plant-based synthesis is especially favored for its availability, low cost, eco-friendliness, and non-toxic nature. Notable plants used for synthesizing AuNPs include *Azadirachta Indica*[194] *Medicago Sativa*,[195] *Aloe Vera*,[196] *Cinnamomum Camphora*,[197] *Pelargonium Graveolens*,[198] *Coriandrum Sativum*,[199] and *Terminalia Catappa*.[200] Additional research has reported AuNP synthesis using extracts from various plants, such as *Memecylon umbellatum*,[201] *Macrotyloma uniflorum*,[202] Citrus species,[203] *Piper pedicellatum*,[204] *Terminalia chebula*,[205] *Nyctanthes arbor-tristis*,[206] *Murraya koenigii*,[207] *Mangifera indica*,[208] Banana peel,[209] *Cinnamomum*

*zeylanicum*,[210] and *Cochlospermum Gossypium*.[211] For instance, Zingiber officinale extract has been used to synthesize AuNPs sized 5 nm – 15 nm, functioning as both reducing and stabilizing agents.[212] Similarly, *Allium cepa* (onion) extract, due to its vitamin C content, has been employed for the green synthesis of AuNPs.[213]

### 2.3. Hybrid Nanoparticles

#### *2.3.1. Different Types of Hybrid Nanoparticles*

Hybrid nanomaterials are chemical conjugates of organic and/or inorganic materials, comprising mixtures of two or more inorganic constituents, two or more organic constituents, or a combination of both.[214] These materials exhibit synergistic properties rather than merely being simple mixtures, with optimized electronic, optical, magnetic, thermal, electrochemical, or biochemical characteristics. Their adaptability allows for the design of materials with tunable properties, making them suitable for a wide range of applications, including optics, electronics, sensors, energy conversion, catalysis, and more.

Bifunctional luminescent/magnetic micro- and nanoparticles have garnered significant interest due to their extended functionality and broad applications.[215] For example, these nanoparticles enable target isolation using an external magnetic field, followed by separation and quantification based on luminescent properties, particularly relevant in cancer research and diagnosis, cell isolation, therapy, and pathogen analysis.[32,216–218] In the context of modern medicine and nanotechnology, theranostics plays a pivotal role, integrating diagnostic and therapeutic tools to advance medical interventions.[219]

As illustrated in **Figure 11**, hybrid nanoparticles can be composed of a combination of different types of nanostructures, such as quantum dots (QDs), superparamagnetic iron oxide nanoparticles (SPIONs), and gold- and silver-based nanoparticles, among others, which offer combined diagnostic and therapeutic functionalities, exemplifying the potential of nanotechnology in personalized and effective treatment modalities.[132,220–223] QDs are composed of semiconductor nanocrystals and emit a distinct wavelength of light upon energy excitation. These nanostructures enable precise imaging and therapy with their unique optical properties and large surface areas for biomolecule conjugation.[224] SPIONs provide controllable sizes for direct interactions with biological systems and exhibit superparamagnetic characteristics for targeted drug delivery.[225] AuNPs, characterized by varied shapes and excellent biocompatibility, offer superior photoimaging capabilities and versatile nanoplatforms for imaging, diagnosis, and therapy.[226,227]

Other types of bi-functional nanostructures involve a combination of semiconducting nanostructures (Fe, Cd, Mn, Ni, etc.), QDs, noble metals, carbon, and silica components.[223,240,241] For example, Zhan and Zhang introduced a novel synthesis method for CdSe@$Fe_2O_3$ core/shell nanoparticles.[240] These nanoparticles, combining CdSe QDs and $Fe_2O_3$ magnetic nanocrystals, offered fluorescent and superparamagnetic properties, while exhibiting distinct optical behaviors influenced by their composite structure. The authors demonstrated that CdSe nanoparticles displayed characteristic exciton absorption and emission peaks at 600 nm and 618 nm, respectively. The measured quantum yield (QY) of CdSe QDs stood at 36%. Quantum yield represents the efficiency with which a fluorophore converts excitation light into fluorescence, and it remains consistent regardless of instrument settings.[242] Upon encapsulation with $Fe_2O_3$, the absorption peak of CdSe@$Fe_2O_3$ nanoparticles shifted to 611 nm, while the emission peak remained at 619 nm. Remarkably, the QY of CdSe@$Fe_2O_3$ nanoparticles experienced a significant enhancement of up to 64% compared to bare CdSe nanoparticles.

Wang et al. designed novel theranostic hybrid nanostructures consisting of $Fe_3O_4$ nanocrystal cores enveloped by carbon shells.[241] These hybrid nanoparticles were synthesized via a one-pot solvothermal method employing ferrocene as the sole precursor. These nanostructures, with a uniform size of ≈16 nm, exhibited remarkable stability in solution attributed to the presence of hydrophilic carboxyl groups on the carbon shell surface. Evaluation using human SF763 glioblastoma cells demonstrated the fluorescence imaging functionality in vitro. These hybrid nanoparticles exhibited dual-modal imaging capacity both in vitro and in vivo, with fluorescent imaging excited across a spectrum from 405 to 820 nm, complemented by T2-weighted magnetic resonance imaging (MRI). This hybrid nanostructure showcased versatile properties, including excitation wavelength-tunable, upconverted, and NIR fluorescence facilitated by the carbon shell, along with superparamagnetic behavior arising from the $Fe_3O_4$ core. Leveraging both fluorescent carbon shells and superparamagnetic cores, these particles offered promising dual-modal imaging capabilities for fluorescence bioimaging and MRI.

More recently, Nazeer et al. showcased the potential of a carbon dot (Cdt)-iron oxide hybrid nanosystem as a dual functional imaging agent for liver fibrosis.[223] Initially, two types of SPIONs were developed: one coated with alginate (ASPIONs) and the other with pullulan (PSPIONs). Subsequently, these materials were conjugated with fluorescent Cdts, resulting in ASPION-Cdts and PSPION-Cdts. ASPION-Cdts were synthesized through the covalent conjugation of the carboxyl groups on ASPIONs with the amino groups of diamino PEG, followed by coupling with Cdts. This process enhanced stability while preserving optical and magnetic properties. On the other hand, PSPION-Cdts were formed via electrostatic interaction between PSPIONs and Cdts. The superparamagnetic nature of both ASPIONs and PSPIONs remained intact upon conjugation with Cdts. Notably, ASPION-Cdts exhibited a reduction in saturation magnetization from 62.7 to 42 emu $g^{-1}$, while PSPION-Cdts showed a significant decrease to 3.17 emu $g^{-1}$. Both hybrid systems displayed decreased T2 relaxation rates and increased T1 relaxation rates compared to SPIONs, enabling MRI while retaining fluorescence imaging capability. Furthermore, cytocompatibility of the hybrid nanosystems was maintained, with only a slight decrease in cell viability compared to SPIONs. Both ASPION-Cdts and PSPION-Cdts demonstrated excellent cellular labeling efficiency, with PSPION-Cdts outperforming ASPION-Cdts for imaging applications. The use of red-emitting Cdts in fluorescence imaging presents a promising avenue for future exploration, potentially minimizing tissue autofluorescence and enhancing imaging efficiency. Overall, hybrid nanoparticles represent promising tools for advancing theranostic strategies in human medicine, underscoring the potential of nanotechnology in enhancing healthcare outcomes.

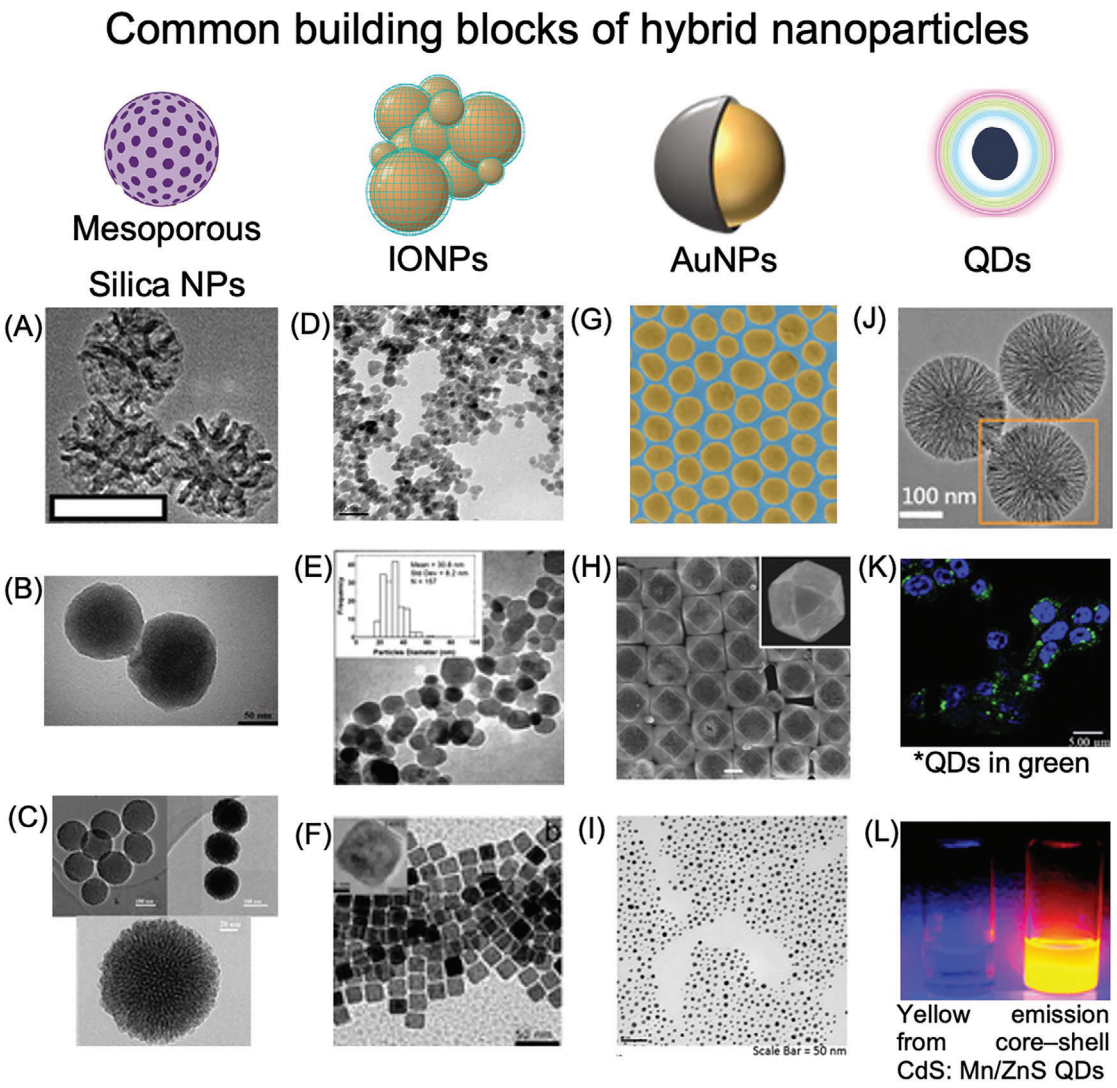


**Figure 11.** Common building blocks of hybrid nanoparticles. A) Reproduced with permission.[228] Copyright 2020, Acta Materialia Inc. B) Reproduced with permission,[229] under a Creative Commons license CC BY-NC 3.0. C) Reproduced with permission.[230] Copyright 2009, The Royal Society of Chemistry. D) Reproduced with permission,[231] under a Creative Commons license CC BY 4.0. E) Reproduced with permission.[232] Copyright 2014, American Chemical Society. F) Reproduced with permission.[233] Copyright 2009, The Royal Society of Chemistry. G) Reproduced with permission,[234] under a Creative Commons license CC BY-NC 3.0. (H) Reproduced with permission.[235] Copyright 2002, The American Association for the Advancement of Science. (I) Reproduced with permission.[236] Copyright 2018, American Chemical Society. J) Reproduced with permission.[237] Copyright 2018, American Chemical Society. K) Reproduced with permission.[238] Copyright 2022, Elsevier Inc. L) Reproduced with permission.[239] Copyright 2005, American Chemical Society.

### *2.3.2. Methods for Synthesis of Hybrid Nanoparticles*

Various methods of synthesis of hybrid nanoparticles can be split into "top-down" (thermal decomposition, laser ablation, plasma/microplasma-based and electrochemical etching) and "bottom-up" (solution-based reduction in the presence of silane precursors, zintl salt metathesis and aqueous reduction), commonly found as physical and chemical methods, respectively.[214] Physical methods offer simplicity but limited control over nanoparticle size, allowing for direct and robust hybridization between nanoparticles, whereas chemical methods, involving the reduction of metal precursors, enable precise control over nanoparticle size and composition, albeit with potential unwanted properties due to stabilizing ligands or polymer shells.[243] Chemical reduction (CR) methods involve the deposition of noble metal nanoparticles onto the surface of metal oxides. This process begins with the adsorption of noble metal ions onto the surface of metal oxides, followed by their reduction through chemical-reducing agents.[214] Alternatively, photoreduction (PR) methods rely on the emission of photoelectrons from metal oxides, particularly titanium,[243,244] and zinc,[245] upon light irradiation, which catalyzes the reduction process and facilitates the formation of nanoparticles on the surface of host larger nanoparticles.

Additionally, various other processing routes are utilized for fabricating hybrid nanoparticles through chemical methods, in-

cluding hydrothermal, thermal decomposition, sol-gel, coprecipitation, electrodeposition, sonochemical, and seeding growth methods. These methods enable the creation of diverse hybrid nanoparticles with tailored properties, facilitating applications across numerous fields. Examples of studies that used a combination of different synthesis methods to develop novel nanomaterials are briefly exposed throughout the following lines.

For example, Bakal et al. utilized a combination of hydrothermal and chemical co-precipitation methods to synthesize bifunctional magnetite-luminescent carbon nanostructures with dual magnetic and luminescent properties.[215] They found that under varying experimental conditions, a portion of $Fe_3O_4$ nanoparticles combined with luminescent carbon nanostructures to form a complex, demonstrating the complexation of carbon and magnetite during synthesis. The resulting colloid exhibited characteristic absorption peaks for magnetite and luminescent carbon nanostructures, alongside strong luminescence at a 450 nm wavelength. Additionally, the synthesized bifunctional nanoparticles displayed both negative and positive charges, while retaining luminescent properties akin to luminescent carbon nanostructures. Spectrometric titration confirmed the presence of iron, indicating an iron concentration of 0.2 mg $mL^{-1}$ of $Fe^{3+}$.

Jiang et al. developed $NiFe_2O_4$/ZnO hybrid nanoparticles exhibiting ferromagnetic properties through the hydrolysis of zinc acetate in the presence of $NiFe_2O_4$ in a water-in-oil microemulsion under ultrasonic irradiation.[245] Transmission electron microscopy (TEM) analysis confirmed the deposition of a ZnO nanolayer onto quasi-spherical $NiFe_2O_4$ particles. The magnetization behavior of the synthesized samples demonstrated ferromagnetic properties under an applied magnetic field, albeit with a saturation magnetization of 33.5 emu $g^{-1}$, lower than the bulk value, attributed to the nonmagnetic ZnO dead layer's contribution. Coating with ZnO influenced the surface anisotropy, shape anisotropy, and interparticle interactions, resulting in reduced coercivity. Viswanathan demonstrated the synthesis of fluorescent silica-coated magnetic hybrid nanoparticles through a combination of co-precipitation, polymerization, and sol-gel techniques with fluorescent dye incorporation, yielding nanoparticles ranging in diameter from ≈80 to 90 nm.[246] Characterization was conducted using various analytical methods including atomic force microscopy (AFM), Fourier transform infrared (FTIR) spectroscopy, spectrofluorometer, X-ray diffraction patterns (XRD), and energy-dispersive X-ray spectroscopy (EDS).

Kas et al. investigated the synthesis of QD-SPION hybrids (MDOTs) for medical and biotechnological applications.[247] QDs, known for their higher quantum yield and superior photostability, have replaced organic fluorophores in various applications, including optical detection of cancer cells, DNA hybridization, and immunoassays. SPIONs, on the other hand, find various applications in magnetic separation, cell sorting, immunoassays, and diagnostic imaging. The study proposed the development of MDOTs combining SPIONs and luminescent QDs through an extraction method involving a ligand-exchange mechanism to prepare small, stable, aqueous QD-SPIONs hybrid nanostructures. The synthesis process utilized by the authors is summarized in **Figure** 12A and detailed throughout the following lines: to prepare QD-SPIONs hybrid nanoparticles, their standard procedure involved mixing lactic acid-coated SPIONs in chloroform with aqueous QDs in a 100 mL round-bottomed flask equipped with a mechanical stirrer. The mixture underwent simultaneous sonication and stirring at 1000 rpm. Subsequently, the mixture was transferred to a separatory funnel to separate the aqueous phase containing the hybrid nanoparticles. This aqueous phase underwent a back-extraction process using chloroform. In this approach, surface carboxylate functionalized aqueous QDs replace the lactic acid coating of SPIONs during a water/chloroform extraction process. This facilitated the efficient transfer of SPIONs into water, now coated with QDs and, thus, forming the aimed MDOTs.

DLS and TEM characterization results (Figure 12B) elucidated the presence of MDOTs of ≈80 nm in diameter. A 15% to 33% decrease in luminescence intensity to the original QD emission was reported and it was argued that the incorporation of SPIONs was the cause of this reduction. As depicted by Figure 12C, all MDOT formulations exhibited robust luminescence properties and decent emission stability. The magnetic behavior of the MDOTs was observed (Figure 12D) and characterized by the hysteresis loop present in Figure 12E, suggesting an approximately paramagnetic trait. Their study demonstrated the effectiveness of both polymeric coatings and small molecules in stabilizing QDs and SPIONs simultaneously. The resulting QD-SPION hybrid nanoparticles offered dual functions such as detection and separation, optical and magnetic detection, as well as therapy. The small size and stable aqueous colloidal form make these hybrid nanoparticles advantageous for in vivo and in vitro studies. The versatility of this method suggests its potential application to other nanoparticles including gold or $TiO_2$.

## 3. Polymer Coatings for Nanoparticles

### 3.1. Synthetic Polymer Coatings

Nanoparticles and nanocomposites play a crucial role in various theranostic applications, necessitating precise control over their monodispersity, core size, saturation magnetization, and hydrodynamic diameter.[248–250] Achieving water-dispersible nanostructures is equally imperative, particularly in biological aqueous environments characterized by balanced ionic forces. Coating nanoparticles with synthetic polymers serves as a pivotal strategy to prevent agglomeration, enhance biocompatibility, and supplement surface functionality.[243] This coating is essential for maintaining colloidal stability, preventing gravitational settlement, and mitigating aggregation among particles. In recent years, various functionalizing agents have been explored to enhance the colloidal stability and surface properties of metal oxide nanoparticles.[251,252] These agents include but are not limited to poly(acrylic-co-maleic) polymers, poly(Trolox ester), and polyacrylic acid (PAA). By modifying the surface of nanoparticles, these coatings improve their stability and biocompatibility, rendering them suitable for various biomedical applications.

For instance, in an example of synthesizing gold-ferric oxide superparamagnetic nanoparticles for NIR-responsive photothermal ablation in breast cancer therapy,[253] The authors surface-coated nanoparticles with Poly(α-L-lysine) (PLL), which not only facilitated cellular uptake and biocompatibility but also ensured colloidal stability across diverse biological environments, including cell culture medium and physiological solutions. Characterization studies confirmed the successful fabrication and struc-

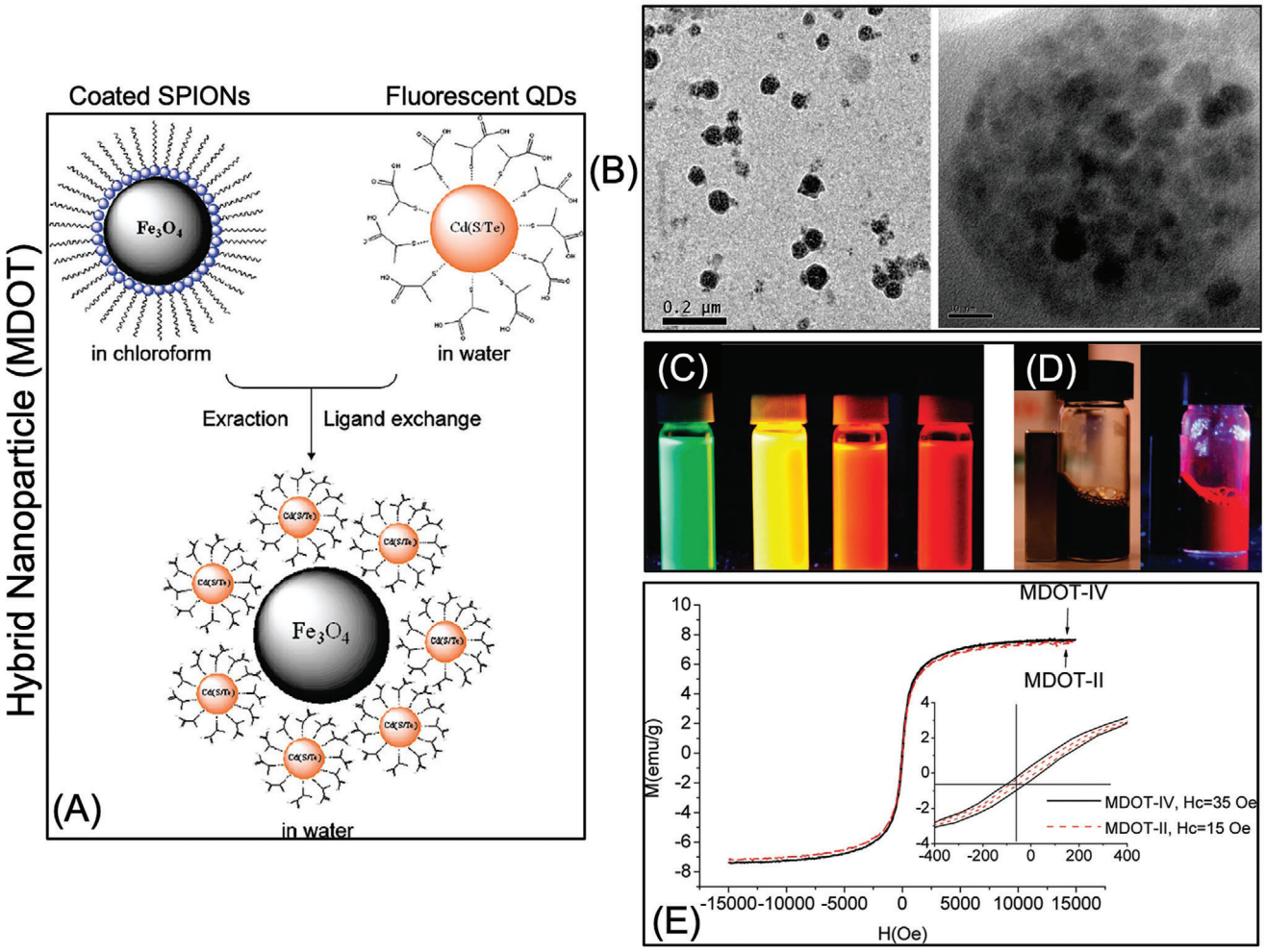


**Figure 12.** Summary of main results from the study of Kas et al. as an example of the successful synthesis of hybrid nanoparticles: A) approach used to synthesize hybrid nanoparticles through a ligand-exchange mechanism. B) TEM characterization images of the synthesized QD-SPION hybrid nanoparticles (MDOT). C) Synthesized MDOTs luminescing from green to red spectra under UV excitation. D) Red luminescing MDOTs interacting with an external magnetic field of 0.3T. E) Hysteresis loop of MDOTs with different QDs/SPIONs ratios synthesized through the approach used by the authors. Reproduced with permission.[247] Copyright 2010, American Chemical Society.

tural integrity of PLL–Au–$Fe_3O_4$ nanoparticles, highlighting their potential in diagnostic and therapeutic applications. In the following subsections, we list and discuss different synthetic polymeric coatings increasingly explored in theranostics. These coatings offer promising avenues for the development of multifunctional nanoparticles with enhanced stability, biocompatibility, and therapeutic efficacy. At the end of this section, we provided **Table 2** to summarize and compare the different polymer coatings for nanoparticles, including aspects such as synthesis, stability, biocompatibility, and biomedical applications.

### *3.1.1. Polyacrylic Acid (PAA)*

Polyacrylic acid (PAA) is a synthetic polymer composed of acrylic acid monomers with high molecular weight (see **Figure 13**A). Each monomer unit of PAA contains a carboxylic group (—COOH) attached to the vinyl group at one end. PAA is characterized by its biocompatibility, water solubility, non-toxicity, and recyclability, making it a versatile superabsorbent polymer.[254,255] The study by Nahar et al. elucidated a straightforward one-pot synthesis approach for fabricating PAA-functionalized IONPs.[248] Through a combination of free radical solution polymerization and coprecipitation of $Fe^{3+}$ and $Fe^{2+}$ salts, PAA-coated IONPs were synthesized, exhibiting enhanced colloidal stability and surface functionality. Characterization studies encompassing structural analysis, thermal stability, and magnetic behavior underscored the successful surface functionalization of IONPs with PAA. Moreover, an investigation into the adsorption of biocatalysts onto PAA-functionalized IONPs showcased their potential as magnetically recyclable carriers for various biomedical applications.

Building on the understanding of PAA coatings, Sanchez et al. explored the influence of PAA molecular weight on the magnetic properties of IONPs.[256] Through systematic variation of PAA molecular weights and thorough characterization, they de-

**Table 2.** Different Polymer Coatings for Nanoparticles.

| Polymer | Stability | Biocompability | Biomedical Applications | Synthesis |
|---|---|---|---|---|
| **PAA** | Sensitive to pH changes, exhibits good thermal stability under normal conditions | Good cytocompatibility and non-immunogenic | Drug delivery, tissue engineering and wound healing | Polymerization of acrylic acid |
| **PDA** | Resistant to many organic solvents and stable under a broad pH range, moderate thermal stability | Highly biocompatible, non-toxic to cells | Drug delivery, biosensing, antibacterial coatings and photothermal therapy | Oxidative polymerization of dopamine in an alkaine environment. |
| **PLL** | Stable under physiological conditions but can be susceptible under extreme pH conditions | Highly biocompatible and promote cell adhesion, non-toxic and naturally metabolized by the body | Cell culture, drug delivery and gene therapy | Ring-opening polymerization of NCAs of lysine |
| **PEG** | Stable under a wide range of pH levels and temperature | Hydrophilic prolonging circulation time in biological systems biodegradable minimal toxicity | MRI contrast enhancement, magnetic hyperthermia targeted drug delivery, wound healing | Anionic polymerization of ethylene oxide with hydroxyl initiators or ring-opening polymerization of epoxyethane. |
| **PLGA** | Stable in physiological conditions, allowing to maintain the structural integrity over time in biological environments | minimizing adverse reactions when interacting with biological systems, tailored biodegradation rates | drug delivery systems, tissue engineering scaffolds, and medical implants. | enzymatic fermentation of carbohydrates or from lactic and glycolic acids through ring-opening polymerization |
| **PVA** | Stable under a wide range of pH levels, temperature, and physiological conditions | biodegradable in both aerobic and anaerobic environments no toxic effects minimal cell adhesion great water solubility | tissue grafts, embolization materials, artificial organs, photonic crystal sensor materials, and drug delivery systems. 3D bioprinting scaffolds | synthesized through the partial or complete hydrolysis of polyvinyl acetate |

lineated the impact of molecular weight on polymer content, particle size, and magnetic behavior. Their main findings showed that elevated molecular weights of the polymeric chain correlated with increased quantities of higher oligomers within the MNPs. As the molecular weight escalated, the contribution of loops and tails intensified, thereby facilitating higher polymer contents. Regardless of the employed PAA molecular weight, the adsorbed PAA induced a reduction in particle hydrodynamic diameters and led to a narrower size distribution. The zeta potential values were more significantly influenced by the quantity of PAA adsorbed onto the iron oxides rather than by the PAA's molecular weight in the examined scenarios.

Additionally, Hu et al. investigated the synthesis and characterization of chitosan–PAA complex nanoparticles, highlighting their aqueous dispersion and stability.[257] Physicochemical properties were studied using exclusion chromatography, FTIR, dynamic light scattering, TEM, and zeta potential analysis. Chitosan–PAA nanoparticles were synthesized via two methods: polymerization of acrylic acid in chitosan solution and by mixing positively charged chitosan with negatively charged PAA using a dropping method. Drug-loaded nanoparticles were prepared by incubating silk peptide (SP) with chitosan–PAA nanoparticles synthesized via polymerization of acrylic acid in a chitosan solution. The study revealed that the molecular weight of PAA in nanoparticles increased with the molecular weight of chitosan, suggesting template polymerization of acrylic acid in a chitosan solution. Nanoparticles exhibited a positive charge and sizes ranging from 50 to 400 nm. Surface structure and zeta potential were modulated by different preparation methods. In vitro experiments demonstrated sustained release of entrapped SP over 10 days, with release behavior influenced by medium pH. The authors demonstrated different results from the synthesis of PAA-coated chitosan nanoparticles through different methods and chitosan solution pH, which caused distinct outcomes on surface structure and physical properties.

Furthermore, Jans et al. contributed to the understanding of PAA coatings through the synthesis and thorough characterization of PAA-coated AuNPs.[258] Their work revealed intriguing physical behaviors of PAA-coated AuNPs under diverse conditions, including sensitivity to ions, pH-induced conformational changes, and temperature responsiveness. First, the study observed the sensitivity of the PAA coating to $Na^+$ ions, with higher NaCl concentrations leading to coating shrinkage and subsequent nanoparticle aggregation due to dehydration. Scanning electron microscopy (SEM) analysis confirmed that the addition of 7 mM NaCl led to a considerable reduction in the thickness of the PAA coating on AuNPs. Second, pH-induced changes were observed, with the PAA coating transitioning between coiled and stretched conformations in response to varying pH levels. Furthermore, PAA-coated AuNPs demonstrated improved stability in acidic solutions compared to citrate-stabilized counterparts. Figure 13B outlines the pH-dependent behavior of citrate-stabilized AuNPs and PAA-coated AuNPs. Citrate-stabilized AuNPs exhibited a sigmoidal zeta potential trend, with increasing negative charge until an alkaline plateau at pH 5–12, correlating with deprotonation of carboxyl groups. In acidic conditions (pH 2–4), protonation decreased charges, causing particle aggregation. PAA-coated AuNPs remained stable at pH 4 with a negative zeta potential of −70 mV, decreasing slightly with higher pH. At acidic pH (<4), charges decreased, nearing the isoelectric

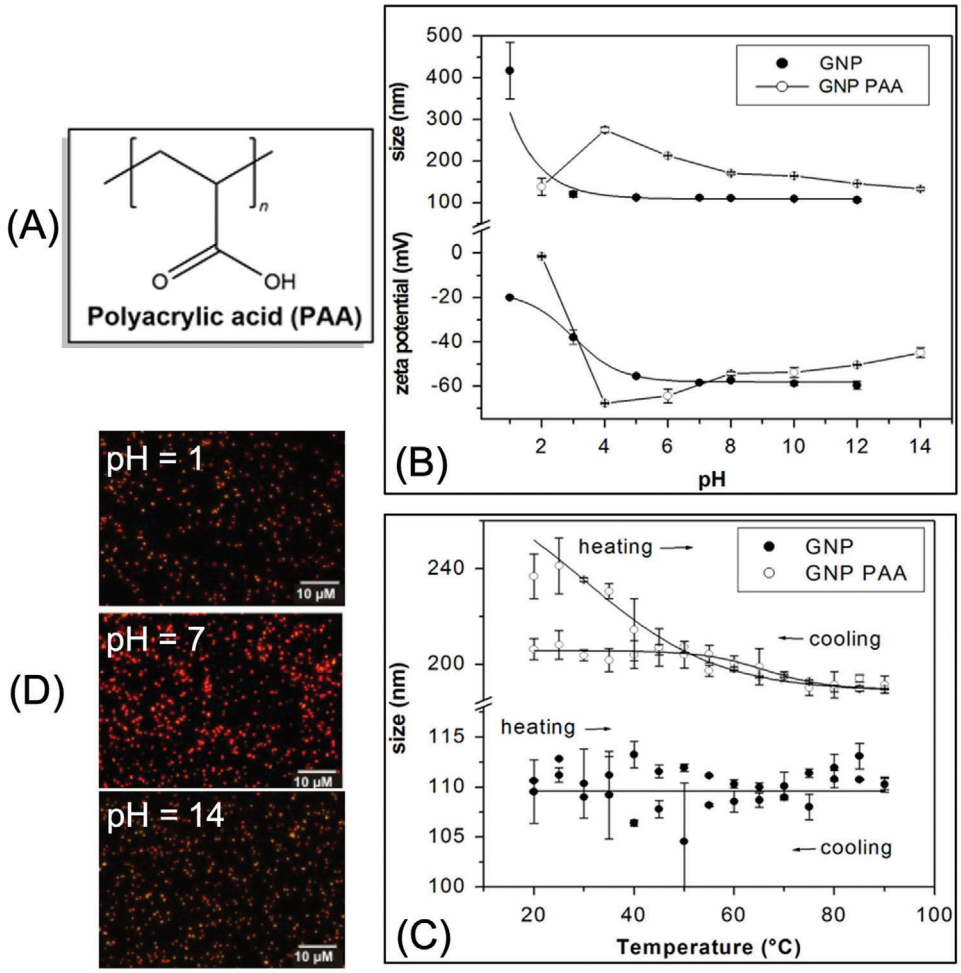


**Figure 13.** A) Molecular structure of PAA. Summary of the main results regarding the synthesis of PAA-coated AuNPs. B) Influence of pH of AuNPs solution before incubation on particle size and zeta potential for both citrate stabilized and coated AuNPs. C) Influence of temperature during the synthesis process of citrated-stabilized and PAA-AuNPs on particle size. D) Darkfield optical microscopy images of PAA-AuNPs in different pHs. A) Originally prepared by the authors. B–D) Reproduced with permission.[258] Copyright 2010, IOP Publishing Ltd.

point at pH 2. The addition of NaOH influenced zeta potential behavior.

Additionally, temperature variations affected the PAA layer, which contracted upon heating and expanded upon cooling of the suspension as depicted by Figure 13C. Figure 13D presents dark field images of PAA-coated AuNPs at various pH levels. Notably, at pH 1, the scattering intensity of PAA-coated AuNPs appeared significantly less bright compared to higher pH values. Corresponding sizes indicated that the brightest intensity corresponds to the largest spot size, thus suggesting reduced aggregation at pH 1. Overall, their findings offer valuable insights into the behavior of PAA-coated nanoparticles, collectively contributing to understanding the effects of PAA coating on the development of novel hybrid nanomaterials for diverse applications.

Overall, these studies highlight the significance of controlling both the synthesis methods and solution conditions (such as pH, ionic strength, etc.) to produce PAA-coated nanoparticles with desirable surface properties, including zeta potential, size distribution, surface groups, and coating thickness. These factors are crucial for their effective utilization in biomedical applications.

### *3.1.2. Polydopamine (PDA)*

Polydopamine (PDA) has garnered significant attention in biomedical applications owing to its remarkable biocompatibility and biodegradability.[259] Derived from mussel adhesive proteins, PDA exhibits strong wet adhesion to substrates, making it an ideal material for various biomedical uses. Its inherent antibacterial properties, combined with excellent biocompatibility and an environmentally friendly preparation process, position PDA as a promising antibacterial material.[260] Moreover, PDA-derived nanomaterials can be used for simultaneous diagnosis and therapy when combined with other materials, as has been recently reported in the literature for tumor ablation in animal models, highlighting the outstanding properties of PDA nanocomposites. More specifically, these nanoparticles have shown enhanced photothermal performance, prolonged circulation time, multimodal imaging capabilities, improved mucopenetration as well as increased cellular uptake and good safety profiles when combined with multiple nanomaterials as presented in the following.

Cheng et al. explored leveraging PDA coating to enhance manganese-based nanoparticle contrast and facilitate photothermal therapy (PTT).[261] They developed $MnCO_3$@PDA core-shell nanocomposites for potential MRI/PTT theranostics. The study showed an increase in $MnCO_3$@PDA nanoparticles' longitudinal relaxivity from 5.7 to 8.3 $mM^{-1}$ $s^{-1}$. Longitudinal relaxation, where tissue protons return to equilibrium after MRI excitation, was enhanced by PDA coating, yielding 6.3 $mM^{-1}$ $s^{-1}$ at pH 7.4 and 8.3 $mM^{-1}$ $s^{-1}$ at pH 6.0. Improved relaxivity enhances contrast agent efficiency, yielding clearer MRI images with better tissue contrast. In vitro studies validated $MnCO_3$@PDA's efficacy as an MRI/PTT agent, while in vivo experiments demonstrated MRI-guided tumor ablation in mice, showcasing high-resolution imaging and effective PTT. PDA-coated nanoparticles exhibited excellent biocompatibility and photothermal conversion efficiency, enhancing both MRI contrast and PTT efficacy. These findings elevated $MnCO_3$@PDA nanocomposites' potential as robust theranostic agents for enhanced MRI-guided PTT, promising advances in early tumor diagnosis and treatment.

Approaching a different type of hybrid nanostructure, the study by Liu et al. addressed the limitations of AuNRs in tumor theranostics due to poor stability, toxicity, and rapid immune system clearance.[262] They developed Cu(II)-doped PDA-coated AuNRs (AuNR@CuPDA) to enhance their potential in tumor theranostics. Using a seed-mediated method, AuNRs were synthesized and further coated with Cu(II)-doped PDA. Compared to AuNRs, AuNR@CuPDA exhibited improved photothermal performance, evidenced by a redshift and intensity increase in the absorption spectra. The PDA coating extended the half-life of AuNRs from 0.7 to 4.5 h in circulation, leading to a tumor uptake rate of 4.6%. Additionally, Cu (II) in the PDA shell shortened the T1 of surrounding protons, enabling tumor site visualization under T1-weighted MRI. The loading of Cu(II) in the PDA shell provided AuNR@CuPDA with MRI capability, in addition to computed tomography imaging. Moreover, Cu(II) in the PDA shell demonstrated chemotherapeutic properties, with a tumor inhibitor rate of 31.2%. Safety assessments including liver and renal function tests and histological analysis of major organs confirmed the safety of AuNR@CuPDA. Overall, the study demonstrated that Cu(II)-doped PDA-coated AuNRs are promising for tumor theranostics, offering enhanced photothermal performance, prolonged circulation time, multimodal imaging capabilities, and therapeutic efficacy with good safety profiles.

Poinard et al. focused on addressing the limitations posed by mucus, a natural barrier, to the effective delivery of therapeutic carriers to mucosal cells.[263] While PEGylation is a commonly used surface modification strategy to enhance mucopenetration, it often fails to improve cell uptake of nanoparticles. In this research, the authors explored PDA coating as an alternative approach to enhance both mucopenetration and cell uptake of nanoparticles. They polymerized PDA on carboxylated polystyrene (PS) nanoparticles to form a PDA coating, resulting in PS-PDA nanoparticles. The PS-PDA particles exhibited similar mucopenetration levels as PEGylated PS (PS-PEG) particles but demonstrated nearly three times higher cell uptake in T24 cells, a model for underlying mucosal cells. This improvement in cell uptake by PS-PDA was attributed to the interactions between the PDA coating and the cellular membrane. It was hypothesized that the positively charged amino groups of PDA facilitated interaction with negatively charged phosphate groups on the cell membrane, while the negatively charged phenol groups on the PDA surface interacted with positively charged choline groups on the lipid membrane, promoting cellular uptake. In contrast, the neutral charge of PEG limited its interaction with the cell membrane, resulting in minimal cell uptake of PS-PEG nanoparticles. Additionally, PS-PDA nanoparticles showed efficient mucopenetration, with slower diffusion rates compared to bare PS nanoparticles but faster diffusion rates than PS-PEG particles in reconstituted mucus solution. These findings suggest that PDA coating offers a novel functionality for enhancing both mucopenetration and cell uptake of nanoparticles for mucosal drug delivery applications, which is not achievable with conventional PEGylation strategies. The study positions PDA as a promising material for efficient mucosal delivery of therapeutics, particularly for cancer cell targets, potentially improving the efficacy of combined photodynamic and photothermal therapies.

More recently, Niyonshuti et al. investigated how PDA coating affects the antimicrobial activity of AgNPs.[264] The main results of this study are summarized in **Figure 14** to corroborate the observed enhanced antibacterial activity of PDA-coated AgNPs. It was argued by the authors that PDA was selected for its adhesive properties, chemical functionalities, and biocompatibility suitable for biological applications. By employing a polymeric synthesis and deposition method, PDA-AgNPs were synthesized with controllable coating thicknesses (Figure 14A) ranging from 3 to 25 nm. TEM images of PDA-AgNPs at varying coating times (labeled as PDA($\lambda$)-AgNPs, where $\lambda$ denotes the coating time in minutes) are organized in Figure 14A: a1, a2, a3. PVP-AgNPs exhibited an average size of 32 nm and, after PDA coating, the AgNPs' size increased to 36 nm for PDA5-AgNPs, 43 nm for PDA15-AgNPs, and 54 nm for PDA30-AgNPs, thus escalating with longer deposition times. The study systematically investigated the impact of dopamine self-polymerization degree on antimicrobial activity, correlating it with the physicochemical properties of functionalized AgNPs. Assessment via fluorescence-based growth curve assays on *E. coli* revealed that PDA-AgNPs exhibited significantly higher antibacterial efficacy compared to PVP-passivated AgNPs (PVP-AgNPs) and PDA alone. This observation is exemplified in Figure 14B for PDA-coated AgNPs with different thicknesses.

Notably, the PDA coating synergistically enhanced the potency of PDA-AgNPs against bacteria. Analysis using X-ray photoelectron spectroscopy and FTIR spectroscopy unveiled that the synergistic effects stemmed from the interaction/coordination between Ag and the catechol group on the PDA coating. These interactions boosted the generation of reactive oxygen species (ROS), leading to increased bacterial damage. By utilizing MitoTracker Green FM dye to stain the bacterial membrane, the authors observed a noticeable increase in the brightness of the bacterial membrane upon exposure to PDA15-AgNPs (Figure 14C), indicating a change in bacterial membrane electrical potential. Their analysis unraveled that while increased brightness was observed for all treated bacteria, those treated with PDA15-AgNPs exhibited the highest intensity increase. Their findings bring to light the pivotal role of surface effects in modulating the antimicrobial properties of AgNPs. The study highlighted the significance of surface coating in enhancing the antimicrobial activity of AgNPs and shed light on the underlying mechanisms driving the syner-

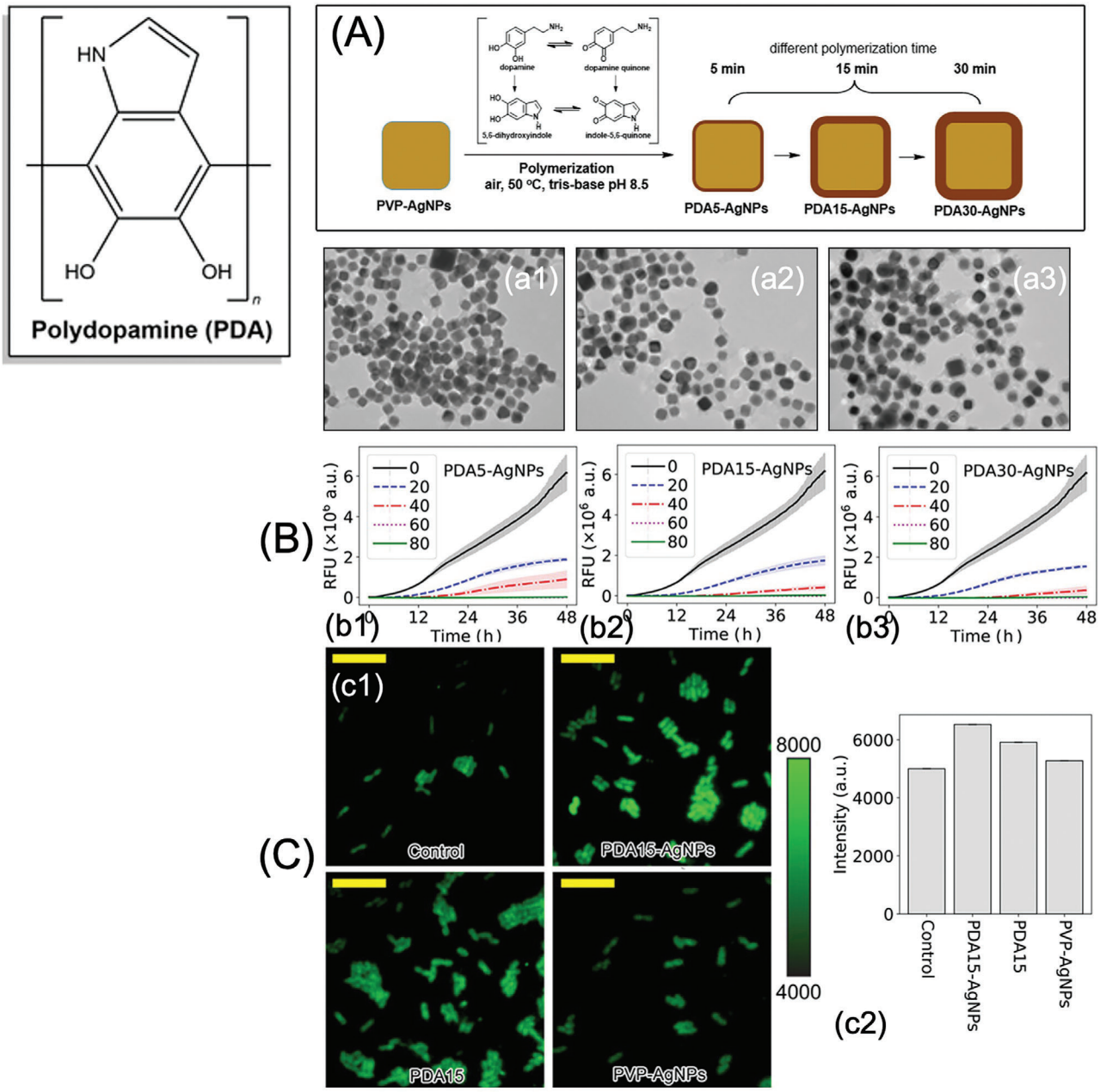


**Figure 14.** Summary of the main results of antibacterial activity studies using synthesized PDA-AgNPs. A) PDA deposition over AgNPs as a function of polymerization reaction time length and TEM characterization images of PDA-AgNPs for reaction times of a1) 5 min, a2) 15 min, and a3) 30 min; B) Timely fluorescence-based growth patterns of bacteria treated with b1) PDA5-AgNPs, b2) PDA15-AgNPs, and b3) PDA30-AgNPs. C, c1) Fluorescent images of bacteria stained with MitoTracker Green FM dye for control, PVP-AgNPs, PDA15, and PDA15-AgNPs along with c2) respective mean fluorescence intensities of the MitoTracker stained bacteria. Reproduced with permission.[264] Copyright 2020, American Chemical Society.

gistic effects between PDA and AgNPs, offering insights for the development of potent antimicrobial agents with broad applications in various biomedical fields.

### *3.1.3. Poly-L-Lysine (PLL)*

Poly-L-lysine (PLL) is a synthetic amino acid chain with a positive charge, featuring one hydrobromide per unit of lysine. Due to its positively charged amino groups under specific pH conditions, PLL can form soluble complexes with negatively charged macromolecules, enabling it to coat a wide range of surfaces effectively. PLL possesses intrinsic biodegradability, cationic charging properties, and easy functionalization capabilities, rendering it an excellent choice for biomedical applications.[265] This coating capability extends to cell membranes, where PLL's positive charge facilitates its entry into cells, enhancing cellular interactions.[266] Furthermore, PLL can form polyelectrolyte com-

 

plexes with DNA, making it an effective gene carrier for transfection purposes.[267,268] Several examples of the applications of PLL as a surface coating for nanoparticles are explored in the next lines.

Wang et al. presented the synthesis of fluorescent core-shell nanoparticles composed of a silver core and a PLL polymer shell.[269] The fluorescent anticancer drug, doxorubicin (DOX), was incorporated into the PLL shell via a primary amine-reactive cross-linker (DTSSP). The presence of a thiol-reducible disulfide bond in DTSSP allowed for the controlled release of DOX upon stimulation with glutathione (GSH). The premodification of the silver core with amino groups facilitated the PLL shell coating, enhancing the separation efficiency of the nanoparticles from the reaction mixture via centrifugation. The size of the prepared core-shell nanoparticles was tailored to ensure rapid internalization into cells, as demonstrated by cellular imaging assays. The results highlighted the potential of Ag@PLL-DOX nanoparticles as smart containers for specific drug-delivery applications and cellular imaging. Furthermore, cell viability assays demonstrated the nanoparticles' ability to internalize into cells and their intracellular drug-release capability, with high cell viability observed even after 1.5 h of incubation, indicating good biocompatibility. Both drug release and cell viability assays indicated that the nanoparticles exhibited good biocompatibility before the release of DOX at low GSH concentrations, while efficiently terminating cancer cells at increased concentrations.

In the following year, Wang et al. focused on the green synthesis of fluorescent core-shell nanoparticles using tryptophan as a reducing agent for the synthesis of gold cores and the deposition of PLL as a biocompatible shell.[270] The nanoparticles exhibited fluorescence enhancement upon conjugation with a cyanine dye, indicating successful functionalization. Furthermore, peptides containing the arginine–glycine–aspartic acid sequence were bound to the shell to serve as targeting ligands. Cell imaging assays demonstrated the efficient targeting of integrin-positive cells by the nanoparticles, highlighting their potential for cellular imaging and targeted detection of integrins. The synthesized hybrid nanoparticles, comprising an Au@PLL core–shell nanostructure, exhibited high specificity in targeting integrin $\alpha v\beta 3$-overexpressed cancer cells, as evidenced by cell imaging assays. The large number of amino groups on the PLL shell facilitated the binding of fluorescent dye Cy3-NHS and targeting ligand RGDyC, resulting in fluorescence enhancement compared to free Cy3 molecules. Importantly, the nanoparticles displayed low cytotoxicity due to the use of green reagents in the synthesis process, enhancing their biocompatibility. The study demonstrated the feasibility of synthesizing fluorescent core-shell nanoparticles via a facile and environmentally friendly method. The functionalized nanoparticles showed promise for specific cellular imaging and targeted detection of integrins, highlighting their potential applications in biomedical research and diagnostics.

Moreover, PLL is beneficial for preventing bacterial colonization on medical equipment due to its antibacterial properties.[271,272] It also enhances cell adhesion and proliferation in tissue engineering, which is crucial for tissue regeneration.[273] Additionally, PLL-mediated delivery of RNA-based therapies holds promise for revolutionizing the treatment of cancer and genetic disorders.[274] Furthermore, PLL can produce stimuli-responsive materials for precise drug delivery and multifunctional nanoparticles for combined therapeutic and diagnostic applications.[275] These attributes highlight PLL's extensive potential for biomedical innovation.

More recently, Siow et al. investigated the role of PLL coating in enhancing the uptake of MNPs by tumor cells and explored the underlying molecular mechanisms.[266] The results of this study are organized and summarized in **Figure 15**. PLL-coated MNPs with positive ($MNP^+$) and negative ($MNP^-$) zeta potentials were synthesized according to the basic sequential steps organized in Figure 15B and further characterized. Figures 15A: a1 and a2 show TEM characterization images of PLL-coated $MNPs^-$ and $MNPs^+$, respectively.

From those, the authors argued that the coating of primary iron oxide colloids with PLL preserved their morphology and size, as shown in Figure 15C. However, the hydrodynamic particle diameter of PLL-MNPs (79 nm) measured by DLS exceeded TEM measurements due to statistical differences and hydration layer inclusion. Both methods yielded low polydispersity values (PI ~0.15), indicating uniformity. They concluded that the PLL coating did not alter the iron oxide crystallites significantly, highlighting their stability. Cellular internalization of PLL-coated MNPs was analyzed using confocal microscopy and TEM, while a colorimetric iron assay was employed to quantify cell-associated MNPs (MNP-Cell). Results revealed that PLL significantly increased MNP-Cell in human glioma and HeLa cells in a concentration-dependent manner, regardless of the zeta potential of PLL-MNPs. Interestingly, the application of a magnetic field attenuated the PLL-induced increase in MNP-Cell. The study highlighted that the PLL coating interacted with heparan sulfate proteoglycans on the cell surface, facilitating MNP internalization by tumor cells. The amino groups of PLL selectively interacted with negatively charged residues of glycoconjugates, suggesting a molecular mechanism shared by certain viruses' infection machinery. Importantly, the study emphasized that the charged functional groups of PLL, rather than its zeta potential, played a crucial role in MNP internalization. Following, a temperature-dependence study was performed with U87MG cells that were exposed to the various synthesized MNPs at both 37 and 4 °C for 3 h. The results of this study are summarized in Figure 15D and suggest a significant reduction in MNP uptake by cells at 4 °C compared to 37 °C. Specifically, MNP uptake decreased by 36% when MNPs were alone and by 74% when combined with free PLL at 4 °C. This suggests a temperature-dependent component to MNP uptake by cells. Additionally, Figure 15E depicts the augmented internalization of dextran (Dex)-MNPs into U87MG cells facilitated by PLL treatment. Confocal microscopy (upper colored images of Figure 15E) revealed Dex-MNPs primarily localized in the cytosol. With PLL-coating, the fluorescence intensity increased by 3.4-fold compared to the control. TEM images (lower images of Figure 15E) confirmed the MNPs accumulation in cytoplasmic vesicles post 24-hour PLL incubation, with increased vesicle size and number per cell. Surprisingly, magnetic field application with PLL reduced the vesicle size and numbers/cells, contrary to expectations. Overall, the findings suggest that PLL-coated MNPs hold potential as drug carriers for targeting tumors inaccessible to magnetic targeting, with PLL interacting selectively with glycoconjugates on tumor cells to facilitate internalization.

PLL stands out as a versatile biomedical polymer due to its favorable characteristics and facile functionalization. Its posi-

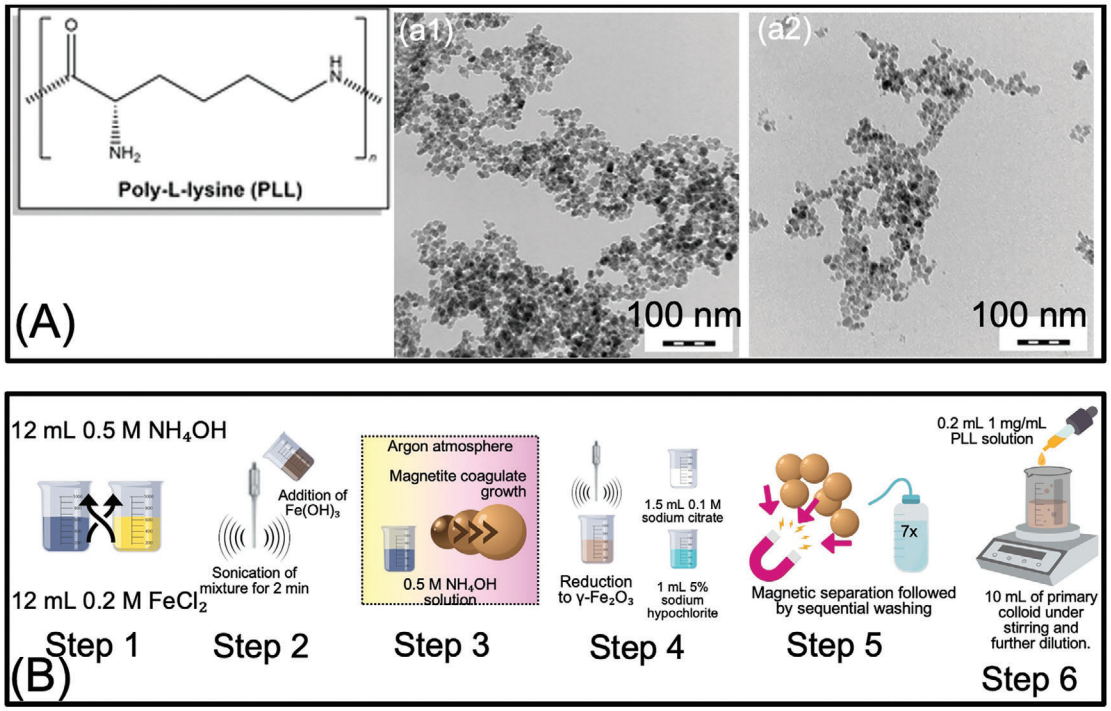


(C)

| MNPs | Polymer | $D_n$, nm (TEM) | PDI (TEM) | $D_h$, nm (DLS) | PI (DLS) | ζ-Potential (mV) | pH |
|---|---|---|---|---|---|---|---|
| Dex-MNPs[a] | Dex | | | 263.7±5.5 | | −40.1±0.3 | |
| MNPs$^-$ | – | 9.7 | 1.22 | 79.3±0.1 | 0.124±0.02 | −56±2 | 8.25 |
| PLL-MNPs$^-$ | PLL | 10.1 | 1.19 | 119±3 | 0.25±0.02 | −47±1 | 7.9 |
| MNPs$^+$ | – | 9.6 | 1.23 | 70.7±0.3 | 0.123±0.004 | 57±4 | 4.09 |
| PLL-MNPs$^+$ | PLL | 10.2 | 1.19 | 69±2 | 0.145±0.006 | 61±1 | 4.13 |

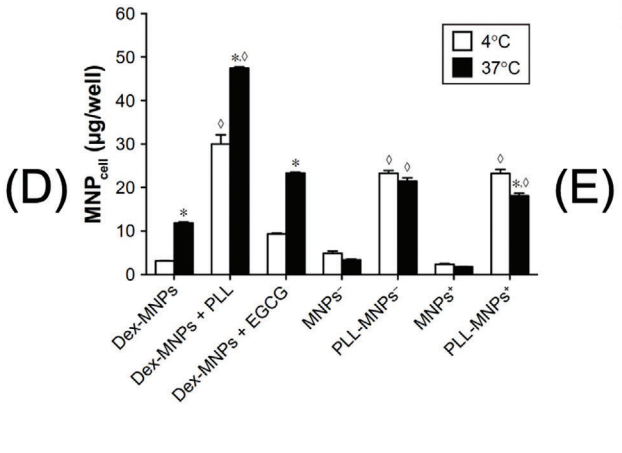


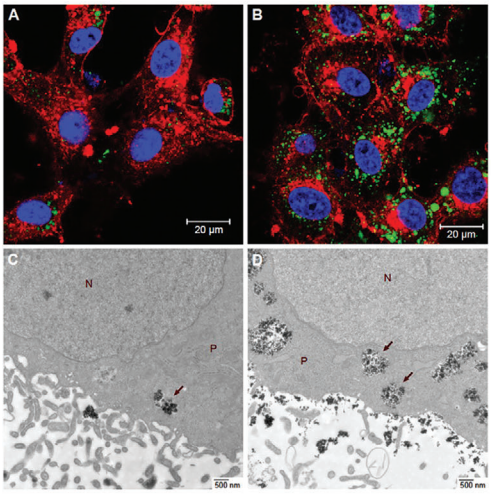


**Figure 15.** Summary of the main results of internalization studies of PLL-coated maghemite particles by tumor cells. A) TEM characterization images of a1) negative zeta potential and a2) positive zeta potential of synthesized PLL-MNPs. B) Experimental synthesis approach followed by the authors. C) Main physicochemical characteristics of bare and coated MNPs. D) Effect of temperature on the uptake of various synthesized MNPs. E) Visual evidence and quantitative analysis of the effects of PLL on the internalization of Dex-MNPs in U87MG cells, with representative confocal microscopy (A,B) and TEM (C,D) images illustrating the changes in internalization and vesicle characteristics under different experimental conditions (in the absence (A,C) and presence (B,D) of 3 nM PLL for 1 and 24 h, respectively). A,C,D) Reproduced with permission,[266] under a Creative Commons license CC BY-NC 4.0.

tively charged amino groups enable effective coating of surfaces and interaction with cell membranes, enhancing cellular uptake. PLL's ability to form complexes with DNA further extends its utility as a gene carrier. Specifically, PLL-coated MNPs exhibit promise in drug delivery and cellular imaging applications. Studies have demonstrated controlled drug release from PLL-coated MNPs, highlighting their potential as smart drug delivery systems. Moreover, PLL-coated MNPs show low cytotoxicity and high specificity in targeting cancer cells, emphasizing their potential in targeted therapy and diagnostics. Understanding PLL's interaction with glycoconjugates on cell surfaces provides insights into its mechanism of action and further enhances its application in biomedical research.

#### 3.1.4. Polyethylene Glycol (PEG)

Polyethylene glycol (PEG) is a linear polyether macromolecule known for its hydrophilicity, lack of charge, and non-immunogenic properties. PEG synthesis typically involves anionic polymerization of ethylene oxide with hydroxyl initiators, which may originate from various sources such as water, ethylene glycol, or diols. Alternatively, PEG can be obtained through the ring-opening polymerization of epoxyethane. Linear PEG molecules possess only two functional groups, limiting their potential for further derivatization, conjugation with other residues, or targeting ligands. To overcome this limitation, commercial PEGs are available with varying degrees of polymerization and activated functional groups, expanding their versatility in biomedical applications.[276] It is easy to conjugate PEG with functional groups since PEG has chemically active hydroxyl groups on both ends, which is a favored choice for biomedical and therapeutic applications.

The process of PEGylation involves the conjugation of biomolecules or nanoparticles with linear PEG through specific functional groups. This transformative process enhances the pharmacokinetic properties of peptides, proteins, hydrophobic polymers, drugs, or nanoparticles, leading to substantial improvements in their bioavailability and circulation time. Importantly, PEGylation has been shown to mitigate the toxicity associated with these materials, thereby enhancing their safety profile, and expanding their potential applications in various biomedical and therapeutic contexts. Also, PEG has minimal toxicity and efficient elimination from the body, which occurs primarily through renal excretion for PEGs below 30 kDa and via fecal excretion for PEGs exceeding 20 kDa. Moreover, among synthetic polymers, PEG stands out as the most commonly utilized material for coating magnetic cores, particularly prized for its ability to confer high colloidal stability to nanomaterials.[277,278] After injection in the human body, nanoparticles are identified as foreign items, and the cells of the mononuclear phagocyte system quickly remove them from the bloodstream, preventing their buildup in target cells and tissues. However, PEG coatings prevent surface aggregation, opsonization, and phagocytosis—as was seen with PEGylated proteins—and hence lengthen the duration of blood circulation. The hydrophilic property of PEG chains results in the formation of a hydrated cloud with a large volume when grafted onto nanoparticles, which sterically prevents nanoparticles from interacting with adjacent nanoparticles and/or blood components.[279]

Moreover, while PEG coating is a common practice for MNPs, the process of passivating them onto AuNPs involves slight variations. This is because AuNPs possess a versatile surface chemistry including thiol (-SH) groups that makes them more receptive to such polymer modifications. Strong interactions between gold and sulfur allow surface functionalization via the Au–S bond,[280] making it easier to coat it with molecules containing -SH terminal groups, such as PEG with thiol groups, targeting agents, and imaging agents. As an alternative approach to this, proteins and polymers can be adsorbed onto the surface of AuNPs through nonspecific absorption via electrostatic interactions, increasing their usefulness and stability.[281–283] Alternatively, AuNPs can be further functionalized through multilayer coatings using layer-by-layer (LBL) assembly techniques or integrated with other functional components, increasing their versatility for biomedical applications.[284–286]

PEG significantly advances biomedical applications through its use in drug delivery systems and tissue engineering. To improve therapeutic efficacy and patient compliance, PEG-based hydrogels are essential for the development of controlled-release formulations. In these formulations, drugs are encapsulated within the hydrogel matrix and released over an extended period. These hydrogels can be engineered to respond to physiological cues such as pH, temperature, or enzymes, allowing for precise and specific drug delivery. In tissue engineering, PEG hydrogels serve as a biocompatible scaffold that promotes cell growth and tissue regeneration, making them ideal for wound healing, cartilage restoration, and the creation of artificial organs.[287,288] Additionally, PEG's ability to reduce protein adsorption and cell adhesion minimizes the risk of immune reactions, making it an excellent choice for coatings on implants and prosthetics to enhance their biocompatibility and longevity.[289]

In Xiao et al.'s study, the ultrasmall 3 nm-sized nanoparticles Mn-IONPs were prepared by the thermal decomposition of iron-eruciate and manganese-oleate complexes and were coated with 1,2-Distearoyl-sn-glycero-3-phosphoethanolamine-N-(methoxy [polyethylene glycol]-2000) (DSPE-PEG 2000).[290] The Mn-IONPs@PEG demonstrated good biocompatibility and outstanding hydrophilicity following DSPE-PEG coating. The Mn-IONPs@PEG exhibited good relaxivity in vitro because of the manganese doping and PEG coating. Particularly, the Mn-IONPs@PEG coated with DSPE-PEG following a mass ratio of 1:20 demonstrated harmonic transverse relaxivity ($r2$ = 120.9 mM $s^{-1}$) and longitudinal relaxivity ($r1$ = 7.1 mM $s^{-1}$), which improved its suitability for T1/T2 dual-contrast MRI (see **Figure 16**A. When administered through a caudal vein, Mn-IONPs@PEG could provide a notable enhancement in T1-weighted and T2-weighted MRI images. It was determined that the optimal time for imaging was 10 min post-injection, as both T1 and T2 enhancements were at their peak during that period (see Figure 16B).

#### 3.1.5. Poly(Lactic-Co-Glycolic) Acid (PLGA)

Poly(lactic-co-glycolic) acid (PLGA) is a linear copolymer that is typically produced by enzymatic fermentation of carbohydrates

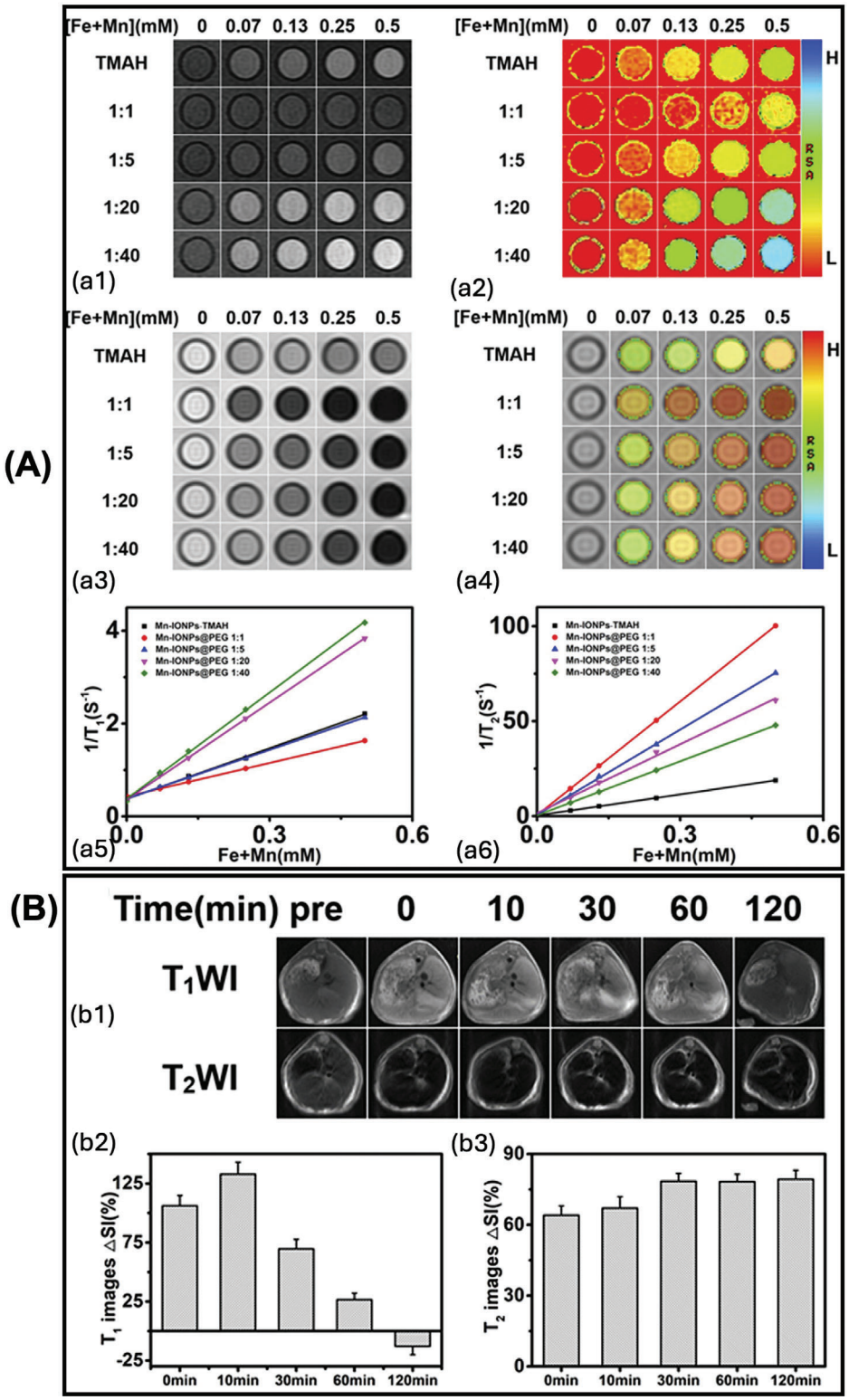


**Figure 16.** A) Mn-IONPs-TMAH and Mn-IONPs@PEG (1:1, 1:5, 1:20, and 1:40) in vitro MRI images at 3.0 T, a1) T1-weighted, a2) T1 mapping, a3) T2-weighted, a4) T2-mapping, a5,a6) Linear fitting of 1/T1 and 1/T2 over a range of nanocomposites (Fe+Mn) concentrations. B) Summary of contrast-enhanced MRI effects of Mn-IONPs, b1) T1- and T2-weighted MRI images of the liver's transverse planes obtained with the fast spin echo (FSE) sequence at 0, 10, 30, 60, or 120 min following the intravenous injection of Mn-IONPs@PEG (1:20). b2,b3) The liver's MRI signal intensity changes (ΔSI) enhancement ratio following contrast-enhancing with Mn-IONPs@PEG (1:20). Reproduced with permission,[290] under a Creative Commons license CC BY-NC 3.0.

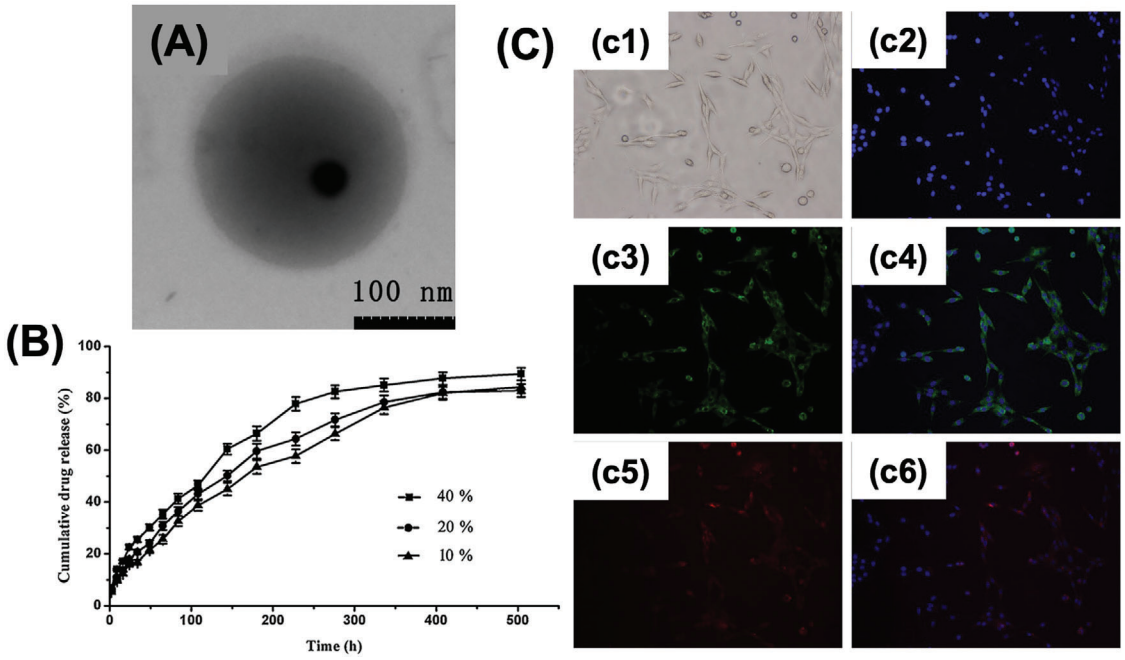


**Figure 17.** A) TEM micrograph of SPION/TMZ particles. B) Release of TMZ in vitro from P80-TMZ/SPIONs with 10%, 20%, and 40% drug loading. C) Fluorescence inverted microscopy of C6 cells incubated for 2 h with P80-RC/SPIONs and labeled by rhodamine and coumarin-6. The Hoechst was added to stain the nucleus. c1) Optical microscopy image of C6 cells after incubation with P80-RC/SPIONs; c2) blue fluorescent microscopy image of C6 cells with labeled nucleus; c3) green fluorescent microscopy image of C6 cells labeled by the nanoparticles with coumarin-6; c4) the composition of the previous fluorescent microscopy images; c5) red fluorescent microscopy image of C6 cells labeled by rhodamine particles; d6) the composition of blue and red fluorescent microscopy images. Reproduced with permission.[302] Copyright 2012, Elsevier B.V.

or synthesized from lactic and glycolic acids. PLGA is created by randomly opening the rings of two distinct monomers—cyclic dimers (1,4-dioxane-2,5-diones) of glycolic acid and lactic acid—and joining them together with ester linkages.[291] However, both carbohydrate and synthesized processes employ biologically derived, renewable basic materials to create PLGA. The molar ratio and the order in which the lactic and glycolic acids are arranged in the polymer chain define the physicochemical characteristics of the polylactic acid gel. The degree of interaction between macromolecules can be adjusted by using PLGA copolymers, which come in a variety of molecular weights and structures. Because of this, the physicochemical characteristics of PLGA might differ significantly based on the polymer's composition.[292,293] An adequate level of biocompatibility and biodegradability in aliphatic polyesters makes them the most widely used biodegradable polymers derived from non-natural sources. They are eliminated and excreted through the kidneys rather quickly because of their low molecular weight breakdown products' natural metabolism.[294]

PLGA has garnered significant attention as foundational material for biomedical applications owing to several key attributes including i) exceptional biocompatibility, which ensures minimal adverse reactions upon interaction with biological systems, ii) tailored biodegradation rates, modulated by controlling the molecular weight and copolymer ratio, enabling precise control over the degradation process, aligning with specific application requirements, iii) approval for clinical use in humans by regulatory authorities such as the U.S. Food and Drug Administration (FDA) which underscores its safety profile and suitability for medical applications, iv) the ability to modify the surface properties facilitates enhanced interactions with biological materials, optimizing performance in various biomedical contexts, v) importantly, PLGA offers an alternative to animal-derived products, aligning with cultural preferences and regulatory requirements in diverse geographic regions.[293,295]

PLGA is extensively used in advanced drug delivery systems, where it forms nanoparticles and microparticles capable of encapsulating a variety of therapeutic agents, including drugs, proteins, and nucleic acids, for controlled release and targeted delivery.[296,297] This application is particularly advantageous in cancer therapy, as PLGA nanoparticles can deliver chemotherapeutic agents directly to tumors, thereby reducing systemic toxicity.[298–300] Beyond drug delivery, PLGA is utilized in bioresorbable medical devices such as sutures, pins, screws, and plates, which degrade within the body, obviating the need for removal surgery.[301] Additionally, PLGA enhances immune responses in vaccine formulations and supports tissue and organ repair and regeneration in regenerative medicine, underscoring its versatility in biomedical applications.

In Ling et al.'s study, the emulsifying-solvent evaporation approach was successfully used to create temozolomide (TMZ)-loaded PLGA-based superparamagnetic nanoparticles, which were then surface-modified using polysorbate 80.[302] Superparamagnetic iron oxide was successfully incorporated into the polymer core, as shown by the TEM image in **Figure 17**A. Although it was not very clear, polysorbate 80 coating was seen on the surface of the PLGA-based nanoparticles. P80-TMZ/SPION nanoparticles demonstrated superior drug sustained release efficacy together with high drug loading and encapsulation efficiency

(Figure 17B). The 3-[4,5-dimethylthiazol-2-yl]-2,5 diphenyl tetrazolium bromide (MTT) assay was used to assess the cytotoxicity of TMZ, P80-TMZ-particles, and P80-TMZ/SPIONs. At the same concentrations, there was no discernible variation in the toxicity of the various formulations. Therefore, to quantify the cytotoxicity on glioma C6 cells, their work started with 20% of TMZ-loaded nanoparticles. Using a fluorescent inverted microscope, the intracellular distribution of nanoparticles in C6 glioma cells was examined after a 2-h incubation period. The nanoparticles were tagged with coumarin-6 and rhodamine and coated with polysorbate 80 (P80-RC/SPIONs), while Hoechst blue-fluorescent dye was used to stain the C6 nucleus. The distribution of the nanoparticles in the cellular environment was revealed by the images shown in Figure 17C. Thus, P80-TMZ/SPIONs could be used as a novel delivery method for tumor imaging, drug delivery, and real-time therapeutic impact monitoring, according to an in vitro experiment conducted on glioma C6 cells.

#### 3.1.6. Poly(Vinyl Alcohol) (PVA)

Polyvinyl alcohol (PVA) is a linear synthetic polymer synthesized through the partial or complete hydrolysis of polyvinyl acetate, resulting in the removal of acetate groups.[295] The degree of hydroxylation is an important factor in defining PVA's mechanical, chemical, and physical properties. Indeed, PVA is typically categorized into two main groups: partially hydrolyzed and fully hydrolyzed. The diverse range of PVA products stems from variations in the length of the initial vinyl acetate polymer and the extent of hydrolysis achieved under alkaline or acidic conditions. These factors contribute to a spectrum of PVA molecules with molecular weights spanning from 20 000 to 400 000. Consequently, PVA exhibits a wide array of characteristics including solubility, flexibility, tensile strength, and adhesiveness, each influenced by its specific molecular structure and composition.[303] This polymer is resistant to the majority of organic solvents and has great water solubility. Water solubility falls with increasing hydroxylation and polymerization, making PVA less prone to crystallization. PVA often must be crosslinked to create hydrogels to fully realize its promise in a variety of applications. Crosslinks, whether created chemically or physically, give the hydrogel structural stability, especially after it has swelled in water or biological fluids. It is biodegradable in both aerobic and anaerobic environments.[304] As a result, PVA finds extensive utility in the biomedical field, where its diverse properties render it indispensable for an array of applications. Notably, PVA serves as a fundamental constituent in the fabrication of numerous tissue grafts, including cardiovascular grafts, bone tissue scaffolds, and artificial skin. Moreover, its use extends to the development of embolization materials, artificial organs such as the pancreas and islets, and constructs for cartilage and vocal cord reconstruction. Additionally, PVA contributes to various biomedical innovations, such as photonic crystal sensor materials, ferrogels for artificial muscles, and pH-sensitive membranes. Its role in facilitating drug delivery through controlled release mechanisms underscores its significance in pharmaceutical applications.[303,305] Overall, PVA has emerged as a versatile material for advanced 3D bioprinting scaffolds in biomedical research.[306] Its biocompatibility, tunable mechanical properties, and solubility make it ideal for creating scaffolds with intricate architectures that mimic the natural tissue microenvironment.[307] PVA scaffolds facilitate nutrient diffusion and cell viability, while the incorporation of bioactive molecules enhances tissue regeneration potential. This innovative approach holds promise for personalized tissue engineering and regenerative medicine applications.[308]

In Darwish et al.'s research, the successful fabrication of MNPs coated with PVA was achieved through an ultrasonic-assisted coprecipitation technique (**Figure 18A**).[309] This coating process led to an enhanced dispersion of MNPs and a notable increase in the saturation magnetization value (45.08 emu $g^{-1}$; see Figure 18B). Importantly, the presence of the PVA shell not only improved the heating efficiency but also enhanced the hyperthermia properties of the MNPs. At high frequencies, PVA@MNPs exhibited the maximum specific loss power (SLP), reaching a value of 163.81 W $g^{-1}$, whereas bare MNPs displayed the lowest SLP of 4.84 W $g^{-1}$ (see Figure 18C). These findings underscore the promising self-heating properties of PVA@MNPs for hyperthermia applications.

#### 3.1.7. Copolymers

Copolymers are large molecules created by polymerizing two or more different monomers.[310] They can be classified into various types based on their structural arrangements and the sequence distribution of their monomers. These classifications include random or statistical copolymers, alternating polymers, and block copolymers (BCPs).[311] Among these, BCPs have attracted the most attention due to their amphiphilic nature, which drives them to self-assemble. This property makes them excellent candidates for nanoparticle coatings and useful in the biomedical field as drug carriers and surface modifiers.[312,313]

Among the various BCPs, PEG-PLGA offers more advantages compared to other amphiphilic BCPs like PS-PEG and PCL-PEG.[314] To date, numerous studies have highlighted the use of PEG-PLGA copolymers as nanoparticle coatings.[315,316] The widespread adoption of these copolymers stems from their outstanding biodegradability and biocompatibility. Additionally, both PEG and PLGA are FDA-approved, and PEG-PLGA copolymers are non-toxic post-hydrolysis.[314] PEG-PLGA-coated NPs are recognized as excellent drug carriers. Unlike unPEGylated PLGA NPs, PEG-PLGA coated NPs demonstrate significantly enhanced immune tolerance.[317]

The creation of PEG-PLGA nanoparticles primarily employs two main techniques: nanoprecipitation and double emulsion-solvent evaporation.[279] These methods leverage the natural self-assembly properties of PEG and PLGA under specific temperatures. Nanoprecipitation offers a straightforward approach for producing nanoparticles with a narrow size distribution, requiring minimal surfactant, producing minimal toxic byproducts, and enabling scalability. Eskandari et al. utilized the nanoprecipitation method to craft PEG-PLGA nanoparticles infused with a manganese complex. The resulting nanoparticles exhibited outstanding encapsulation and drug-loading efficiency, yielding promising therapeutic effects against breast cancer stem cells.[318] In the double emulsion-solvent evaporation method, PEG, PLGA, and drug are added into an organic solvent, where the evaporation of the organic solvent followed by filtration yields

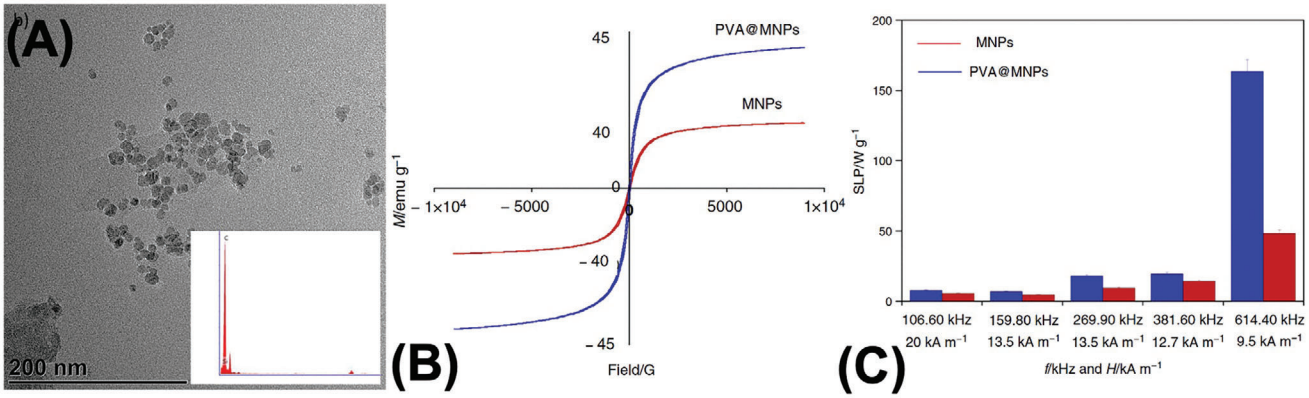


**Figure 18.** A) TEM images and energy dispersive X-ray analysis (EDAX) for PVA@MNPs. B) Magnetic characterization of MNPs and PVA@MNPs. C) Specific loss power (SLP) of MNPs and PVA@MNPs. Reproduced with permission,[309] under a Creative Commons license CC BY 4.0.

drug-loaded PEG-PLGA NPs.[319] Fang et al. employed this approach to formulate PEG-PLGA NPs loaded with salidroside, achieving remarkable entrapment efficiency through fine-tuning the molar ratio of glycolic acid/lactic acid and the molecular weight of PLGA. The resultant formulation exhibited minimal polydispersity, elevated zeta potential, and demonstrated favorable release kinetics and cytotoxicity profiles in vitro. These findings underscore the critical influence of composition and selection of raw materials on the performance of PEG-PLGA NPs.[320]

### 3.2. Natural Polymer Coatings

Significant research has been conducted on utilizing natural polymers or biopolymers for nanoparticle surface coatings to overcome the limitations of synthetic polymers, such as their non-biodegradability and toxicity.[321] Derived from living organic matter, the most common natural polymers utilized in biomedical applications include polysaccharides (alginate, chitosan, dextran) and proteins (collagen, fibrin, gelatin).[322] The advantages of biopolymers include non-toxicity, chemical inertness, biodegradability, and high biocompatibility.[323] The functional groups present in these biopolymers, such as hydroxyl, amino, and carboxyl groups, can be chemically modified to impart enhanced performance properties to the nanoparticles.[277,324]

One common natural polymer that has been extensively investigated for its use as a surface coating is chitosan. Chitosan is a linear polysaccharide produced from the deacetylation of chitin, a polymer found in the exoskeleton of crustaceans.[325] Chitosan-coated nanoparticles have been employed in various biomedical applications including wound healing, tissue engineering, and drug and vaccine delivery.[326] Pham et al. developed magnetic nanoparticles coated with a polymeric shell of chitosan with active amino groups that could bind to curcumin, an anticancer drug.[327] Chitosan confers many advantages to nanocarriers, including improved bioadhesive capacity, cellular uptake, drug bioavailability, and controlled drug release.[325,326] The aforementioned study determined that the maximum curcumin loading time was 120 min and 70% of the drug was released after 2800 min in a phosphate buffer solution at a pH of 7.4 and a temperature of 37 °C.[327] In another study, Bhumkar et al. developed chitosan-coated gold nanoparticles for the transmucosal delivery of an insulin peptide. With a 53% loading efficiency, there was a 30.41% and 34.12% reduction in the blood glucose levels of diabetic Wistar rats after 3 h with a dose of 10 IU $kg^{-1}$ via oral and nasal administration respectively.[328]

Another natural polymer that has gained significant interest in recent years is gelatin, a protein derived from the partial hydrolysis of collagen. Gelatin-coated nanoparticles have been widely studied in drug delivery nanosystems, since gelatin can release drugs at the target site in the presence of an internal or external stimulus, such as pH, temperature, or irradiation.[329,330] A study done by Gaihre et al. investigated the drug loading efficiency of gelatin-coated magnetic nanoparticles and the release of the drug in an acidic or basic medium.[331] Using doxorubicin as the model drug, this study determined that the encapsulation efficiency of gelatin A and gelatin B coated nanoparticles was 41.9% and 67.5% respectively, when the drug loading was done by desolvation. In the absence of an enzyme, 32% and 61% of the drug was released in acidic and basic medium respectively, with an extra 34% and 43% release in the presence of an enzyme. In another similar study, Suarasan et al. developed gelatin-coated gold nanospheres to act as a carrier for doxorubicin.[330] It was determined that ≈80% of the drug was released after 24 h at a pH of 4.6, which corresponded to the acidic region of a tumor but only 25% of the drug was released at a pH of 7.4 for the same amount of time, indicating their stability at physiological pH. These doxorubicin-loaded nanoparticles killed 39% and 48% of MCF-7 breast cancer cells in vitro after 24 and 48 h respectively.

### 3.3. Cell Membrane Coatings

While synthetic techniques have improved the performances of nanoparticles, their inherent complexity hinders them from replicating intricate biological systems. Consequently, this has motivated researchers to use biomimicry approaches as a guiding principle in developing advanced nanoplatforms.[332–336] Biomimetic coatings offer a promising avenue by emulating nature's mechanisms and interactions. Cell membranes, composed of lipids, proteins, and carbohydrates, play vital roles in cellular functions like adhesion, signaling, and recognition. Coating

particles with naturally derived cell membranes offers a promising biomimetic particle engineering approach, imparting specific cell-like properties to nanoparticles.[337–340] Although synthetic biomaterials mimicking cell membranes exist, they often fail to fully replicate the complex structure and protein composition of natural cell membranes. In contrast, coating particles with naturally derived cell membranes presents a top-down design approach that overcomes this limitation.[341,342]

In 2011, Hu et al. showcased a groundbreaking advancement by applying cell-membrane coating on nanoparticles, utilizing membranes from red blood cells (RBCs).[343] RBCs possess an extended circulation lifespan, attributed to their abundance of CD47 proteins on their surface. To obtain the RBC membranes, the researchers lysed RBCs to create membrane ghosts, which were then extruded to isolate the membranes. These RBC membranes were subsequently coated onto polymeric nanoparticles via a co-extrusion technique. The resulting RBC membrane-coated nanoparticles exhibited significantly prolonged circulation in mouse models, boasting an elimination half-life of ≈40 h. This study underscored the potential of cell membrane coating in nanoparticle functionalization for drug delivery and various biomedical applications, including phototherapy, paving the way for numerous future avenues of research and development.[146,344,345] Since then several cell membrane coatings have been developed including cell membranes derived from cancer cells, platelets, white blood cells, etc. However, in this review, we will exclusively focus on RBC membrane-coated NPs or Cm-NPs. Thus, compared to traditional polymeric coatings like PEG, cell-membrane-coated nanoparticles (Cm-NPs) offer an alternative strategy for engineering stealth nanoparticles, potentially surpassing current approaches in effectiveness.

The preparation of Cm-NPs entails three primary steps: extraction of membrane from natural cells, development of the inner core nanocarriers, and the fusion process that brings the two components together (figure 3 of ref. [346]).

#### 3.3.1. Membrane Extraction

Cell-membrane consisting of phospholipids and surface proteins are pivotal in various biological functions like transport and cell recognition.[347] Gentle membrane extraction involves lysis and purification methods tailored to cell types.[348] For nucleus-free cells like mature RBCs and platelets, extraction involves hypotonic treatment and freezing/thawing cycles. Eukaryotic cell extraction, e.g., leukocytes and cancer cells, is more complex, involving isolation, culture, and a combination of lysis, centrifugation, and washing steps.

#### 3.3.2. Selection of Inner Core Nanocarriers

One of the integral parts of developing Cm-NPs is the selection of inner core nanocarriers that serve as the payload to be delivered to targeted solid tumors. Several materials like gold, iron oxide, PLGA, or liposomes have been explored for encapsulation with cell membranes.[349–356] The selection of the inner core nanocarrier should align with specific cargo delivery needs. Organic nanocarriers composed of lipids and polymers like PLGA, are FDA-approved due to their biocompatibility and high drug loading capacity.[357] Liposomes, also widely used, have entered clinical trials and received FDA approval for specific indications.[358] Inorganic inner nanocarriers offer several advantages which include low cost, control over surface properties, and ease of synthesis. They exhibit high-loading capabilities for cytotoxic reactive oxygen species in applications like photodynamic therapy.

#### 3.3.3. Membrane Fusion Process

To create Cm-NPs, the membrane and inner core nanocarriers must be combined using a fusion process (**Figure 19A**). This process allows the core to be enveloped by the cell membrane, resulting in Cm-NPs. Currently, three fusion techniques have been used which include, membrane extrusion, ultrasonic fusion, and electroporation. Membrane extrusion and ultrasonic treatment are predominant techniques. In membrane extrusion, both the membrane and core are pushed multiple times through a nanoscale porous membrane using a mini extruder. This mechanical process coats the NPs with the membrane effectively, though it is challenging to scale up for large production.[359] Ultrasound fusion involves co-incubation of core and membrane components and consequently subjecting them to the sonication process. While this method can generate Cm-NPs, the resulting particles may vary in size and are often associated with a high degree of polydispersity index.[360] With rapid advancements in microfluidic technologies, a microfluidic electroporation approach has been developed where components are mixed in a Y-shaped channel and then subjected to electroporation.[361] With proper optimization, this technique has shown promise in efficiently and reliably generating Cm-NPs.

#### 3.3.4. Photophysical and Biophysical Characterization of Cm-NPs

The assessment of Cm-NPs involves analyzing their physical and biological traits to confirm the successful coating of cell membranes onto NP. This includes evaluating NP size, surface charge, and protein composition. The coating process alters NP size and surface charge, which can be observed through particle characterization techniques. For instance, dynamic light scattering shows an increase in hydrodynamic diameter for the Cm-coated NPs compared to uncoated ones (Figure 19B,C). Correspondingly, transmission electron microscopy (TEM) images typically show a diameter increase of ≈10–20 nm in Cm-NPs compared to uncoated ones (Figure 19D). Zeta potential measurements indicate changes in surface potential before and after coating; for example, in one study, the zeta potential increased by ≈10 mV after coating with a red blood cell (RBC) membrane (Figure 19E). It is also imperative to verify the biological functionality of the cell membrane to ensure effective NP coating. Techniques like fluorescence antibody staining (Figure 19G) Western blotting and dot blotting (Figure 19H,I) have been used to confirm the presence of specific surface proteins on coated NPs. For example, CD47, a marker for RBC membrane, was detected on the surface of RBC membrane-coated NPs (RBCM-coated Cm-NPs). Additionally, SDS-PAGE analysis showed consistent protein levels across different stages of NP fabrication, confirming the presence of membrane proteins on RBCM-coated Cm-NPs (Figure 19J).

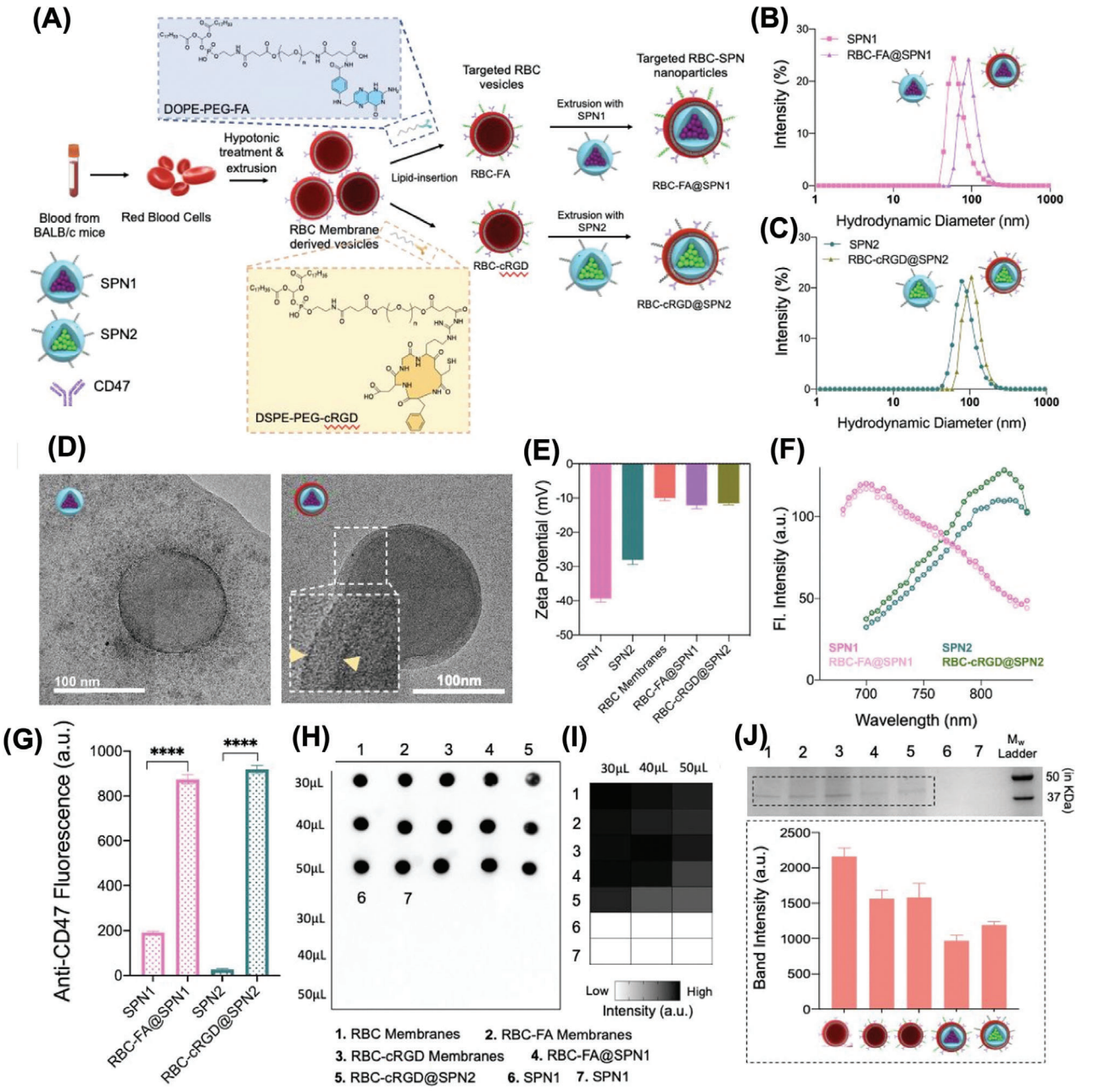


**Figure 19.** Preparation of ligand-modified RBC-SPNs and their physicochemical, optical, and biophysical characterizations. A) Schematic illustration of the RBC membrane extraction, lipid insertion with tumor-targeting peptides, and finally coating it onto SPNs. Hydrodynamic diameter measurements for B) SPN1, RBC-FA@SPN1, and C) SPN2, RBC-cRGD@SPN2. D) Negative stained TEM images of SPN1 and RBC-FA@SPN1. E) $\zeta$ potential measurements and F) fluorescence emission spectra of SPN1, RBC-FA@SPN1 (Ex. 645nm) and SPN2, RBC- cRGD@SPN2 (Ex. 645nm). G) SPNs and RBC-SPNs were stained with a fluorescent anti-CD47 antibody. H,I) Dot blot studies for different samples (RBC membranes, SPNs, RBC-SPNs) to show the presence or absence of the CD-47 proteins. J) SDS-PAGE protein analysis by Coomassie blue staining of RBC membranes, SPNs, and RBC-SPNs with Mw as the molecular ladder to show expression of CD-47 proteins. Reproduced with permission.[362] Copyright 2023, American Chemical Society.

In summary, the process of preparing and characterizing Cm-NPs is well-established. As demand for these particles grows and their applications expand, methods for their preparation are continually refined. Moreover, the variety of materials used for NP cores is increasing, which expands the range of characterization techniques available, including those utilizing ultraviolet and infrared spectra, to ensure consistency in Cm-NP preparation.

## 4. Polymer-Coated Nanoparticles for Theranostic Applications

The nanoparticles to be used in biomedical fields should provide certain attributes depending on the specific application. For those particles to be used as MRI contrast agents, in magnetic hyperthermia or magnetic-based bioassays and sample enrich-

ment processes, the nanoparticles should be able to respond to externally applied magnetic fields efficiently. In this regard, superparamagnetic nanoparticles able to provide high magnetic moments upon application of magnetic fields are preferred because these particles completely demagnetize when the field is removed. That provides additional advantages over other magnetic materials, including stability and lack of aggregation when the field is removed. On the contrary, for applications where the nanoparticles are going to be used to deliver drugs to tumors or other unhealthy tissues, the controlled release at the target site is key. In this regard, nanomaterials with enhanced targeting efficiency and prolonged circulation times so that the particles can be internalized by the cells of interest are pursued. Finally, for photothermal therapy applications, materials with increased energy absorption and a plasmon resonance wavelength in the NIR range are ideal. In general, for all the bioapplications discussed in this work, the nanoparticles should have no toxicity and excellent biocompatibility. In the following, the main applications of polymer-coated nanoparticles within the theranostic fields are presented and the main attributes of the particles for each application are thoroughly discussed to give an overview of the state of the art.

### 4.1. Polymer-Coated MNPs for Magnetic Resonance Imaging (MRI)

MRI is a bioimaging technique that is very effective in producing high-quality images of the human body's internal organs. Numerous diseases including organ inflammation or infection, degenerative diseases, strokes, cancers, and other abnormalities in human tissue or organs, can be treated with the help of MRI.[363] The phenomenon of nuclear magnetic resonance (NMR) which is frequently employed by chemists to determine molecular structure, is the direct source of MRI. There is no relation between NMR and radiation, so the term "nuclear" was eliminated when the focus shifted to imaging to spare patients from the concern of being irradiated.[364]

The basis of MRI is the interaction of a nucleus with a nuclear magnetic moment, or "spin", and an applied magnetic field. The nuclei with nuclear magnetic moments that are best suited for magnetic resonance detection are $^{1}H$, $^{31}P$, $^{13}C$, $^{15}N$, and $^{19}F$. The most prevalent and most MRI-sensitive nuclei in the living system are protons ($^{1}H$). Since the proton, also known as the hydrogen atom, is the most common atom in the body and has a magnetic field, almost all clinical MRI imaging is currently done with the help of it.[365,366] When protons are present in biological tissues, their inherent spin feature allows for a phenomenon that is similar to a tiny magnet. Therefore, in the presence of an external magnetic field $B_0$, a significant portion of the proton spins align themselves parallel to the field, but a lesser portion aligns themselves antiparallel. The system's net nuclear magnetization is established because of this separation in spin alignment. As a result, the net magnetization vector ($M_z$) that is generated because of these aligned spins cumulatively aligns parallel to the direction of the external magnetic field ($B_0$). This alignment represents a state of balance in the system, in which most proton spins align with the dominant magnetic field and help produce a measurable magnetization vector along the same axis. This phenomenon essentially clarifies the complex interaction between the intrinsic magnetic characteristics of protons and the external magnetic field, resulting in a net nuclear magnetization that highlights the fundamental ideas behind MRI and its use in accurately and faithfully probing the internal structures and dynamics of biological entities (see **Figure 20**).

The spins precess about the axis of $B_0$, which is generally interpreted as the z-axis, at a frequency proportionate to the strength of the external magnetic field when tilted away from the magnetic field. The Larmor frequency ($W_0$) is defined as follows:

$$W_0 = \gamma B_0 \tag{6}$$

where $\gamma$ is the gyromagnetic ratio, a constant with a characteristic value of 42.58 MHz $T^{-1}$ for protons, and $W_0$ is the Larmor frequency in MHz. The strength (T) of the external magnetic field is represented by $B_0$. The net magnetization keeps precessing until it reaches its thermal equilibrium state after the RF pulse is off.[365]

Two types of relaxations take place during this period: T1 (transverse or spin/spin) and T2 (longitudinal or spin-lattice). T1 and T2 are particularly useful for identifying the signal in MRI because of their sensitivity to the type and quantity of tissue. This tissue-dependency characteristic accounts for the superior soft-tissue contrast of MRI.[367] Although MRI can detect and identify tumors more clearly and quickly, clinicians may find it difficult to distinguish between normal and malignant tissues due to the intrinsic low sensitivity of this test.[368] Therefore, contrast agents, like MNPs, can be utilized to improve the clarity and precision of images, helping physicians to identify abnormalities in tissues or organs more accurately.[4] Contrast agents alter the water protons' relaxation times, which alters the signal's magnitude in the bodily regions where they are incorporated, improving the quality of MRI pictures of tissues and organs. The rates of all the relaxation processes are often shortened by an MRI contrast agent; however, each substance primarily affects one of them. T1, or positive, contrast agents mostly shorten the longitudinal component of the magnetization's relaxation time, whereas T2, or negative, contrast agents primarily shorten the transverse component's relaxation time.[369]

#### *4.1.1. T1 Contrast Agents*

Positive contrast agents, also referred to as T1 agents, generally enhance the longitudinal (or spin-lattice) relaxation rates of water protons in tissue more than the transverse (or spin-spin) relaxation rates (1/T1). Depending on the biological system, the T1 relaxation time is not constant. T1 contrast agents, which distinguish between fat and water by giving fat a brighter contrast and water a darker contrast, can be used to create positive imaging.[368] The majority of T1 contrast agents contain paramagnetic metal ions, which need to have the ability to reduce T1. With its high paramagnetic moment (7 unpaired electrons), the lanthanide $Gd^{3+}$ is the most widely used ion that meets this requirement. Due to their strong magnetic moments, the transition metal ions $Mn^{2+}$ and $Fe^{3+}$ are also effective T1 contrast agents but the free metal ions must be coordinated with a protective chelate because the majority of free metal ions are harmful to living tissue.[370]

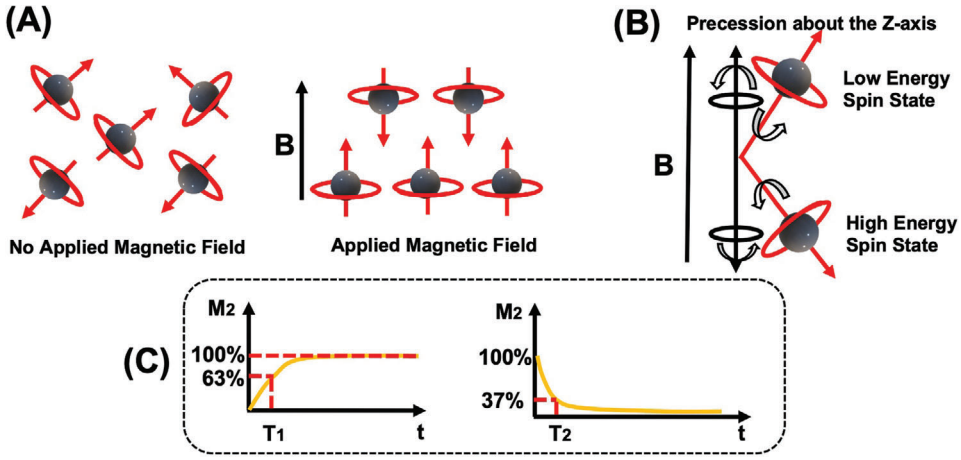


**Figure 20.** Illustration of the following: a) proton alignment in a magnetic field; b) precession along the z-axis. c) graphical representation of T1 relaxation and T2 relaxation.

#### *4.1.2. T2 Contrast Agent*

Transverse magnetization resulting from interactions between nearby hydrogen nuclei's magnetic fields is lost because of T2 relaxation. It is a loss of phase coherence inside the spin system rather than an energy loss mechanism like T1. Spin-spin relaxation, another name for this process, results in the dephasing of the tissue's magnetic moments and the breakdown of transverse magnetization.[367]

The most used MRI technique for distinguishing fat from water is T2-weighted imaging, which shows fat as having a darker contrast and water as having a brighter contrast. T2 contrast agents enable darker images of the regions of interest as well as negative contrast augmentation.[363]

For example, Ali et al. investigated the efficacy of multifunctional polymer-based SPIONs, commonly referred to as bio-ferrofluids, serving as a T2 magnetic resonance contrast agent.[371] Their study also delved into the uptake mechanisms and potential toxicity of these nanoparticles in liver tissues. The synthesis of bio-ferrofluids followed a co-precipitation approach via a polymeric pathway. Initially, maghemite/poly(4-vinyl pyridine) (P4VP) nanocomposites were synthesized, and subsequently, they underwent coating with a hydrophilic polymer, PEG acrylate (PEGA). **Figure 21**A,B displays the findings of the TEM ($13.08 \pm 2.33$ nm) and DLS (163 nm) and the characterization of bio-ferrofluids. The T2 and T1 relaxation times were measured for both Endorem (one of the most widely marketed SPION agent products) and bio-ferrofluids. For Endorem, the r2 value stood at $113.99 \pm 11.08$ mM $s^{-1}$, while the corresponding r1 value was $2.11 \pm 0.21$ mM $s^{-1}$. In contrast, for bio-ferrofluids, the r2 value was recorded at $82.8 \pm 8.28$ mM $s^{-1}$, with an r1 value of $0.45 \pm 0.05$ mM $s^{-1}$. These findings suggest that bio-ferrofluids exhibit transverse relaxivity either lower than or, at most, comparable to Endorem (see Figure 21C).

To assess the efficacy of bio-ferrofluid as a contrast agent (CA) relative to Endorem under steady-state conditions, T2*-weighted images of the brain were acquired pre- and post-injection of both agents at a dose of 23.5 mg Fe $kg^{-1}$ body weight. Initially, the brain vasculature exhibited clarity in the pre-injection images (Figure 21D: d1,d5). After the injection of bio-ferrofluids and Endorem, there was a significant drop in signal intensity (SI) (Figure 21D: d1,d6). This drop was accompanied by a hypointense (darkening) of the cerebral vasculature, which is a sign that the CAs were in circulation. After 2 h of injection, the mouse given Endorem showed hypointense brain vasculature (Figure 21D: d3), whereas the brain vasculature (Figure 21D: d7) cleared bio-ferrofluids from circulation. Furthermore, an in vivo study's findings showed that bio-ferrofluid does not have any harmful effects on liver tissue and stays in the liver longer than Endorem—up to 30 days after injection.

#### *4.1.3. Dual (T1/T2) Contrast Agent*

Single-mode T1 or T2 MRI images often present limitations, particularly in accurately identifying tumors. For instance, T1-weighted images may exhibit signal strength loss owing to the presence of fat, while T2-weighted images can lead to potential confusion between tumors and signals from bleeding or calcification. Magnetic resonance artifacts, characterized by bright or dark signals, frequently stem from endogenous factors prevalent within disease lesions, complicating precise diagnostic interpretation.[372,373] Consequently, by leveraging the complementary advantages of both imaging modes, these contrast agents offer the potential to overcome the shortcomings associated with single-mode imaging, thereby improving diagnostic accuracy, and are mostly used in clinical settings when some of the in vivo artifacts are present.[372,374,375]

### 4.2. Polymer-Coated MNPs for Magnetic Hyperthermia Therapy

One of the acknowledged therapeutic techniques for cancer, in addition to surgery, radiation therapy, chemotherapy, gene therapy, and immunotherapy, is hyperthermia, commonly referred to as thermal therapy or thermotherapy. Using external heat sources entails elevating the body's temperature or the temperature of a particular location above the organism's normal threshold.[376]

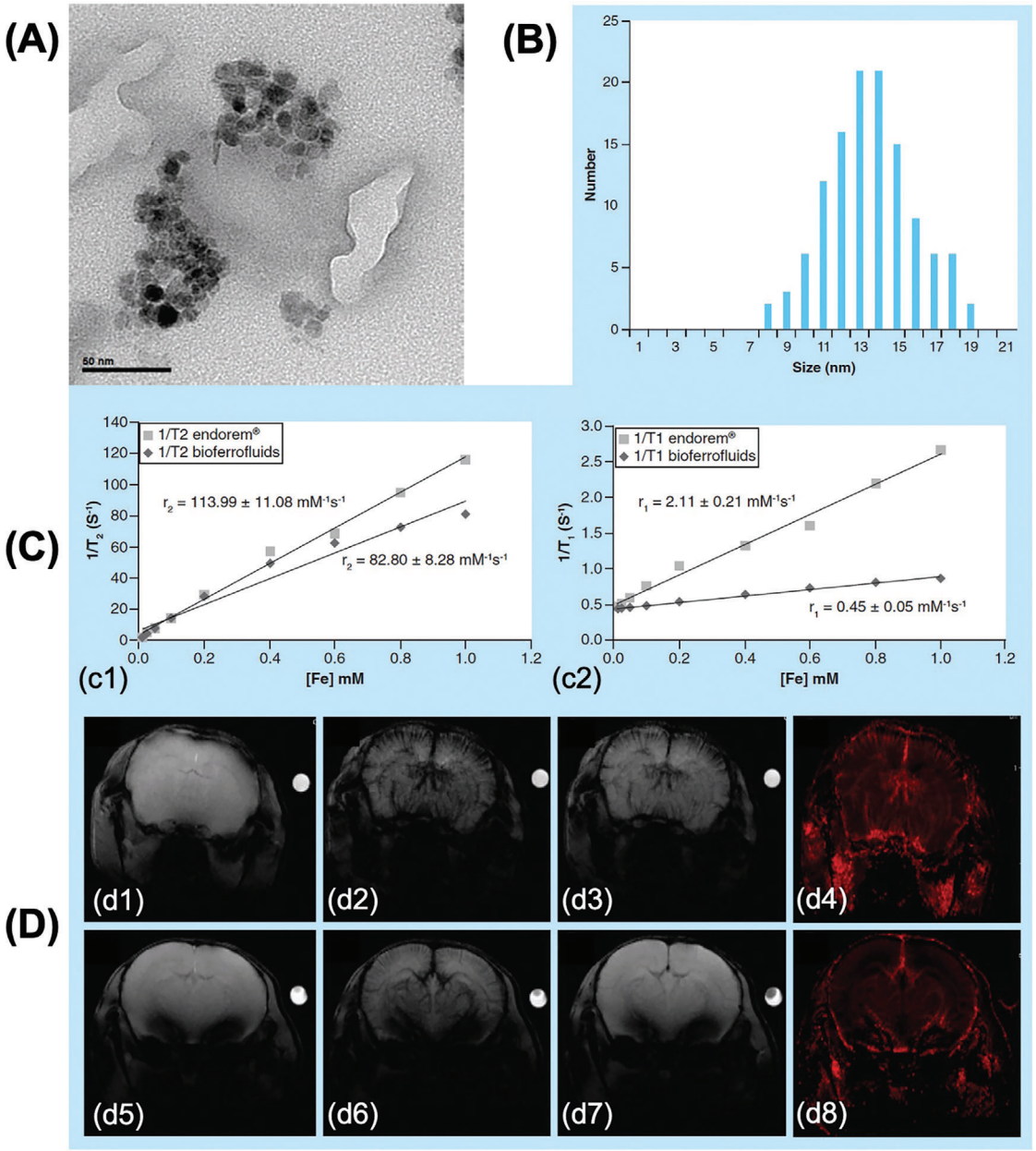


**Figure 21.** A) Transmission electron microscopy images of maghemite MNPs in the bio-ferrofluid. B) DLS size distribution of hydrodynamic size in the bio-ferrofluids sample. C) Comparative study of bio-ferrofluids and Endorem's transverse relaxation rates (c1) and longitudinal relaxation rates (c2). D) T2*-weighted pictures of the cerebral vasculature in a mouse before (d1 and d5), 5 min (d2, d6), and 2 h (d3, d7) following injections of bio-ferrofluids (bottom panel) and Endorem (upper panel). The rCBV maps for bio-ferrofluids and Endorem are displayed in (d4) and (d8), respectively. Reproduced with permission,[371] under a Creative Commons license CC BY 4.0.

Elevated tissue temperatures, usually between 40 and 45 °C, are used in hyperthermia to alter the microenvironment of the tumor and normal tissue. In cancer treatment, the goal of hyperthermia is to minimize damage to healthy tissue while fostering an environment that is favorable for the removal of tumors.[377]

Depending on the extent of the cancerous region being treated, hyperthermia can be classified into three basic categories: whole-body, regional, and local. Heat is administered to the entire body using a variety of techniques in the whole-body hyperthermia method, including hot water blankets, electric blankets, and hot wax. Using external applicator arrays and regional perfusion, heat is administered to an organ or area of the body in the regional hyperthermia method. When a superficial cancer is present, applicators that are inserted inside the targeted region or put at the surface or beneath its skin produce electromagnetic waves such as radio waves, microwaves, and ultrasonic waves, which are then used to provide heat to small tumor patches. This process is known as local hyperthermia.[378] Nevertheless, despite these approaches, efficiently managing the heat's spatial distribution within tissue continues to be a formidable obstacle.[379]

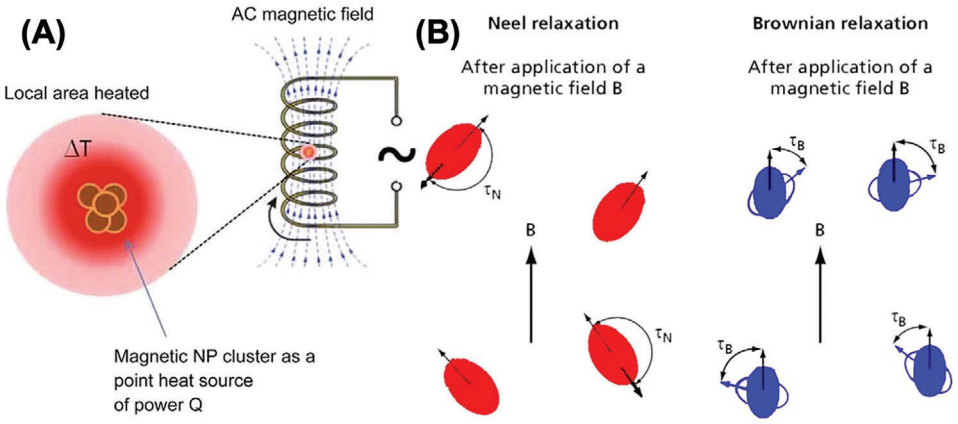


**Figure 22.** Schematic diagram of A) magnetic hyperthermia-based treatment along with the process of B) magnetic (Néel and Brownian) relaxations. A) Reproduced with permission.[384] Copyright 2018, Springer International Publishing AG. B) Reproduced with permission.[385] Copyright 2019, Springer-Verlag GmbH Germany, part of Springer Nature.

Indeed, to address the challenge of controlling the spatial distribution of heat within tissue, magnetic hyperthermia has emerged as a widely utilized approach. Magnetic hyperthermia is a therapeutic technique that utilizes MNPs, typically composed of materials like iron oxide, to generate heat when exposed to an alternating magnetic field generated by radio frequency (RF) induction coils, as shown in **Figure 22**A. This localized heating effect can be harnessed to selectively target and destroy cancer cells while minimizing damage to surrounding healthy tissue.

When MNPs are subjected to alternating magnetic fields, four distinct mechanisms—hysteresis, eddy current, Néel or Brownian relaxation, and frictional losses—can all work to produce heat inside the therapeutic system.[378,380] Superparamagnetic nanoparticles, however, exhibit strong Néel or Brownian relaxation. The influence of each factor varies significantly, contingent upon nanoparticle size, shape, crystalline anisotropy, and the extent of nanoparticle aggregation or agglomeration.[380–382] Heat is produced as a result of domain walls shifting due to the oscillation of the magnetic moment. After the magnetic field is removed, the magnetic moments relax either because of the Néel relaxation occurring within each particle or because of the Brownian relaxation occurring as each particle rotates about its axis.[383] Heat is produced in nanoparticles by the rotation of each particle's magnetic moment in opposition to an energy barrier. It's known as Brownian relaxation when the particle rotates because of the surrounding fluid's shear stress, which transfers thermal energy. On the other hand, Néel relaxation—which releases thermal energy through atomic dipole rearrangement inside the crystal—occurs when the particle stays stationary while its moment rotates (see Figure 22B).

Both systems can function simultaneously, and how they contribute will depend on the timelines at which they take place.[381,386,387] The Néel and Brownian relaxation times, $\tau_N$ and $\tau_B$, respectively, are typically represented by:

$$\tau_B = 3\eta V_H / k_B T \tag{7}$$

$$\tau_N = \tau_0 \, e^{(KV_M/k_B T)} \tag{8}$$

where attempt time, anisotropy constant, MNPs primary volume, Boltzmann constant, temperature, solvent viscosity, the hydrodynamic volume of MNPs, and temperature are represented by the variables $\tau_0$, K, $V_M$, $k_B$, T, $\eta$, and $V_H$, respectively. According to Rosensweig, the Néel and Brownian relaxations happen simultaneously, and the effective relaxation angular frequency is:

$$\omega_{eff} = 1/\tau_{eff} = 1/\tau_N + 1/\tau_B \tag{9}$$

This is the inverse of effective relaxation time.

It can be said that relaxation with the shortest characteristic time drives the heating. At specific frequencies and amplitudes of the alternating magnetic field, the SLP, or specific absorption rate (SAR), stands for normalized characteristics that enable us to evaluate and quantify the efficiency of a given material to convert electromagnetic energy into heat. As per the well-known Rosensweig equation, the heat loss of a magnetic hyperthermia test conducted on a ferrofluid will depend on two factors: a) the frequency and strength of the magnetic field, and b) the physical properties of the ferrofluid, including the solvent viscosity, particle size distribution, magnetic anisotropy energy constant of the magnetic core, and the magnetic and hydrodynamic radius of the MNPs. In an experimental setting, the SAR (W $g^{-1}$) is computed using the formula below:

$$SAR = C\Delta T / m\Delta t \tag{10}$$

where C represents the specific heat capacity of the medium, which is assumed to be equivalent to that of water (4185 J $L^{-1}$ $K^{-1}$). The concentration of the transition metal of interest (g $L^{-1}$) in the magnetic material solution is denoted by m. The slope of the initial linear section of the temperature versus time curve, represented by $\Delta T/\Delta t$, indicates the rate of change of temperature over time.

Liu et al. reported the synthesis of ferrimagnetic vortex-domain structure (FVIOs) by thermal phase transformation of alpha-$Fe_2O_3$ nanorings (NRs).[388] As can be seen in **Figure 23**A,B, these FVIOs show an average outer diameter of 70 nm, heights of 50 nm, and an inner-to-outer diameter ratio of ≈0.6. The cell vi-

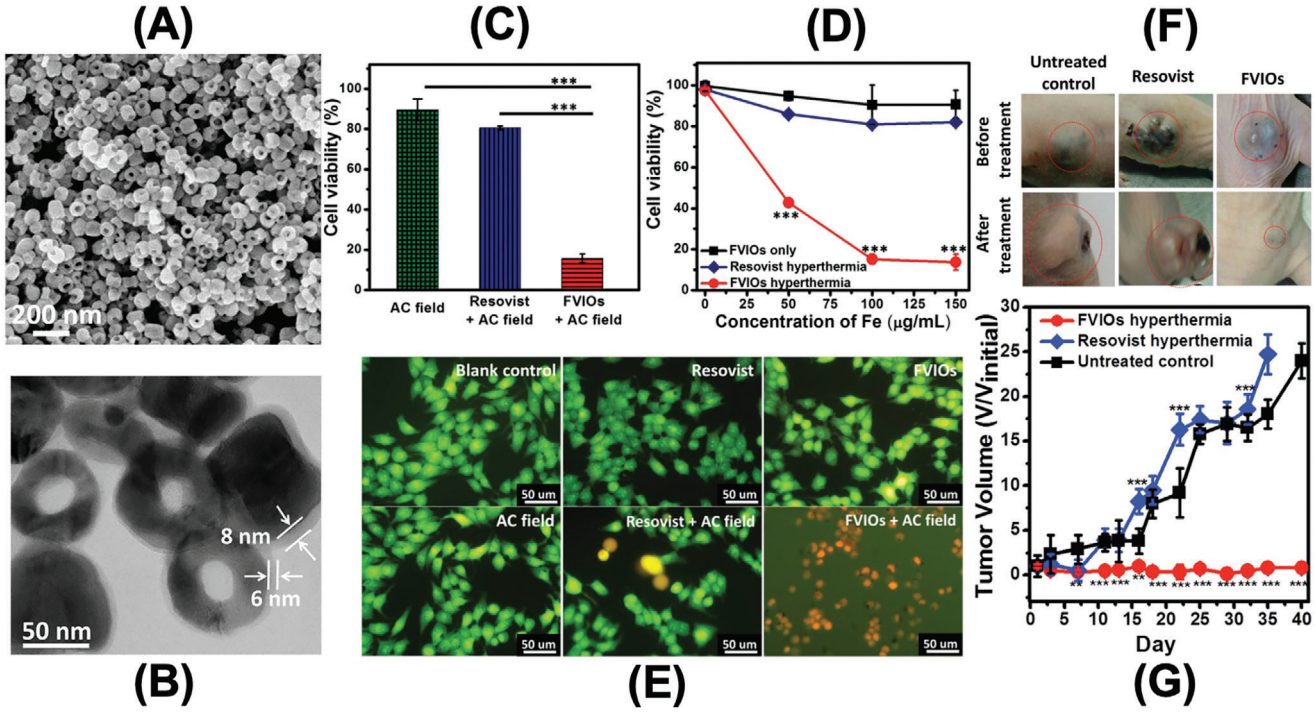


**Figure 23.** A) SEM image of FVIOs. B) TEM image of FVIOs dyed with ruthenium tetroxide ($RuO_4$) to obtain a sufficient contrast for surface coating mPEG layer. C) Cell viability of MCF-7 cancer cells subjected to magnetic hyperthermia with FVIOs and Resovist. D) Dosage dependence of cell viability for MCF-7 cells treated with magnetic hyperthermia using FVIOs and Resovist. E) Immunofluorescence images of MCF-7 cells after treatment with Resovist, FVIOs, AC field, Resovist + AC field, and FVIOs + AC field. The untreated group is the blank control. F) Nude mice xenografted with breast cancer cells (MCF-7) before treatment (upper row, dotted circle) and 40 days after treatment (lower row) with the untreated control, Resovist hyperthermia, and FVIOs hyperthermia, respectively. G) Plot of tumor volume (v/v initial) versus days after treatment with FVIOs hyperthermia, Resovist hyperthermia, and untreated control. Reproduced with permission.[388] Copyright 2015, WILEY-VCH.

ability of MCF-7 breast cancer cells treated with magnetic hyperthermia after being incubated with FVIOs or Resovist is depicted in Figure 23C–E. After being treated with heat for 10 min (Figure 23F,G), FVIOs showed a notable cytotoxic effect with a significant loss in cell viability to only 16%. FVIOs' good biocompatibility makes them attractive as bio-magnetic materials for the development of diverse heat-inducing nanoagent systems, which could eventually provide a secure and efficient therapeutic option for a variety of malignancies.

### 4.3. Polymer-Coated MNPs for Sample Enrichment and Bioassays

Novel techniques involving polymer-coated MNPs have been devised for the isolation of diverse cell populations, including rare ones such as circulating tumor cells (CTCs).[389] These cells, originating from primary tumors and circulating in the peripheral bloodstream, are crucial targets for cancer detection and their isolation from blood is challenging due to their low number.[390] Their analysis offers valuable insights into their biological properties and provides essential data regarding the primary tumor cells. Various particle-based approaches have been suggested for enriching CTCs, with positive enrichment through immunomagnetic separation emerging as one of the most widely utilized methods.[391] This technique boasts significant advantages, including easy manipulation, high capture efficiency, and specificity.

Polymer-coated MNPs exploit the advantageous combination of magnetic separation and target-specific binding to effectively enrich CTCs. The polymer coating plays a pivotal role by stabilizing the magnetic core, furnishing a biocompatible surface for functionalization, and influencing target specificity. The operational mechanism of polymer-coated MNPs in CTC enrichment entails their functionalization with ligands capable of binding to CTC-specific markers, such as antibodies,[392] aptamers,[393] or other targeting biomolecules, chosen according to the expression profile of CTC surface antigens.[394] Upon introduction into a blood sample, these functionalized MNPs selectively adhere to CTCs through receptor-ligand interactions. Subsequent application of an external magnetic field facilitates the swift and efficient separation of CTC-bound MNPs from the majority of blood cells.[395] This magnetic manipulation enables the isolation and enrichment of CTCs with minimal contamination from normal blood cells, thereby enhancing sensitivity and specificity in downstream analyses.

A variety of synthetic and natural polymers are utilized as coatings, each presenting distinct advantages and considerations. Synthetic polymer coatings, such as PEG,[396] PDA,[397] and polyvinylpyrrolidone,[398] offer remarkable stability and biocompatibility. They effectively reduce nonspecific interactions and immunogenicity, while their properties can be customized

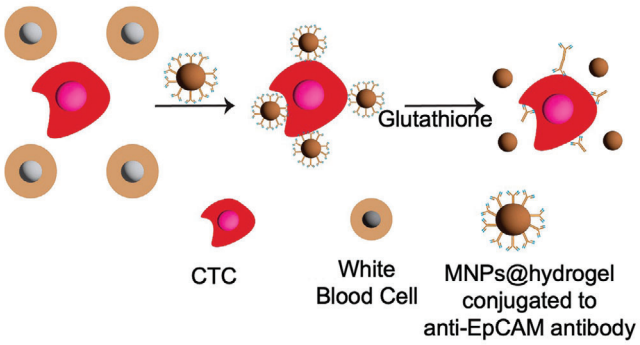


**Figure 24.** Diagram depicting the utilization of MNPs enveloped in a hydrogel linked with anti-EpCAM for isolating and retrieving CTCs following the implementation of a magnetic framework. Reproduced with permission,[403] under a Creative Commons license CC BY 4.0.

to enhance the surface characteristics of MNPs for specific biomedical applications. On the other hand, natural polymers like chitosan,[399] alginate,[400] and dextran[401] provide both biocompatibility and functional groups suitable for bioconjugation with targeting ligands. These polymers create a biomimetic environment conducive to CTC capture, thus minimizing adverse effects on cell viability and functionality. The selection of a polymer coating depends on numerous factors, including desired surface chemistry, compatibility with targeting ligands, and application-specific needs. It is imperative to optimize polymer-coated MNPs to achieve robust and efficient CTC enrichment, thereby expanding their potential applications in cancer research and clinical diagnostics.

For instance, Wang et al. explored the utilization of polymer-coated MNPs for capturing and isolating CTCs (**Figure 24**).[402] They designed MNPs with a hydrogel coating aimed at preventing nonspecific cell adhesion. Functionalization of the hydrogel layer involved covalently linking an anti-epithelial cell adhesion molecule (anti-EpCAM) antibody to the carboxyl group of methacrylic acid (MAA). This antibody is specifically bound to their model CTCs, characterized by high expression of EpCAM (MCF-7 cells), thereby exhibiting significant potential for separating CTCs from test samples using a magnetic scaffold. To facilitate the separation process, a glutathione (GSH) solution was employed to disrupt the disulfide bonds in the hydrogel matrix, effectively dissociating the MNPs from the CTCs and ensuring over 95% CTC viability post-separation.[403]

Besides CTC isolation for cancer applications, polymer-coated MNPs have other applications as enrichment agents. For instance, there is a growing demand for developing bioassays with higher sensitivity, which is currently a major limitation of current systems. One emerging platform for bioassays is magnetic nanoparticle spectroscopy (MPS). First reported in 2006, MPS is a technology stemming from magnetic particle imaging, a noninvasive tomographic technique.[404,405] Under the influence of an oscillating magnetic field (magnetic drive field), MNPs are periodically saturated.[13,249,406,407] The two different modalities for the magnetic drive field include the mono-frequency drive field and dual-frequency drive; the mono- or dual- refers to the number of magnetic drive fields generated.[249,407–412] MPS measures the dynamic magnetization of periodically saturated MNPs that encompasses the drive field frequency and a series of harmonic frequencies. Since there are negligible harmonic signals from the non-magnetic or paramagnetic biological samples, the harmonic signals are only associated with the MNPs present in the sample. There is a modification in the dynamic magnetic response when the target analytes are captured by the MNPs, and the amplitudes of the higher harmonic frequencies can be utilized to quantify the concentration of target analytes in a biological sample. The entities to be measured are the MNPs linked to the molecule/cells. Once these are detected/measured, the molecule/cells can be quantified accordingly.

Polymer-coated MNPs are one of the preferred tracers for MPS, as they are biocompatible, biodegradable, chemically stable, and superparamagnetic.[407] In a study conducted by Horvat et al., MNPs were coated with a cross-linked polymer, a poloxamer modified with acrylate groups conjugated to the thiol functionalized poly(glycidol)s; the cross-linked polymer-coated MNPs improved the signal intensity in MPS.[413] Since the purpose of MPS-based assays is to measure the change in magnetization based on the binding between the MNPs and biological analytes, polymers, such as polysorbate 20 or Tween 20, can act as surfactants to prevent nonspecific binding by disrupting non-specific hydrophobic interactions. Overall, the polymer coating directly impacts the behavior, stability, and functionality of the MNPs in MPS.

Ever since the inception of MPS, rapid and highly sensitive MPS-based bioassays have been developed to capture specific biochemical analytes. Two different types of bioassay platforms have been reported, including surface- and volumetric-based assays (**Figure 25**A,C). For the surface-based assays, functionalized MNPs are bound to a target analyte captured on a chemically modified reaction surface (substrate) through a specific antigen-antibody sandwich assay structure.[249,414] The dynamic magnetic responses correspond to the Néel relaxation time, which corresponds to the bound, stationary MNPs' internal rotation of the magnetic moment within the particle core, as shown in Figure 25B.[415] The concentration of the bound MNPs has a direct proportion to the concentration of the target analytes in the solution and the amplitude of the harmonic signals.[249] It has been reported that surface-based MPS assays have been utilized to detect various biological analytes including viruses, drugs, and toxins. However, surface-based assays rely on the spatial separation of the surface receptors on the target analytes and multiple washing steps to remove the unbound analytes and MNPs, making them unsuitable for field applications.

In a volumetric-based assay, functionalized MNPs capture the biomolecule to be measured via specific recognition of surface receptors on the target analyte, such as antigen-antibody binding.[410,416–418] MPS detects the changes in the magnetization of freely rotating MNPs in solution before and after binding to the target analyte. The dynamic magnetization is dominated by the Brownian relaxation process, which corresponds to the physical rotation required to align the MNP's magnetic moment with the direction of the applied magnetic field.[415] One major parameter affecting the Brownian relaxation time is the hydrodynamic size affected by the polymer coating's thickness, as this influences the particle-particle interactions.[13] Once the target analytes are captured by the MNPs, clustering of the MNPs occurs, which increases the hydrodynamic diameter of the MNPs

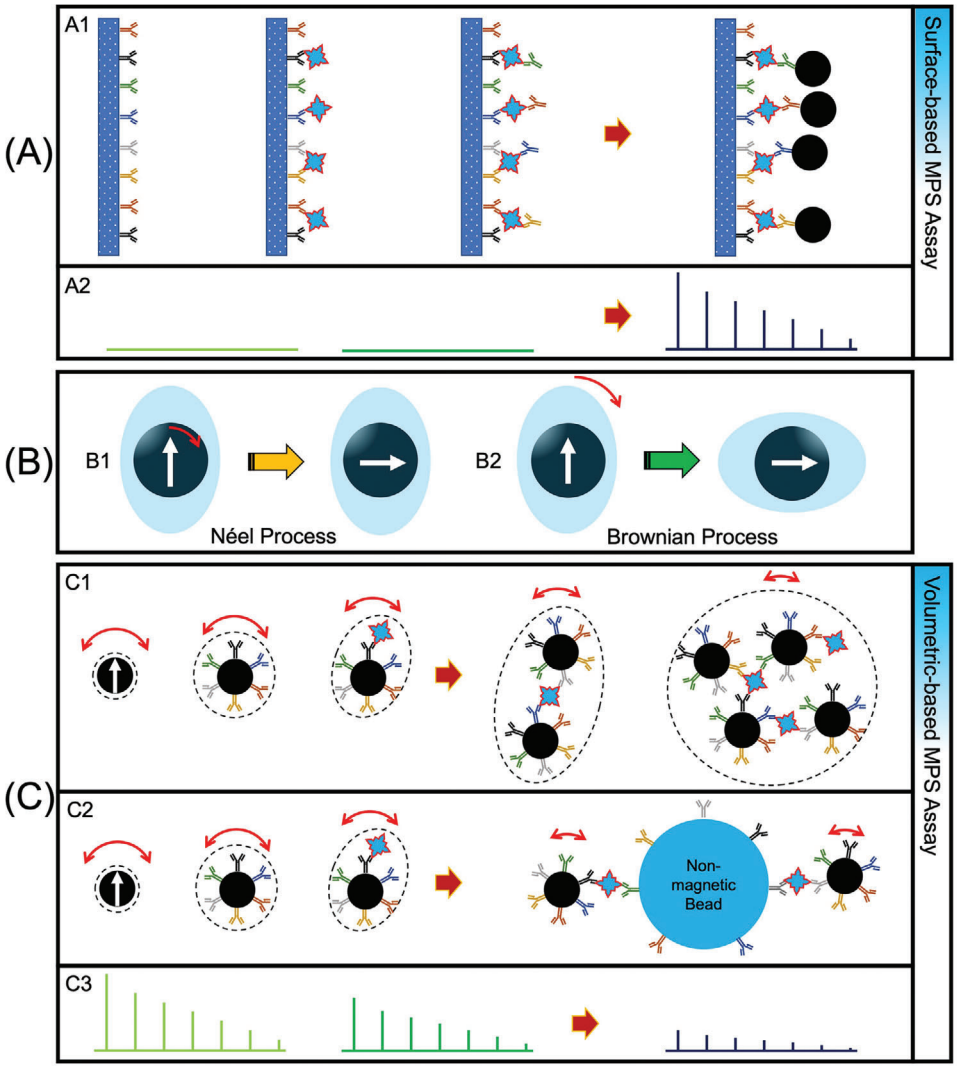


**Figure 25.** Illustration of the mechanisms of volumetric- and surface-based MPS bioassays. Panels (A) and (C) are schematic views of surface- and volumetric-based MPS assay methods, respectively. B) Schematics of dynamic magnetic relaxations. Reproduced with permission.[249] Copyright 2022, IOP Publishing Ltd.

and subsequently a significant change in the Brownian relaxation time and the dynamic magnetization of the MNPs in the magnetic drive field.[406,410] In the MPS spectra, there is a larger phase lag and lower harmonic amplitudes can be observed in the MPS spectrum, indicating weaker dynamic magnetic responses of the MNPs, which can be used to quantitively measure the concentration of the captured analytes and the reaction kinetics.[418] This phenomenon can be exploited for the detection of target analytes at ultra-low concentrations in a rapid, sensitive, wash-free volumetric-based assay.

Zhong et al., developed a volumetric-based MPS assay to detect SARS-CoV-2-spike protein-coated polystyrene beads (mimic viral particles) captured by 80 nm MNPs coated with protein A conjugated to the spike protein antibodies with a limit of detection of 0.084 nM.[418] In the absence of the mimic SARS-CoV-2 particles, the amplitudes of the produced harmonic signals were strong, as the MNPs were freely moving in solution. In the presence of the SARS-CoV-2 particles, there was a significant decrease in the amplitudes of the harmonic signals. Other than the SARS-CoV-2 virus, volumetric-based MPS assays have been reported to detect the H1N1 virus, hormones, cytokines, thrombin, and DNA aptamers.[249]

### 4.4. Polymer-Coated AuNPs for Photothermal Therapy

Over the past twenty years, innovative methodologies leveraging nanotechnologies have revolutionized cancer treatment, encompassing drug delivery,[419] phototherapy,[420,421] and immunotherapy.[422] Among these, photothermal therapy stands out as a straightforward, highly efficient, and low-toxicity method for combating cancer. It hinges on the use of photothermal agents to harness light energy and convert it into heat, thereby inducing the death of cancerous cells. In contrast to alternative

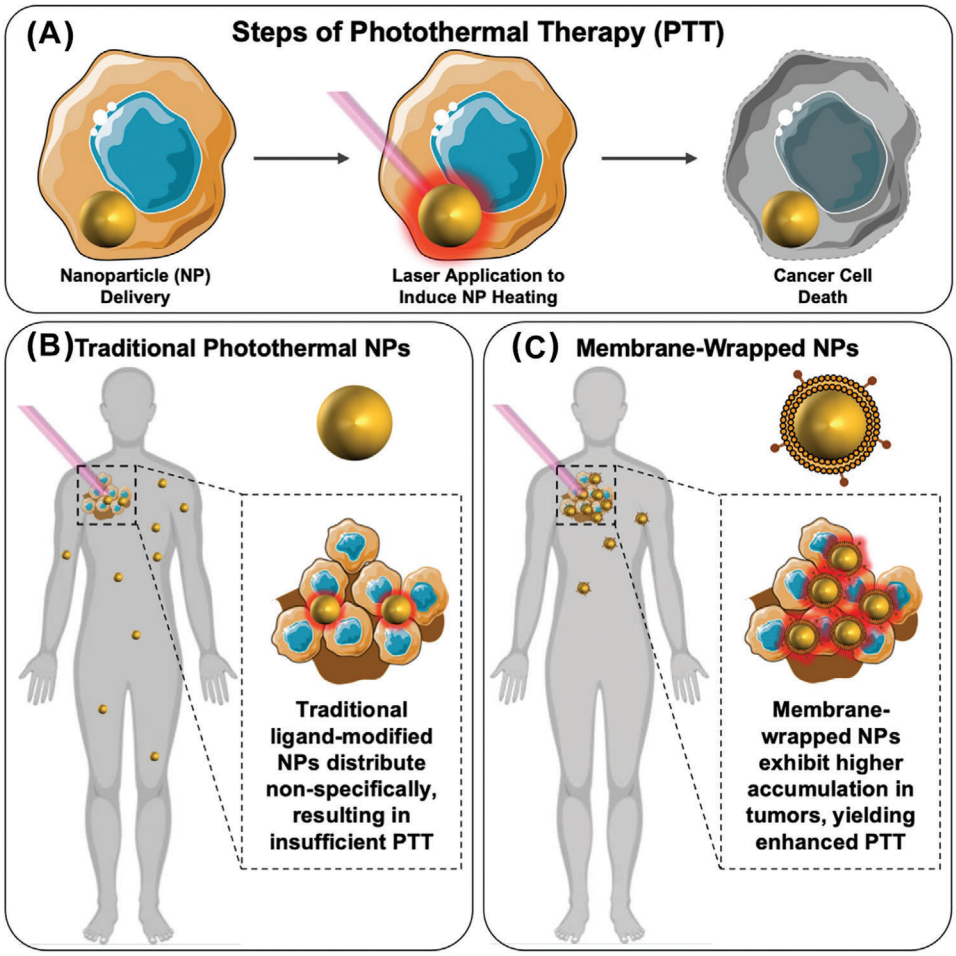


**Figure 26.** A) Illustration showing the employment of photothermal therapy involves the delivery of NPs into tumors, followed by laser irradiation to induce NP heating leading to cancer cell death. B) Traditional PEG- or ligand-modified NPs distribute non-specifically throughout the body, and low tumor accumulation may lead to insufficient PTT effects. C) Coating photoresponsive NPs with cell-derived membranes enhances their tumor accumulation, increasing the efficacy of PTT upon light irradiation. Reproduced with permission,[427] under a Creative Commons license CC BY 4.0.

techniques, light stands out as an optimal external trigger due to its simple regulation, precision, and remote manipulability. This ease of adjustment and command facilitates more precise treatments, resulting in reduced harm to surrounding healthy tissues.[423] Nevertheless, when it comes to photodynamic therapy using either laser or visible light, its effectiveness is constrained by the limited depth of light penetration.[424] However, NIR light, falling within the wavelength range of 800 nm – 1200 nm, boasts significantly enhanced body transparency, making it the preferred choice for photothermal therapy which primarily operates by elevating the temperature within tumors.[425]

While AuNPs have been widely utilized in photothermal therapy, specific characteristics are imperative for them to be considered ideal candidates. Firstly, AuNPs must exhibit excellent dispersibility in aqueous solutions, coupled with an appropriate size and uniform shape. Additionally, these nanoparticles should ideally have a plasmon resonance wavelength within the NIR range of 650 nm – 950 nm to minimize harm to adjacent healthy tissues,[426] while ensuring adequate photothermal efficiency. Furthermore, they should demonstrate minimal to no cytotoxicity when introduced into living systems. Finally, AuNPs have simple chemical modification procedures that allow their shape and size to be tuned with ease, which allows the tuning of the plasmon absorption peak and results in enhanced photothermal conversion efficiency. Presently, polymer-coated AuNPs stand out as the preferred agents for enabling photothermal therapy, such as polyaniline and PDA-coated AuNPs. This preference stems from their superior biodegradability and biocompatibility, combined with significant photothermal efficiency. **Figure 26** demonstrates the utilization of polymer-coated AuNPs in this process and the subsequent release of drugs upon irradiation.[427] During this procedure, AuNPs are administered to target the tumor site, where they accumulate. Following this, an external laser, calibrated to coincide with the peak plasmon resonance/absorbance wavelength of the AuNPs, is directed at the tumor area (Figure 26A,B). The laser irradiation prompts the nanoparticles to produce heat, causing irreversible harm to cancer cells in the vicinity of the tumor tissue. Polymer-coated AuNPs exhibit superior tumor delivery and therapeutic outcomes compared to traditional ligand-modified AuNPs (see Figure 26C).

Polyaniline stands as a venerable choice among conducting polymers for photothermal therapy applications, renowned for its affordability, impressive conductivity, and remarkable mechanical flexibility. Polyaniline-coated nanoparticles were initially suggested for photothermal therapy by Huh et al. in 2011, who synthesized these particles through a chemical oxidation polymerization process, resulting in the formation of emeraldine salt.[428] Later, their thermogenic properties were meticulously evaluated through in vitro experiments.

In contrast, PDA a naturally occurring polymer, exhibits well-defined biodegradation properties without inducing adverse effects.[429] Initially investigated by Liu et al., PDA-coated entities emerged as a promising candidate for photothermal therapy.[430] These authors devised dopamine-melanin colloidal nanospheres via the oxidation and self-polymerization of dopamine within a blend of water, ethanol, and ammonia under ambient conditions. Melanin, a naturally existing biopolymer, serves various roles in living organisms, such as thermoregulation and shielding from ultraviolet harm.[431]

PDA has been utilized in several cases to boost compatibility with living tissues and add hyperthermic capabilities to inorganic materials, resulting in a multifunctional approach. For instance, iron oxide nanoparticles have been coated with PDA in a couple of works, yielding multifunctional particles capable of being targeted by a magnetic field, thus enhancing photothermal therapy for cancer.[432] Similarly, in other research studies, Au NRs, which are considered effective photothermal agents, have been coated with PDA to further amplify their photothermal efficiency.[433] Consequently, surface modification using PDA is acknowledged as an effective strategy for improving the compatibility of non-biodegradable substances.[434]

### 4.5. Polymer-Coated AuNPs for Drug Delivery

Controlled drug release strategies utilize three key approaches: i) triggered release of cargo via light, triggered release of cargo in the presence of a reductant, and triggered release of cargo due to a change in pH levels in an intracellular environment. AuNPs offer versatility due to their facile surface modification and nanostructure size manipulation capabilities. Surface modification of AuNPs with ligands such as PEG, monoclonal antibodies, proteins, peptides, small biomolecules, or very recently, cell-membrane coatings have proven to be essential in enhancing their overall targeting efficacy to deliver therapeutics. PEG coating and very recently, cell membrane coating[362] have been shown to improve and prolong circulation times of nanocarriers in blood, leading to increased cellular internalization (**Figure 27**A–D), cargo accumulation at tumor sites, and spectroscopic tracking of delivery of therapeutics.[435,436] Other ligands like monoclonal antibodies,[437] proteins,[438] peptides,[439] and small biomolecules[440] have been shown to improve their tumor targeting and uptake performances. For instance, folate-mediated AuNPs loaded with doxorubicin (DOX) show enhanced cellular internalization and better therapeutic performances compared to non-folate counterparts.[441] Additionally, AuNPs can serve as a thermal source for NIR-triggered thermos-responsive release, leveraging the photothermal effect. Nano-engineering allows for the creation of porous and hollow structures in AuNPs, thereby providing ample surface area and large inner cavities for efficient adsorption and loading of various small molecules nanotherapeutics, and macromolecules, enhancing their utility in drug delivery systems.

AuNPs, particularly AuNVs with hollow structures, can be triggered for controlled release under external stimuli like NIR light and/or ultrasound. AuNVs have been demonstrated to seamlessly integrate with liposomes and mesoporous silica for drug loading and controlled release.[442,443] Chemotherapeutic drug DOX tethered onto AuNPs with a PEG spacer[444] effectively enters tumor cells and releases them in acidic environments, overcoming multidrug resistance. AuNPs act as fluorescence probes, monitoring DOX release via fluorescence recovery. AuNRs functionalized with siRNA silence key genes involved in tumor metastasis. Au nanospheres deliver therapeutic oligonucleotides with NIR-triggered controllable release.[445] AuNCs with hollow interiors and porous shells serve as carriers for drug/gene delivery, with specific recognition of cancer cells and accelerated release under NIR illumination.

The varying pH conditions found in solid tumors compared to normal, healthy tissues, coupled with the acidic behavior of lysosomes and endosomes, present a prospective target for the development of pH-sensitive drug release systems. Reductant-triggered release systems exploit glutathione (GSH) as a main reductant in intracellular environments, achieving a controlled drug release through thiol-disulfide exchange reactions.[446] Light-triggered release methods utilize AuNPs' surface plasmon resonance absorption for NIR light, enabling photothermal conversion and controlled drug release.[447] Yavuz et al. demonstrated the NIR light-triggered release of DOX from AuNPs-based delivery systems, utilizing the photothermal effect to expose pores and release the drug.[448] Integration of AuNPs' properties with other therapeutic options enables targeted delivery, controlled release, multimodal imaging, and enhanced therapy efficacy, representing a core strategy for therapy design.

## 5. Challenges and Biosafety Discussions

The use of nanoparticles in biomedical applications presents a complex array of challenges, spanning from synthesis methodologies to functionalization strategies and considerations of biocompatibility. Chemical synthesis methods often face issues related to reproducibility and scalability, while physical approaches may encounter difficulties in controlling particle size distribution and crystallinity. Biological synthesis routes, though promising due to their environmentally friendly nature, often struggle with yield, purity, and the precise tuning of particle properties. In this context, the establishment of standardized protocols for the reproducible synthesis of nanoparticles with consistent physicochemical properties across batches is crucial. Variations in particle characteristics can significantly impact their performance in various biomedical applications, such as imaging, biosensing, hyperthermia, and drug delivery. A standardized framework for synthesis and characterization would not only enable comparisons between different studies but also accelerate the translation of nanoparticles from laboratory research to clinical applications.

One of the major applications of nanoparticles within biomedicine is the development of novel cancer therapies. Among them, drug delivery using nanoparticles to carry ther-

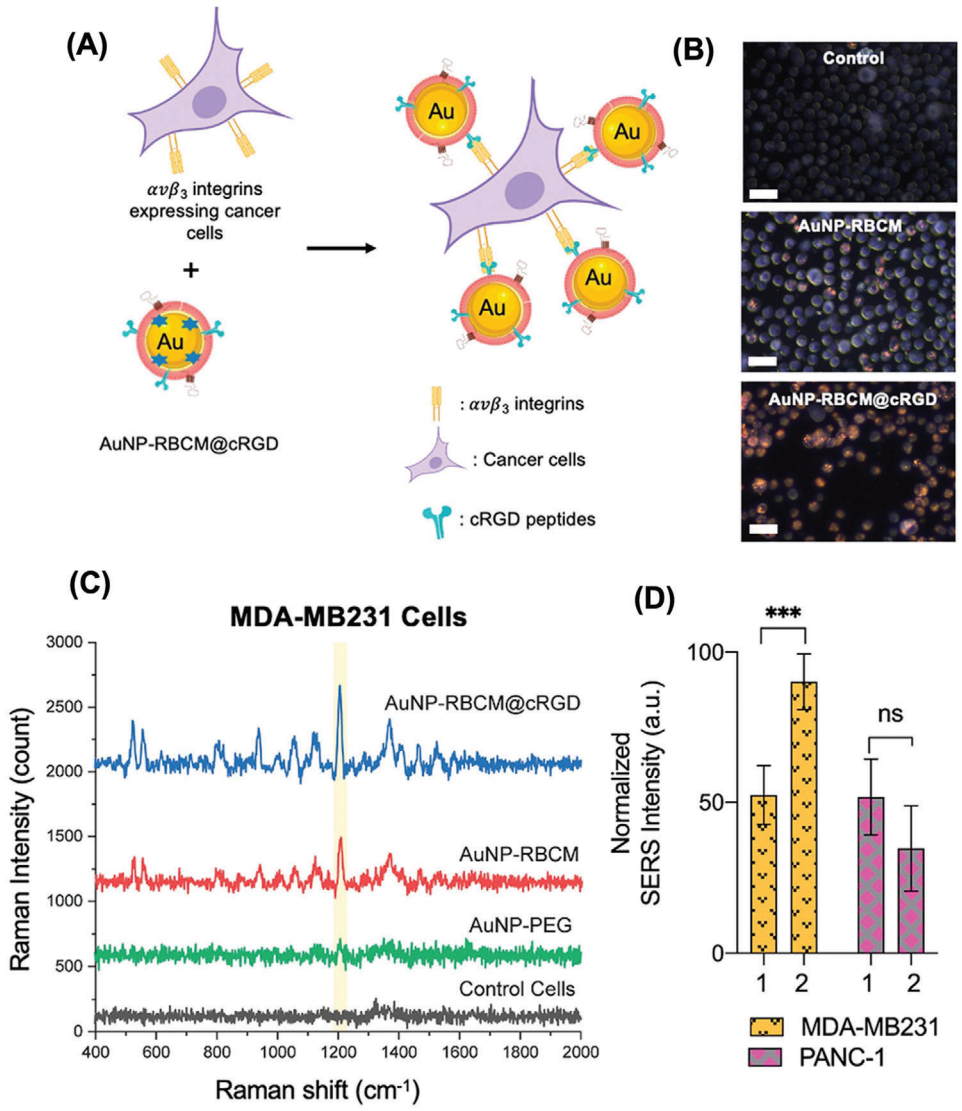


**Figure 27.** Development of cell-membrane coated AuNPs for spectroscopic detection of metastatic tumor cells and nanotherapeutics delivery into tumor cells. A) Schematic depicting the targeting and spectroscopic detection of $\alpha v\beta 3$ expressing cancer cells using biomimetic and tumor-targeted AuNP-RBCM@cRGD. B) Dark-field microscopy images of MDA-MB231 cells incubated with PBS 1×, AuNP-RBCM, and AuNP-RBCM@cRGD, respectively. C) Raman spectra of control cells, AuNP-PEG, AuNP-RBCM, and AuNP-RBCM@cRGD treated MDA-MB231 cells after overnight incubation. Each sample contains NP cell suspensions dispersed in PBS. Spectra were acquired at a laser power of 200 mW and an integration time of 2 s. D) Normalized Raman intensity of 1) AuNP-RBCM and 2) AuNP-RBCM@cRGD treated cells at 1205 $cm^{-1}$ Raman peak. MDA-MB231 and PANC-1 were selected as representative cell lines with and without cRGD-targeted receptors, respectively. Reproduced with permission.[146] Copyright 2022, American Chemical Society.

apeutics to the target tumor has been pursued by multiple research groups. Nanoparticle-based drug delivery systems offer a multitude of benefits compared to the ones conventionally used in clinics. Some of these benefits include improved bioavailability of drugs, delivery efficacy, tumor-specific targeting attributes, and prolonged blood circulation. Owing to their unique attributes, a new era has thus begun to develop novel nanoengineering approaches to modulate nanosized systems of MNPs or AuNPs and others to achieve more controlled nanotherapeutics delivery systems. However, despite the added advantages of such nanoscale platforms, concerns about preparations and applications of such systems still need to be addressed. For this application, it should be noted that nanoparticles enter the biological environment of living systems, interacting with biomolecules such as proteins, lipids, etc. as they navigate toward the diseased microenvironment. However, if not catered to meticulously, nanoparticle attributes such as their size, surface charge, or chemical compositions can inadvertently trigger adverse effects instead of intended benefits, particularly in in vitro or in vivo systems.

One of the seminal advantages of nanoparticle carriers (nanocarriers) over conventional drug delivery platforms such as chemotherapeutics, is that they play a crucial role in reducing side effects and potential toxicity of drugs on healthy cells. However, depending on their physicochemical properties, these

carrier systems have the potential to be damaging and toxic. The chemical composition of the nanoparticles is one of the primary factors that determines their toxicity as a carrier. The widespread integration of nanoparticles in various aspects of our daily lives is largely due to the rapid growth of the nanotechnology industry. While some of these materials serve medical purposes, they can also pose risks to human health, especially when introduced into the body's systems, particularly the lungs. Adverse effects resulting from nanoparticle exposure may include inflammation, oxidative stress, fibrosis, and genotoxicity, which can contribute to pulmonary diseases and injuries in other tissues. Hence, it is imperative to carefully assess the potential harmful effects of nanomaterials, especially when they are intended for use in therapeutic applications. This consideration is vital to ensure the safety and efficacy of nanoparticle-based therapies.

The surface-to-volume aspect ratio for nanoparticles is another attribute that allows the distinction of their properties when compared to their bulk counterparts. Changes in aspect ratio directly influence size-dependent properties such as reactivity, diffusion, and distribution.[449,450] Nanoparticles exhibit distinct traits in a biologically relevant milieu based on their hydrodynamic diameter (size). Nanoparticles less than 10 nm are swiftly eliminated from the circulatory system following systemic administration, while those with sizes ranging from 100 to 200 nm remain in circulation for longer periods. Additionally, different sizes correspond to varying levels of toxicity. Due to their high aspect ratio, smaller particles demonstrate uncontrolled reactivity with biological molecules and a tendency to aggregate or form clusters spontaneously. This could culminate in the possibility of why microparticles are generally less toxic than nanoparticles of the same material. Moreover, the size of the carrier determines the mechanism of cell penetration for drug-loaded particles. The surface charge of nanoparticle-based carriers, usually referred to as the zeta potential is often correlated with their hydrodynamic diameter. The values of zeta potential often serve as a strong indicator of the colloidal stability of nanoparticles in both aqueous solutions and in a biological milieu. Having high negative and positive zeta potential values for nanoparticles used for drug delivery is often preferred as they avoid aggregation scenarios in vitro or in vivo. Cellular internalization of these nanocarriers to tumor cells is also dictated by the surface charge/ zeta potential values. For example, anionic nanoparticles tend to internalize more effectively than the cationic or neutral ones.[451] Contrastingly, for lipid-based nanocarriers, circulation half-life drastically changes with zeta potential.[362,452]

Nanomaterial-based drug delivery technologies show significant promise for the future of medicine. By utilizing tiny nanocarriers to target specific areas within the body, researchers aim to enhance treatment effectiveness while minimizing side effects. The potential applications of this technology are vast, spanning areas such as cancer treatment, immunotherapy, and gene therapy, among others. While nanomaterial-based drug delivery holds the potential to revolutionize medicine, it is crucial to acknowledge existing limitations and drawbacks that must be addressed. These include concerns about toxicity, limited safety profiles, insufficient loading, and entrapment into specific organs, as well as the necessity for comprehensive nanotoxicology assessments in living organisms.

Further research is imperative to enhance the efficacy and safety of nanomaterial-based formulations, facilitating their transition from laboratory settings to clinical use. Despite these grand challenges, the outlook for nanomaterial-based drug delivery remains promising. Continued research and development efforts are expected to overcome these limitations, ultimately improving the efficacy and safety of these formulations, and advancing their clinical utility.

## 6. Conclusions and Future Perspectives

Recent progress in synthesis methods at the nanoscale has enabled the fabrication of a plethora of polymer nanoparticles with a variety of sizes, compositions, and physicochemical properties. In this work, we provide an overview of several synthesis methods that have succeeded in the formulation of these materials, along with a summary of the most recent findings regarding their use in biomedical applications. More specifically, we discuss the main synthesis routes of nanoparticles with special magnetic and optical properties, such as MNPs and AuNPs, and how these can be coated with different polymers such as PEG, PAA, PDA, and PVA, among others. Within the available synthesis methods, we highlight the benefits of green synthetic approaches for the fabrication of the nanoparticles, that overcome traditional issues reported by popular physical and chemical routes, such as the high cost and use of toxic solutions and precursors, or the generation of hazardous byproducts, which is especially crucial for their later application to biological systems.

Furthermore, we also discuss the role that these polymer-coated nanomaterials have played in the recent development in biomedical and biological fields. Specifically, we highlight how these nanoparticles have been successfully employed in a variety of applications, including MRI, as novel contrast agents for the generation of high-quality, high-resolution images, or in cancer therapy via hyperthermia, drug delivery, or photothermal tumor destruction. Additionally, novel techniques involving polymer-coated MNPs have been devised for the isolation of diverse cell populations and biomolecules, including rare entities such as CTCs for cancer diagnosis and prognosis. Nevertheless, work is still underway to translate this research into clinical implementation. Efforts in the field should be directed towards the assessment of the safety and efficacy of the nanoparticles, including their long-term stability, biocompatibility, and potential toxicity via the design of both in vitro and in vivo studies. The scientific community should address these issues and concerns before the particles are fully implemented to minimize any potential harm. However, despite these challenges, we emphasize that further advancements in the field may be able to bring these technologies a step forward and make the effective clinical application of polymer-coated nanoparticles a viable option with great potential in theranostics and personalized medicine. Continued research and development in this direction will enhance our understanding of these materials and their potential benefits along with minimization strategies of their toxicological properties and adverse effects, to overcome current challenges, make the most out of polymer-coated nanoparticles, and facilitate their transition from laboratory settings to clinical use.

## Acknowledgements

B.R., A.H., X.W., and P.R.I. contributed equally to this work. This study was financially supported by Texas Tech University through HEF New Faculty Startup, NRUF Start Up, and Core Research Support Fund. B. R. acknowledges the Distinguished Graduate Student Assistantships (DGSA) offered by Texas Tech University.

## Conflict of Interest

The authors declare no conflict of interest.

## Keywords

bioassay, biomedicine, cell membranes, gold nanoparticle, magnetic nanoparticle, nanoparticle, polymer, synthesis

Received: April 1, 2024
Revised: May 28, 2024
Published online: June 25, 2024

[1] A. Eftekhari, S. Maleki Dizaj, E. Ahmadian, A. Przekora, S. M. Hosseiniyan Khatibi, M. Ardalan, S. Zununi Vahed, M. Valiyeva, S. Mehraliyeva, R. Khalilov, M. Hasanzadeh, *Materials* **2021**, *14*, 2939.
[2] K. Markandan, Y. W. Tiong, R. Sankaran, S. Subramanian, U. D. Markandan, V. Chaudhary, A. Numan, M. Khalid, R. Walvekar, *Biotechnol. Genet. Eng. Rev.* **2022**, 1.
[3] M. Khalil, G. T. M. Kadja, Moh. M. Ilmi, *J. Ind. Eng. Chem.* **2021**, *93*, 78.
[4] B. Rezaei, P. Yari, S. M. Sanders, H. Wang, V. K. Chugh, S. Liang, S. Mostufa, K. Xu, J.-P. Wang, J. Gómez-Pastora, *Small* **2024**, *20*, 2304848.
[5] A. Pavlicek, S. Neubauer, C. Zafiu, M. Huber-Humer, E.-K. Ehmoser, F. Part, *Environ. Pollut.* **2023**, *317*, 120461.
[6] X. Bai, Y. Wang, Z. Song, Y. Feng, Y. Chen, D. Zhang, L. Feng, *Int. J. Mol. Sci.* **2020**, *21*, 2480.
[7] T. I. Janjua, Y. Cao, C. Yu, A. Popat, *Nat. Rev. Mater.* **2021**, *6*, 1072.
[8] C. Buzea, I. I. Pacheco, K. Robbie, *Biointerphases* **2007**, *2*, MR17.
[9] J. Gómez-Pastora, E. Bringas, I. Ortiz, *Chem. Eng. J.* **2014**, *256*, 187.
[10] K. Wu, D. Su, J. Liu, R. Saha, J.-P. Wang, *Nanotechnology* **2019**, *30*, 502003.
[11] P. Yari, S. Liang, V. K. Chugh, B. Rezaei, S. Mostufa, V. D. Krishna, R. Saha, M. C.-J. Cheeran, J.-P. Wang, J. Gómez-Pastora, K. Wu, *Anal. Chem.* **2023**, *95*, 15419.
[12] J. Gómez-Pastora, X. Xue, I. H. Karampelas, E. Bringas, E. P. Furlani, I. Ortiz, *Sep. Purif. Technol.* **2017**, *172*, 16.
[13] K. Wu, D. Su, R. Saha, D. Wong, J.-P. Wang, *J. Phys. Appl. Phys.* **2019**, *52*, 173001.
[14] P. Yuan, Y. Min, Z. Zhao, *Biomater. Adv.* **2023**, *151*, 213466.
[15] N. Shahbazi, R. Zare-Dorabei, S. M. Naghib, *Mater. Sci. Eng. C* **2021**, *127*, 112249.
[16] D. Dragoman, *Nanomaterials* **2023**, *13*, 1154.
[17] D. Astruc, *Chem. Rev.* **2020**, *120*, 461.
[18] J. Gómez Pastora, E. Bringas Elizalde, I. Ortiz Uribe, UCrea: Design of novel adsorption processes for the removal of arsenic from polluted groundwater employing functionalized magnetic nanoparticles, Universidad de Cantabria, Spain, **2016**.
[19] K. McNamara, S. A. M. Tofail, *Adv. Phys. X* **2017**, *2*, 54.
[20] S. Bharathala, P. Sharma, in *Nanotechnology in Modern Animal Biotechnology*, Elsevier, Cham **2019**, pp. 113–132.
[21] H. A. Nguyen, I. Srivastava, D. Pan, M. Gruebele, *ACS Nano* **2020**, *14*, 6127.
[22] S. K. Misra, I. Srivastava, I. Tripathi, E. Daza, F. Ostadhossein, D. Pan, *J. Am. Chem. Soc.* **2017**, *139*, 1746.
[23] I. Srivastava, S. K. Misra, F. Ostadhossein, E. Daza, J. Singh, D. Pan, *Nano Res.* **2017**, *10*, 3269.
[24] I. Srivastava, S. K. Misra, S. Bangru, K. A. Boateng, J. A. N. T. Soares, A. S. Schwartz-Duval, A. Kalsotra, D. Pan, *ACS Appl. Mater. Interfaces* **2020**, *12*, 16137.
[25] I. Srivastava, M. S. Khan, K. Dighe, M. Alafeef, Z. Wang, T. Banerjee, T. Ghonge, L. M. Grove, R. Bashir, D. Pan, *Small Methods* **2020**, *4*, 2000099.
[26] M. Alafeef, I. Srivastava, T. Aditya, D. Pan, *Small* **2024**, *20*, 2303937.
[27] B. Begines, T. Ortiz, M. Pérez-Aranda, G. Martínez, M. Merinero, F. Argüelles-Arias, A. Alcudia, *Nanomaterials* **2020**, *10*, 1403.
[28] A. Zielińska, F. Carreiró, A. M. Oliveira, A. Neves, B. Pires, D. N. Venkatesh, A. Durazzo, M. Lucarini, P. Eder, A. M. Silva, A. Santini, E. B. Souto, *Molecules* **2020**, *25*, 3731.
[29] S. Perumal, *Polymers* **2022**, *14*, 5449.
[30] J. Liu, D. Su, K. Wu, J.-P. Wang, *J. Nanoparticle Res.* **2020**, *22*, 1.
[31] S. Ciannella, X. Wu, C. González-Fernández, B. Rezaei, J. Strayer, H. Choe, K. Wu, J. Chalmers, J. Gomez-Pastora, *Micromachines* **2023**, *14*, 2107.
[32] I. Yildiz, *Nanotechnol. Rev.* **2016**, *5*, 331.
[33] B. Rezaei, A. Kermanpur, S. Labbaf, *J. Magn. Magn. Mater.* **2019**, *481*, 16.
[34] A. Dasari, J. Xue, S. Deb, *Nanomaterials* **2022**, *12*, 757.
[35] H. Zhang, J. Xia, X. Pang, M. Zhao, B. Wang, L. Yang, H. Wan, J. Wu, S. Fu, *Mater. Sci. Eng. C* **2017**, *73*, 537.
[36] K. Wu, R. Saha, D. Su, V. D. Krishna, J. Liu, M. C.-J. Cheeran, J.-P. Wang, *ACS Appl. Nano Mater.* **2020**, *3*, 9560.
[37] J. Kudr, Y. Haddad, L. Richtera, Z. Heger, M. Cernak, V. Adam, O. Zitka, *Nanomaterials* **2017**, *7*, 243.
[38] S. Shukla, R. Khan, A. Daverey, *Environ. Technol. Innov.* **2021**, *24*, 101924.
[39] M. Roostaee, I. Sheikhshoaie, *Curr. Biochem. Eng.* **2020**, *6*, 91.
[40] D. Alromi, S. Madani, A. Seifalian, *Polymers* **2021**, *13*, 4146.
[41] S. Ying, Z. Guan, P. C. Ofoegbu, P. Clubb, C. Rico, F. He, J. Hong, *Environ. Technol. Innov.* **2022**, *26*, 102336.
[42] Y. B. Pottathara, Y. Grohens, V. Kokol, N. Kalarikkal, S. Thomas, in *Nanomaterial Synthesis*, Elsevier, Cham **2019**, pp. 1–25.
[43] S. Majidi, F. Zeinali Sehrig, S. M. Farkhani, M. Soleymani Goloujeh, A. Akbarzadeh, *Artif. Cells Nanomedicine Biotechnol.* **2016**, *44*, 722.
[44] S. Tazikeh, A. Akbari, A. Talebi, E. Talebi, *Mater. Sci.-Pol.* **2014**, *32*, 98.
[45] R. Kripal, A. K. Gupta, R. K. Srivastava, S. K. Mishra, *Spectrochim. Acta. A. Mol. Biomol. Spectrosc.* **2011**, *79*, 1605.
[46] R. Srinivasan, R. Yogamalar, A. C. Bose, *Mater. Res. Bull.* **2010**, *45*, 1165.
[47] J. R. Vargas-Ortiz, C. Gonzalez, K. Esquivel, *Processes* **2022**, *10*, 2282.
[48] S.-N. Sun, C. Wei, Z.-Z. Zhu, Y.-L. Hou, S. S. Venkatraman, Z.-C. Xu, *Chin. Phys. B* **2014**, *23*, 037503.
[49] H. Mohammadi, E. Nekobahr, J. Akhtari, M. Saeedi, J. Akbari, F. Fathi, *Toxicol. Rep.* **2021**, *8*, 331.
[50] M. A. Willard, L. K. Kurihara, E. E. Carpenter, S. Calvin, V. G. Harris, *Int. Mater. Rev.* **2004**, *49*, 125.
[51] J. A. Darr, J. Zhang, N. M. Makwana, X. Weng, *Chem. Rev.* **2017**, *117*, 11125.
[52] K. Byrappa, T. Adschiri, *Prog. Cryst. Growth Charact. Mater.* **2007**, *53*, 117.
[53] M. Rajamathi, R. Seshadri, *Curr. Opin. Solid State Mater. Sci.* **2002**, *6*, 337.
[54] X. Guo, Q. Zhang, X. Ding, Q. Shen, C. Wu, L. Zhang, H. Yang, *J. Sol-Gel Sci. Technol.* **2016**, *79*, 328.
[55] M. Parashar, V. K. Shukla, R. Singh, *J. Mater. Sci. Mater. Electron.* **2020**, *31*, 3729.

[56] L. P. Singh, S. K. Bhattacharyya, R. Kumar, G. Mishra, U. Sharma, G. Singh, S. Ahalawat, *Adv. Colloid Interface Sci.* **2014**, *214*, 17.
[57] C. Giordano, M. Antonietti, *Nano Today* **2011**, *6*, 366.
[58] S. F. Hasany, I. Ahmed, R. J. A. Rehman, *Nanosci. Nanotechnol.* **2013**, *2*, 148.
[59] A. K. Ganguli, A. Ganguly, S. Vaidya, *Chem. Soc. Rev.* **2010**, *39*, 474.
[60] M. A. Malik, M. Y. Wani, M. A. Hashim, *Arab. J. Chem.* **2012**, *5*, 397.
[61] J. N. Solanki, Z. V. P. Murthy, *Ind. Eng. Chem. Res.* **2011**, *50*, 12311.
[62] I. R. Singh, A. K. Pulikkal, *OpenNano* **2022**, *8*, 100066.
[63] M.-C. Ioncica, S. Bandyopadhyay, N. Bali, V. Socoliuc, S. I. Bernad, *Magnetochemistry* **2023**, *9*, 99.
[64] I. Capek, *Adv. Colloid Interface Sci.* **2004**, *110*, 49.
[65] K. Margulis-Goshen, S. Magdassi, *Curr. Opin. Colloid Interface Sci.* **2012**, *17*, 290.
[66] S. Asgari, A. H. Saberi, D. J. McClements, M. Lin, *Trends Food Sci. Technol.* **2019**, *86*, 118.
[67] G. B. Oliveira-Filho, J. J. Atoche-Medrano, F. F. H. Aragón, J. C. Mantilla Ochoa, D. G. Pacheco-Salazar, S. W. Da Silva, J. A. H. Coaquira, *Appl. Surf. Sci.* **2021**, *563*, 150290.
[68] S. Navaladian, B. Viswanathan, R. P. Viswanath, T. K. Varadarajan, *Nanoscale Res. Lett.* **2007**, *2*, 44.
[69] R. Al-Gaashani, S. Radiman, N. Tabet, A. R. Daud, *J. Alloys Compd.* **2013**, *550*, 395.
[70] C.-C. Lin, Y.-Y. Li, *Mater. Chem. Phys.* **2009**, *113*, 334.
[71] H. Kominami, J. Kato, Y. Takada, Y. Doushi, B. Ohtani, S. Nishimoto, M. Inoue, T. Inui, Y. Kera, *Catal. Lett.* **1997**, *46*, 235.
[72] A. Dumbrava, V. Ciupina, B. Jurca, G. Prodan, E. Segal, M. Brezeanu, *J. Therm. Anal. Calorim.* **2005**, *81*, 399.
[73] C. Wang, M. Chi, D. Li, D. Van Der Vliet, G. Wang, Q. Lin, J. F. Mitchell, K. L. More, N. M. Markovic, V. R. Stamenkovic, *ACS Catal.* **2011**, *1*, 1355.
[74] R. Nagpal, M. Gusain, in *Graphene, Nanotubes and Quantum Dots-Based Nanotechnology*, Elsevier, Cham **2022**, pp. 599–630.
[75] A. Das, P. T. Snee, *ChemPhysChem* **2016**, *17*, 598.
[76] A. Lu, E. emsp14L Salabas, F. Schüth, *Angew. Chem., Int. Ed.* **2007**, *46*, 1222.
[77] G. G. Flores-Rojas, F. López-Saucedo, R. Vera-Graziano, E. Mendizabal, E. Bucio, *Macromol* **2022**, *2*, 374.
[78] M. R. Zamani Kouhpanji, B. J. H. Stadler, *Sensors* **2020**, *20*, 2554.
[79] I. O. Perez De Berti, M. V. Cagnoli, G. Pecchi, J. L. Alessandrini, S. J. Stewart, J. F. Bengoa, S. G. Marchetti, *Nanotechnology* **2013**, *24*, 175601.
[80] S. Kumar, P. Bhushan, S. Bhattacharya, *Environ. Chem. Med. Sens.* **2018**, 167.
[81] J. Liu, K. Wu, J.-P. Wang, *AIP Adv.* **2016**, *6*, 056126.
[82] A.-G. Niculescu, C. Chircov, A. M. Grumezescu, *Methods* **2022**, *199*, 16.
[83] M. Salavati-Niasari, J. Javidi, M. Dadkhah, *Comb. Chem. High Throughput Screen.* **2013**, *16*, 458.
[84] A. Ali, T. Shah, R. Ullah, P. Zhou, M. Guo, M. Ovais, Z. Tan, Y. Rui, *Front. Chem.* **2021**, *9*, 629054.
[85] M. Kim, S. Osone, T. Kim, H. Higashi, T. Seto, *KONA Powder Part. J.* **2017**, *34*, 80.
[86] P. Grammatikopoulos, S. Steinhauer, J. Vernieres, V. Singh, M. Sowwan, *Adv. Phys. X* **2016**, *1*, 81.
[87] T. Tsuzuki, P. G. McCormick, *J. Mater. Sci.* **2004**, *39*, 5143.
[88] J. Joy, A. Krishnamoorthy, A. Tanna, V. Kamathe, R. Nagar, S. Srinivasan, *Appl. Sci.* **2022**, *12*, 9312.
[89] S. Prabakaran, M. Rajan, in *Comprehensive Analytical Chemistry*, Elsevier, Cham **2021**, pp. 1–47.
[90] M. M. Can, S. Ozcan, A. Ceylan, T. Firat, *Mater. Sci. Eng. B* **2010**, *172*, 72.
[91] A. Pineda, A. M. Balu, J. M. Campelo, R. Luque, A. A. Romero, J. C. Serrano-Ruiz, *Catal. Today* **2012**, *187*, 65.
[92] A. E.-M. A. Mohamed, M. A. Mohamed, *Magn. Nanostructures Environ. Agric. Appl.* **2019**, 1.
[93] S. Dutz, R. Hergt, J. Mürbe, R. Müller, M. Zeisberger, W. Andrä, J. Töpfer, M. E. Bellemann, *J. Magn. Magn. Mater.* **2007**, *308*, 305.
[94] K. Wu, J. Liu, R. Saha, B. Ma, D. Su, C. Peng, J. Sun, J.-P. Wang, *ACS Omega* **2020**, *5*, 11756.
[95] K. Wu, J. Liu, R. Saha, B. Ma, D. Su, V. K. Chugh, J.-P. Wang, *ACS Appl. Nano Mater.* **2021**, *4*, 4409.
[96] M. S. El-Eskandarany, A. Al-Hazza, L. A. Al-Hajji, N. Ali, A. A. Al-Duweesh, M. Banyan, F. Al-Ajmi, *Nanomaterials* **2021**, *11*, 2484.
[97] P. F. M. De Oliveira, R. M. Torresi, F. Emmerling, P. H. C. Camargo, *J. Mater. Chem. A* **2020**, *8*, 16114.
[98] M. Malekzadeh, M. T. Swihart, *Chem. Soc. Rev.* **2021**, *50*, 7132.
[99] P. Biehl, M. von der Luhe, S. Dutz, F. H. Schacher, *Polymers* **2018**, *10*, 28.
[100] H. Zeng, X. Du, S. C. Singh, S. A. Kulinich, S. Yang, J. He, W. Cai, *Adv. Funct. Mater.* **2012**, *22*, 1333.
[101] A. Wazeer, A. Das, A. Sinha, A. Karmakar, *J. Inst. Eng. India Ser. D* **2023**, *104*, 413.
[102] G. K. Yogesh, S. Shukla, D. Sastikumar, P. Koinkar, *Appl. Phys. A* **2021**, *127*, 810.
[103] S.-B. Wen, X. Mao, R. Greif, R. F. Russo, *J. Appl. Phys.* **2006**, 100.
[104] D. Zhang, H. Wada, *Handb. Laser Micro- Nano-Eng.* **2020**, *1*.
[105] F. Mafuné, J. Kohno, Y. Takeda, T. Kondow, H. Sawabe, *J. Phys. Chem. B* **2000**, *104*, 8333.
[106] D. Zhang, B. Gokce, S. Barcikowski, *Chem. Rev.* **2017**, *117*, 3990.
[107] M. C. Sportelli, M. Izzi, A. Volpe, M. Clemente, R. A. Picca, A. Ancona, P. M. Lugarà, G. Palazzo, N. Cioffi, *Antibiotics* **2018**, *7*, 67.
[108] B. S. Hettiarachchi, Y. Takaoka, Y. Uetake, Y. Yakiyama, H. H. Lim, T. Taira, M. Maruyama, Y. Mori, H. Y. Yoshikawa, H. Sakurai, *Ind. Chem. Mater.* **2024**.
[109] V. Harish, M. M. Ansari, D. Tewari, M. Gaur, A. B. Yadav, M.-L. García-Betancourt, F. M. Abdel-Haleem, M. Bechelany, A. Barhoum, *Nanomaterials* **2022**, *12*, 3226.
[110] L. Mascaretti, C. Mancarella, M. Afshar, Š. Kment, A. L. Bassi, A. Naldoni, *Nanotechnology* **2023**, *34*, 502003.
[111] Y. Manawi, Ihsanullah, A. Samara, T. Al-Ansari, M. Atieh, *Materials* **2018**, *11*, 822.
[112] A. V. Samrot, C. S. Sahithya, J. Selvarani, S. K. Purayil, P. Ponnaiah, *Curr. Res. Green Sustain. Chem.* **2021**, *4*, 100042.
[113] M. Niedermaier, T. Schwab, O. Diwald, *Met. Oxide Nanoparticles Form. Funct. Prop. Interfaces* **2021**, *1*, 67.
[114] V. N. Popok, O. Kylián, *Appl. Nano* **2020**, *1*, 4.
[115] R. López-Martín, B. S. Burgos, P. S. Normile, J. A. De Toro, C. Binns, *Nanomaterials* **2021**, *11*, 2803.
[116] P. Rai-Choudhury, *Handbook of Microlithography, Micromachining, and Microfabrication: Microlithography*, SPIE Press, Bellingham, WA **1997**.
[117] L. Signorini, L. Pasquini, L. Savini, R. Carboni, F. Boscherini, E. Bonetti, A. Giglia, M. Pedio, N. Mahne, S. Nannarone, *Phys. Rev. B* **2003**, *68*, 195423.
[118] X. Li, H. Xu, Z.-S. Chen, G. Chen, *J. Nanomater.* **2011**, *2011*, 1.
[119] A. D. Mihai, C. Chircov, A. M. Grumezescu, A. M. Holban, *Int. J. Mol. Sci.* **2020**, *21*, 7355.
[120] S. Ghosh, R. Ahmad, M. Zeyaullah, S. K. Khare, *Front. Chem.* **2021**, *9*, 626834.
[121] P. Singh, Y.-J. Kim, D. Zhang, D.-C. Yang, *Trends Biotechnol.* **2016**, *34*, 588.
[122] O. P. Bolade, A. B. Williams, N. U. Benson, *Environ. Nanotechnol. Monit. Manag.* **2020**, *13*, 100279.
[123] R. Singh, P. Wagh, S. Wadhwani, S. Gaidhani, A. Kumbhar, J. Bellare, B. A. Chopade, *Int. J. Nanomed.* **2013**, 4277.
[124] S. He, Z. Guo, Y. Zhang, S. Zhang, J. Wang, N. Gu, *Mater. Lett.* **2007**, *61*, 3984.

[125] D. Mandal, M. E. Bolander, D. Mukhopadhyay, G. Sarkar, P. Mukherjee, *Appl. Microbiol. Biotechnol.* **2006**, *69*, 485.
[126] S. Jadoun, N. P. S. Chauhan, P. Zarrintaj, M. Barani, R. S. Varma, S. Chinnam, A. Rahdar, *Environ. Chem. Lett.* **2022**, *20*, 3153.
[127] E. Castro-Longoria, A. R. Vilchis-Nestor, M. Avalos-Borja, *Colloids Surf. B Biointerfaces* **2011**, *83*, 42.
[128] Z. Molnár, V. Bódai, G. Szakacs, B. Erdélyi, Z. Fogarassy, G. Sáfrán, T. Varga, Z. Kónya, E. Tóth-Szeles, R. Szűcs, *Sci. Rep.* **2018**, *8*, 3943.
[129] F. Niknejad, M. Nabili, R. D. Ghazvini, M. Moazeni, *Curr. Med. Mycol.* **2015**, *1*, 17.
[130] P. Prema, P. A. Iniya, G. Immanuel, *RSC Adv.* **2016**, *6*, 4601.
[131] M. Fatemi, N. Mollania, M. Momeni-Moghaddam, F. Sadeghifar, *J. Biotechnol.* **2018**, *270*, 1.
[132] G. A. Marcelo, C. Lodeiro, J. L. Capelo, J. Lorenzo, E. Oliveira, *Mater. Sci. Eng. C* **2020**, *106*, 110104.
[133] Y. P. Yew, K. Shameli, M. Miyake, N. B. B. A. Khairudin, S. E. B. Mohamad, T. Naiki, K. X. Lee, *Arab. J. Chem.* **2020**, *13*, 2287.
[134] A. K. Mittal, Y. Chisti, U. C. Banerjee, *Biotechnol. Adv.* **2013**, *31*, 346.
[135] S. Jadoun, R. Arif, N. K. Jangid, R. K. Meena, *Environ. Chem. Lett.* **2021**, *19*, 355.
[136] F. E. Ettadili, S. Aghris, F. Laghrib, A. Farahi, S. Saqrane, M. Bakasse, S. Lahrich, M. A. El Mhammedi, *J. Mol. Struct.* **2022**, *1248*, 131538.
[137] K. Vijayaraghavan, T. Ashokkumar, *J. Environ. Chem. Eng.* **2017**, *5*, 4866.
[138] J. O. Adeyemi, E. E. Elemike, D. C. Onwudiwe, *Mater. Res. Express* **2019**, *6*, 125091.
[139] P. Kuppusamy, M. M. Yusoff, G. P. Maniam, N. Govindan, *Saudi Pharm. J.* **2016**, *24*, 473.
[140] E.-A. Moacă, V. Socoliuc, D. Stoian, C. Watz, D. Flondor, C. Păcurariu, R. Ianoș, C. I. Rus, L. Barbu-Tudoran, A. Semenescu, *Magnetochemistry* **2022**, *8*, 145.
[141] L. Soltys, O. Olkhovyy, T. Tatarchuk, M. Naushad, *Magnetochemistry* **2021**, *7*, 145.
[142] J. O. Adeyemi, A. O. Oriola, D. C. Onwudiwe, A. O. Oyedeji, *Biomolecules* **2022**, *12*, 627.
[143] T. Tatarchuk, M. Myslin, I. Lapchuk, O. Olkhovyy, N. Danyliuk, V. Mandzyuk, *Phys. Chem. Solid State* **2021**, *22*, 195.
[144] G. Sharmila, M. Thirumarimurugan, C. Muthukumaran, *Microchem. J.* **2019**, *145*, 578.
[145] M. Umadevi, M. R. Bindhu, V. Sathe, *J. Mater. Sci. Technol.* **2013**, *29*, 317.
[146] I. Srivastava, R. Xue, J. Jones, H. Rhee, K. Flatt, V. Gruev, S. Nie, *ACS Nano* **2022**, *16*, 8051.
[147] P. Zhao, N. Li, D. Astruc, *Coord. Chem. Rev.* **2013**, *257*, 638.
[148] G. Frens, *Kolloid-Z. Z. Für Polym.* **1972**, *250*, 736.
[149] G. Frens, *Nat. Phys. Sci.* **1973**, *241*, 20.
[150] J. Kimling, M. Maier, B. Okenve, V. Kotaidis, H. Ballot, A. Plech, *J. Phys. Chem. B* **2006**, *110*, 15700.
[151] X. Ji, X. Song, J. Li, Y. Bai, W. Yang, X. Peng, *J. Am. Chem. Soc.* **2007**, *129*, 13939.
[152] A. Kumar, S. Murugesan, V. Pushparaj, J. Xie, C. Soldano, G. John, O. Nalamasu, P. M. Ajayan, R. J. Linhardt, *Small* **2007**, *3*, 429.
[153] C. Li, D. Li, G. Wan, J. Xu, W. Hou, *Nanoscale Res. Lett.* **2011**, *6*, 440.
[154] S. Yang, Y. Wang, Q. Wang, R. Zhang, B. Ding, *Colloids Surf. Physicochem. Eng. Asp.* **2007**, *301*, 174.
[155] I. Ojea-Jiménez, N. G. Bastús, V. Puntes, *J. Phys. Chem. C* **2011**, *115*, 15752.
[156] S. Link, M. A. El-Sayed, *J. Phys. Chem. B* **1999**, *103*, 4212.
[157] W. Patungwasa, J. H. Hodak, *Mater. Chem. Phys.* **2008**, *108*, 45.
[158] A. A. Volkert, V. Subramaniam, A. J. Haes, *Chem. Commun.* **2011**, *47*, 478.
[159] K. Zabetakis, W. E. Ghann, S. Kumar, M.-C. Daniel, *Gold Bull.* **2012**, *45*, 203.
[160] M. Brust, M. Walker, D. Bethell, D. J. Schiffrin, R. Whyman, *J Chem Soc Chem Commun* **1994**, *0*, 801.
[161] N. R. Jana, L. Gearheart, C. J. Murphy, *Chem. Mater.* **2001**, *13*, 2313.
[162] M. Sakamoto, M. Fujistuka, T. Majima, *J. Photochem. Photobiol. C Photochem. Rev.* **2009**, *10*, 33.
[163] A. S. Schwartz-Duval, C. J. Konopka, P. Moitra, E. A. Daza, I. Srivastava, E. V. Johnson, T. L. Kampert, S. Fayn, A. Haran, L. W. Dobrucki, D. Pan, *Nat. Commun.* **2020**, *11*, 4530.
[164] J. Xie, Y. Zheng, J. Y. Ying, *J. Am. Chem. Soc.* **2009**, *131*, 888.
[165] C. J. Murphy, T. K. Sau, A. M. Gole, C. J. Orendorff, J. Gao, L. Gou, S. E. Hunyadi, T. Li, *J. Phys. Chem. B* **2005**, *109*, 13857.
[166] P. K. Jain, K. S. Lee, I. H. El-Sayed, M. A. El-Sayed, *J. Phys. Chem. B* **2006**, *110*, 7238.
[167] A. V. Alekseeva, V. A. Bogatyrev, B. N. Khlebtsov, A. G. Mel'nikov, L. A. Dykman, N. G. Khlebtsov, *Colloid J.* **2006**, *68*, 661.
[168] A. M. Alkilany, L. B. Thompson, S. P. Boulos, P. N. Sisco, C. J. Murphy, *Adv. Drug Delivery Rev.* **2012**, *64*, 190.
[169] E. Gournaris, W. Park, S. Cho, D. J. Bentrem, A. C. Larson, D.-H. Kim, *ACS Appl. Mater. Interfaces* **2019**, *11*, 21353.
[170] B. E. Brinson, J. B. Lassiter, C. S. Levin, R. Bardhan, N. Mirin, N. J. Halas, *Langmuir* **2008**, *24*, 14166.
[171] S. J. Oldenburg, R. D. Averitt, S. L. Westcott, N. J. Halas, *Chem. Phys. Lett.* **1998**, *288*, 243.
[172] R. D. Averitt, D. Sarkar, N. J. Halas, *Phys. Rev. Lett.* **1997**, *78*, 4217.
[173] H. Wang, K. Fu, R. A. Drezek, N. J. Halas, *Appl. Phys. B* **2006**, *84*, 191.
[174] S. E. Skrabalak, J. Chen, L. Au, X. Lu, X. Li, Y. Xia, *Adv. Mater.* **2007**, *19*, 3177.
[175] S. E. Skrabalak, J. Chen, Y. Sun, X. Lu, L. Au, C. M. Cobley, Y. Xia, *Acc. Chem. Res.* **2008**, *41*, 1587.
[176] B. Sun, Y. Z. Long, M. M. Li, X. J. Hu, Y. Q. Qi, S. Y. Zhou, P. Chen, *Adv. Mater. Res.* **2013**, *650*, 200.
[177] Y. Xia, W. Li, C. M. Cobley, J. Chen, X. Xia, Q. Zhang, M. Yang, E. C. Cho, P. K. Brown, *Acc. Chem. Res.* **2011**, *44*, 914.
[178] I. Srivastava, R. Xue, H.-K. Huang, Z. Wang, J. Jones, I. Vasquez, S. Pandit, L. Lin, S. Zhao, K. Flatt, V. Gruev, Y.-S. Chen, S. Nie, *ACS Appl. Mater. Interfaces* **2024**, *16*, 8554.
[179] C. G. Khoury, T. Vo-Dinh, *J. Phys. Chem. C* **2008**, *112*, 18849.
[180] S. A. Oh, J. W. Park, S. H. Kim, S. K. Kim, J. W. Yea, S. Y. Lee, H. C. Kang, *J. Korean Phys. Soc.* **2018**, *73*, 1744.
[181] M. Grzelczak, J. Pérez-Juste, P. Mulvaney, L. M. Liz-Marzán, *Chem. Soc. Rev.* **2008**, *37*, 1783.
[182] B. Pelaz, V. Grazu, A. Ibarra, C. Magen, P. Del Pino, J. M. De La Fuente, *Langmuir* **2012**, *28*, 8965.
[183] Q. He, S. Guo, Z. Qian, X. Chen, *Chem. Soc. Rev.* **2015**, *44*, 6258.
[184] E. Qiu, X. Chen, D.-P. Yang, M. D. Regulacio, R. M. C. R. Ramos, Z. Luo, Y.-L. Wu, M. Lin, Z. Li, X. J. Loh, E. Ye, *ACS Omega* **2022**, *7*, 2031.
[185] P. Huang, J. Lin, W. Li, P. Rong, Z. Wang, S. Wang, X. Wang, X. Sun, M. Aronova, G. Niu, R. D. Leapman, Z. Nie, X. Chen, *Angew. Chem.* **2013**, *125*, 14208.
[186] M. T. Reetz, W. Helbig, *J. Am. Chem. Soc.* **1994**, *116*, 7401.
[187] Y. Z. Song, X. Li, Y. Song, Z. P. Cheng, H. Zhong, J. M. Xu, J. S. Lu, C. G. Wei, A. F. Zhu, F. Y. Wu, J. Xu, *Russ. J. Phys. Chem. A* **2013**, *87*, 74.
[188] C.-J. Huang, P.-H. Chiu, Y.-H. Wang, K.-L. Chen, J.-J. Linn, C.-F. Yang, *J. Electrochem. Soc.* **2006**, *153*, D193.
[189] M. Haruta, M. Daté, *Appl. Catal. Gen.* **2001**, *222*, 427.
[190] S. Chen, Y. Yang, *J. Am. Chem. Soc.* **2002**, *124*, 5280.
[191] R. G. Freeman, K. C. Grabar, K. J. Allison, R. M. Bright, J. A. Davis, A. P. Guthrie, M. B. Hommer, M. A. Jackson, P. C. Smith, D. G. Walter, M. J. Natan, *Science* **1995**, *267*, 1629.
[192] K. Kuge, M. Arisawa, N. Aoki, A. Hasegawa, *Jpn. J. Appl. Phys.* **2000**, *39*, 6550.

[193] P. V. Kamat, M. Flumiani, G. V. Hartland, *J. Phys. Chem. B* **1998**, *102*, 3123.
[194] S. S. Shankar, A. Rai, A. Ahmad, M. Sastry, *J. Colloid Interface Sci.* **2004**, *275*, 496.
[195] J. L. Gardea-Torresdey, J. G. Parsons, E. Gomez, J. Peralta-Videa, H. E. Troiani, P. Santiago, M. J. Yacaman, *Nano Lett.* **2002**, *2*, 397.
[196] S. P. Chandran, M. Chaudhary, R. Pasricha, A. Ahmad, M. Sastry, *Biotechnol. Prog.* **2006**, *22*, 577.
[197] J. Huang, Q. Li, D. Sun, Y. Lu, Y. Su, X. Yang, H. Wang, Y. Wang, W. Shao, N. He, J. Hong, C. Chen, *Nanotechnology* **2007**, *18*, 105104.
[198] S. S. Shankar, A. Rai, B. Ankamwar, A. Singh, A. Ahmad, M. Sastry, *Nat. Mater.* **2004**, *3*, 482.
[199] K. B. Narayanan, N. Sakthivel, *Mater. Lett.* **2008**, *62*, 4588.
[200] B. Ankamwar, *E-J. Chem.* **2010**, *7*, 1334.
[201] K. Arunachalam, S. Annamalai, S. Hari, *Int. J. Nanomed.* **2013**, 1307.
[202] S. A. Aromal, V. K. Vidhu, D. Philip, *Spectrochim. Acta. A. Mol. Biomol. Spectrosc.* **2012**, *85*, 99.
[203] M. V. Sujitha, S. Kannan, *Spectrochim. Acta. A. Mol. Biomol. Spectrosc.* **2013**, *102*, 15.
[204] C. Tamuly, M. Hazarika, S. Ch. Borah, M. R. Das, M. P. Boruah, *Colloids Surf. B Biointerfaces* **2013**, *102*, 627.
[205] K. M. Kumar, B. K. Mandal, M. Sinha, V. Krishnakumar, *Spectrochim. Acta. A. Mol. Biomol. Spectrosc.* **2012**, *86*, 490.
[206] R. K. Das, N. Gogoi, U. Bora, *Bioprocess Biosyst. Eng.* **2011**, *34*, 615.
[207] D. Philip, C. Unni, S. A. Aromal, V. K. Vidhu, *Spectrochim. Acta. A. Mol. Biomol. Spectrosc.* **2011**, *78*, 899.
[208] D. Philip, *Spectrochim. Acta. A. Mol. Biomol. Spectrosc.* **2010**, *77*, 807.
[209] A. Bankar, B. Joshi, A. Ravi Kumar, S. Zinjarde, *Colloids Surf. B Biointerfaces* **2010**, *80*, 45.
[210] S. L. Smitha, D. Philip, K. G. Gopchandran, *Spectrochim. Acta. A. Mol. Biomol. Spectrosc.* **2009**, *74*, 735.
[211] V. T. P. Vinod, P. Saravanan, B. Sreedhar, D. K. Devi, R. B. Sashidhar, *Colloids Surf. B Biointerfaces* **2011**, *83*, 291.
[212] K. P. Kumar, W. Paul, C. P. Sharma, *Process Biochem.* **2011**, *46*, 2007.
[213] U. K. Parida, B. K. Bindhani, P. Nayak, *World J. Nano Sci. Eng.* **2011**, *01*, 93.
[214] A. Gouri, A. Sharma, M. Boddu, J. Mahendran, S. J. Mohanbhai, M. N. Sardoiwala, S. R. Choudhury, S. Karmakar, in *Multifunctional Nanocomposites for Targeted Drug Delivery in Cancer Therapy*, Elsevier, Cham **2024**, pp. 179–212.
[215] A. A. Bakal, A. A. Kozlova, A. S. Novoselova, I. Y. Goryacheva, in *Saratov Fall Meeting 2019: Optical and Nano-Technologies for Biology and Medicine*, SPIE, Bellingham, WA **2020**, pp. 236–241.
[216] N. Rajana, A. Mounika, P. S. Chary, V. Bhavana, A. Urati, D. Khatri, S. B. Singh, N. K. Mehra, *J. Controlled Release* **2022**, *352*, 1024.
[217] T. J. Ondera, A. T. Hamme II, *Analyst* **2015**, *140*, 7902.
[218] S. Vengurlekar, S. C. Chaturvedi, in *Nano Drug Delivery Strategies for the Treatment of Cancers*, Elsevier, Cham **2021**, pp. 107–118.
[219] J. L. Vivero-Escoto, R. C. Huxford-Phillips, W. Lin, *Chem. Soc. Rev.* **2012**, *41*, 2673.
[220] S. S. Khasraghi, A. Shojaei, U. Sundararaj, *Mater. Sci. Eng. C* **2020**, *114*, 110993.
[221] S. J. McMahon, F. J. Currell, in *Frontiers in Nanoscience*, Elsevier, Cham **2013**, pp. 65–93.
[222] I. Hocaoglu, D. Asik, G. Ulusoy, C. Grandfils, I. Ojea-Jimenez, F. Rossi, A. Kiraz, N. Doğan, H. Y. Acar, *Colloids Surf. B Biointerfaces* **2015**, *133*, 198.
[223] S. S. Nazeer, A. Saraswathy, N. Nimi, E. Sarathkumar, A. N. Resmi, S. J. Shenoy, R. S. Jayasree, *Methods Appl. Fluoresc.* **2023**, *11*, 024002.
[224] S. Kargozar, S. J. Hoseini, P. B. Milan, S. Hooshmand, H.-W. Kim, M. Mozafari, *Biotechnol. J.* **2020**, *15*, 2000117.
[225] G. Kandasamy, D. Maity, *Int. J. Pharm.* **2015**, *496*, 191.
[226] J. U. Menon, P. Jadeja, P. Tambe, K. Vu, B. Yuan, K. T. Nguyen, *Theranostics* **2013**, *3*, 152.
[227] Q. Gao, J. Zhang, J. Gao, Z. Zhang, H. Zhu, D. Wang, *Front. Bioeng. Biotechnol.* **2021**, *9*, 647905.
[228] A. Noureddine, A. Maestas-Olguin, E. A. Saada, A. E. LaBauve, J. O. Agola, K. E. Baty, T. Howard, J. K. Sabo, C. R. S. Espinoza, J. A. Doudna, J. S. Schoeniger, K. S. Butler, O. A. Negrete, C. J. Brinker, R. E. Serda, *Acta Biomater.* **2020**, *114*, 358.
[229] A. A. Kajani, L. Rafiee, S. H. Javanmard, N. Dana, S. Jandaghian, *RSC Adv.* **2023**, *13*, 9491.
[230] L. Wang, J. Lei, J. Zhang, *Chem. Commun.* **2009**, 2195.
[231] S. Vidawati, S. Barbosa, P. Taboada, E. Villar, A. Topete, V. Mosquera, *Adv. Biol. Chem.* **2018**, *08*, 91.
[232] S. P. Yeap, S. S. Leong, A. L. Ahmad, B. S. Ooi, J. Lim, *J. Phys. Chem. C* **2014**, *118*, 24042.
[233] A. Shavel, L. M. Liz-Marzán, *Phys. Chem. Chem. Phys.* **2009**, *11*, 3762.
[234] N. Gumbiowski, K. Loza, M. Heggen, M. Epple, *Nanoscale Adv.* **2023**, *5*, 2318.
[235] Y. Sun, Y. Xia, *Science* **2002**, *298*, 2176.
[236] J. D. Mangadlao, X. Wang, C. McCleese, M. Escamilla, G. Ramamurthy, Z. Wang, M. Govande, J. P. Basilion, C. Burda, *ACS Nano* **2018**, *12*, 3714.
[237] S.-Y. Sung, Y.-L. Su, W. Cheng, P.-F. Hu, C.-S. Chiang, W.-T. Chen, S.-H. Hu, *Nano Lett.* **2019**, *19*, 69.
[238] M. Haider, R. Cagliani, J. Jagal, M. N. Jayakumar, B. Fayed, S. B. Shakartalla, R. Pasricha, K. Greish, R. El-Awady, *J. Colloid Interface Sci.* **2023**, *630*, 698.
[239] S. Santra, H. Yang, P. H. Holloway, J. T. Stanley, R. A. Mericle, *J. Am. Chem. Soc.* **2005**, *127*, 1656.
[240] F. Zhan, C. Zhang, *J. Mater. Chem.* **2011**, *21*, 4765.
[241] H. Wang, Q. Mu, R. Revia, K. Wang, B. Tian, G. Lin, W. Lee, Y.-K. Hong, M. Zhang, *J. Controlled Release* **2018**, *289*, 70.
[242] M. E. Sommer, M. Elgeti, P. W. Hildebrand, M. Szczepek, K. P. Hofmann, P. Scheerer, in *Methods in Enzymology*, Elsevier, Cham **2015**, pp. 563–608.
[243] J. Zhu, Y. Shen, C. Yao, A. Xie, *Colloid J.* **2016**, *78*, 156.
[244] K. H. Leong, H. Y. Chu, S. Ibrahim, P. Saravanan, *Beilstein J. Nanotechnol.* **2015**, *6*, 428.
[245] J. Jiang, L.-H. Ai, L.-C. Li, H. Liu, *J. Alloys Compd.* **2009**, *484*, 69.
[246] K. Viswanathan, *Colloids Surf. Physicochem. Eng. Asp.* **2011**, *386*, 11.
[247] R. Kas, E. Sevinc, U. Topal, H. Y. Acar, *J. Phys. Chem. C* **2010**, *114*, 7758.
[248] Y. Nahar, M. A. Rahman, M. K. Hossain, M. K. Sharafat, M. R. Karim, A. Elaissari, B. Ochiai, H. Ahmad, M. M. Rahman, *Mater. Res. Express* **2019**, *7*, 016102.
[249] K. Wu, J. Liu, V. K. Chugh, S. Liang, R. Saha, V. D. Krishna, M. C. Cheeran, J.-P. Wang, *Nano Futur.* **2022**.
[250] K. Wu, D. Tonini, S. Liang, R. Saha, V. K. Chugh, J.-P. Wang, *ACS Appl. Mater. Interfaces* **2022**, *14*, 9945.
[251] A. K. Hauser, K. W. Anderson, J. Z. Hilt, *Nanomedicine* **2016**, *11*, 1769.
[252] T. Mai, J. Z. Hilt, *Colloids Surf. Physicochem. Eng. Asp.* **2019**, *576*, 9.
[253] M. R. Abedin, S. Umapathi, H. Mahendrakar, T. Laemthong, H. Coleman, D. Muchangi, S. Santra, M. Nath, S. Barua, *J. Nanobiotechnology* **2018**, *16*, 1.
[254] H. Arkaban, M. Barani, M. R. Akbarizadeh, N. Pal Singh Chauhan, S. Jadoun, M. Dehghani Soltani, P. Zarrintaj, *Polymers* **2022**, *14*, 1259.
[255] S. Savaskan Yilmaz, N. Yildirim, M. Misir, Y. Misirlioglu, E. Celik, *Materials* **2020**, *13*, 4390.
[256] L. M. Sanchez, D. A. Martin, V. A. Alvarez, J. S. Gonzalez, *Colloids Surf. Physicochem. Eng. Asp.* **2018**, *543*, 28.
[257] Y. Hu, X. Jiang, Y. Ding, H. Ge, Y. Yuan, C. Yang, *Biomaterials* **2002**, *23*, 3193.
[258] H. Jans, K. Jans, L. Lagae, G. Borghs, G. Maes, Q. Huo, *Nanotechnology* **2010**, *21*, 455702.

[259] L. Shao, R. Zhang, J. Lu, C. Zhao, X. Deng, Y. Wu, *ACS Appl. Mater. Interfaces* **2017**, *9*, 1226.
[260] Y. Fu, L. Yang, J. Zhang, J. Hu, G. Duan, X. Liu, Y. Li, Z. Gu, *Mater. Horiz.* **2021**, *8*, 1618.
[261] Y. Cheng, S. Zhang, N. Kang, J. Huang, X. Lv, K. Wen, S. Ye, Z. Chen, X. Zhou, L. Ren, *ACS Appl. Mater. Interfaces* **2017**, *9*, 19296.
[262] S. Liu, L. Wang, M. Lin, D. Wang, Z. Song, S. Li, R. Ge, X. Zhang, Y. Liu, Z. Li, *ACS Appl. Mater. Interfaces* **2017**, *9*, 44293.
[263] B. Poinard, S. Kamaluddin, A. Q. Q. Tan, K. G. Neoh, J. C. Y. Kah, *ACS Appl. Mater. Interfaces* **2019**, *11*, 4777.
[264] I. I. Niyonshuti, V. R. Krishnamurthi, D. Okyere, L. Song, M. Benamara, X. Tong, Y. Wang, J. Chen, *ACS Appl. Mater. Interfaces* **2020**, *12*, 40067.
[265] M. Zheng, M. Pan, W. Zhang, H. Lin, S. Wu, C. Lu, S. Tang, D. Liu, J. Cai, *Bioact. Mater.* **2021**, *6*, 1878.
[266] W. X. Siow, Y.-T. Chang, M. Babič, Y.-C. Lu, D. Horák, Y.-H. Ma, *Int. J. Nanomed.* **2018**, 1693.
[267] E. Alinejad-Mofrad, B. Malaekeh-Nikouei, L. Gholami, S. H. Mousavi, H. R. Sadeghnia, M. Mohajeri, M. Darroudi, R. K. Oskuee, *Hum. Exp. Toxicol.* **2019**, *38*, 983.
[268] R. G. Thomas, M. Muthiah, M. Moon, I.-K. Park, Y. Y. Jeong, *Macromol. Res.* **2017**, *25*, 446.
[269] C. Wang, F. Tang, X. Wang, L. Li, *ACS Appl. Mater. Interfaces* **2015**, *7*, 13653.
[270] C. Wang, F. Tang, X. Wang, L. Li, *Colloids Surf. Physicochem. Eng. Asp.* **2016**, *506*, 425.
[271] W. Ahmed, Z. Zhai, C. Gao, *Mater. Today Bio* **2019**, *2*, 100017.
[272] H. Zhu, R. Liu, Y. Shang, L. Sun, *Eng. Regen.* **2023**, *4*, 20.
[273] S. Zheng, Y. Guan, H. Yu, G. Huang, C. Zheng, *New J. Chem.* **2019**, *43*, 9989.
[274] T. Kim, H. S. Han, K. Yang, Y. M. Kim, K. Nam, K. H. Park, S. Y. Choi, H. W. Park, K. Y. Choi, Y. H. Roh, *ACS Nano* **2024**, *18*, 7972.
[275] K. A. Howard, *Adv. Drug Delivery Rev.* **2009**, *61*, 710.
[276] A. A. D'souza, R. Shegokar, *Expert Opin. Drug Deliv.* **2016**, *13*, 1257.
[277] K. Mylkie, P. Nowak, P. Rybczynski, M. Ziegler-Borowska, *Materials* **2021**, *14*, 248.
[278] L. Shi, J. Zhang, M. Zhao, S. Tang, X. Cheng, W. Zhang, W. Li, X. Liu, H. Peng, Q. Wang, *Nanoscale* **2021**, *13*, 10748.
[279] J. S. Suk, Q. Xu, N. Kim, J. Hanes, L. M. Ensign, *Adv. Drug Delivery Rev.* **2016**, *99*, 28.
[280] J. C. Love, L. A. Estroff, J. K. Kriebel, R. G. Nuzzo, G. M. Whitesides, *Chem. Rev.* **2005**, *105*, 1103.
[281] I. H. El-Sayed, X. Huang, M. A. El-Sayed, *Nano Lett.* **2005**, *5*, 829.
[282] D. Pissuwan, S. M. Valenzuela, M. B. Cortie, *Biotechnol. Genet. Eng. Rev.* **2008**, *25*, 93.
[283] D. Liu, W. Chen, Y. Tian, S. He, W. Zheng, J. Sun, Z. Wang, X. Jiang, *Adv. Healthcare Mater.* **2012**, *1*, 90.
[284] G. Schneider, G. Decher, N. Nerambourg, R. Praho, M. H. V. Werts, M. Blanchard-Desce, *Nano Lett.* **2006**, *6*, 530.
[285] B.-S. Kong, J. Geng, H.-T. Jung, *Chem. Commun.* **2009**, 2174.
[286] A. Elbakry, A. Zaky, R. Liebl, R. Rachel, A. Goepferich, M. Breunig, *Nano Lett.* **2009**, *9*, 2059.
[287] Z. Wang, Q. Ye, S. Yu, B. Akhavan, *Adv. Healthcare Mater.* **2023**, *12*, 2300105.
[288] J. Yang, X. Jing, Z. Wang, X. Liu, X. Zhu, T. Lei, X. Li, W. Guo, H. Rao, M. Chen, K. Luan, X. Sui, Y. Wei, S. Liu, Q. Guo, *Front. Bioeng. Biotechnol.* **2021**, *9*, 607709.
[289] D. Shi, D. Beasock, A. Fessler, J. Szebeni, J. Y. Ljubimova, K. A. Afonin, M. A. Dobrovolskaia, *Adv. Drug Delivery Rev.* **2022**, *180*, 114079.
[290] S. Xiao, X. Yu, L. Zhang, Y. Zhang, W. Fan, T. Sun, C. Zhou, Y. Liu, Y. Liu, M. Gong, D. Zhang, *Int. J. Nanomed.* **2019**, *14*, 8499.
[291] G. Singh, T. Kaur, R. Kaur, A. Kaur, *Int J Pharmacol Pharm Sci* **2014**, *1*, 30.
[292] M. A. Sevostyanov, A. S. Baikin, K. V. Sergienko, L. A. Shatova, A. A. Kirsankin, I. V. Baymler, A. V. Shkirin, S. V. Gudkov, *React. Funct. Polym.* **2020**, *150*, 104550.
[293] P. Gentile, V. Chiono, I. Carmagnola, P. Hatton, *Int. J. Mol. Sci.* **2014**, *15*, 3640.
[294] R. P. F. Lanao, A. M. Jonker, J. G. C. Wolke, J. A. Jansen, J. C. M. Van Hest, S. C. G. Leeuwenburgh, *Tissue Eng. Part B Rev.* **2013**, *19*, 380.
[295] N. Ben Halima, *RSC Adv.* **2016**, *6*, 39823.
[296] D. J. Hines, D. L. Kaplan, *Crit. Rev. Ther. Drug Carrier Syst.* **2013**, *30*, 257.
[297] M. Mir, N. Ahmed, A. U. Rehman, *Colloids Surf. B Biointerfaces* **2017**, *159*, 217.
[298] S. Wohlfart, A. S. Khalansky, S. Gelperina, O. Maksimenko, C. Bernreuther, M. Glatzel, J. Kreuter, *PLoS One* **2011**, *6*, e19121.
[299] Y. Choi, H. Y. Yoon, J. Kim, S. Yang, J. Lee, J. W. Choi, Y. Moon, J. Kim, S. Lim, M. K. Shim, S. Jeon, I. C. Kwon, K. Kim, *Pharmaceutics* **2020**, *12*, 1165.
[300] S. Rezvantalab, N. I. Drude, M. K. Moraveji, N. Güvener, E. K. Koons, Y. Shi, T. Lammers, F. Kiessling, *Front. Pharmacol.* **2018**, *9*, 1260.
[301] T. Hickey, D. Kreutzer, D. J. Burgess, F. Moussy, *Biomaterials* **2002**, *23*, 1649.
[302] Y. Ling, K. Wei, F. Zou, S. Zhong, *Int. J. Pharm.* **2012**, *430*, 266.
[303] C. C. DeMerlis, D. R. Schoneker, *Food Chem. Toxicol.* **2003**, *41*, 319.
[304] M. I. Baker, S. P. Walsh, Z. Schwartz, B. D. Boyan, *J. Biomed. Mater. Res. B Appl. Biomater.* **2012**, *100B*, 1451.
[305] B. Gajra, S. S. Pandya, G. Vidyasagar, H. Rabari, R. R. Dedania, S. Rao, *Int J Pharm Res* **2012**, *4*, 2026.
[306] Y. Luo, G. Luo, M. Gelinsky, P. Huang, C. Ruan, *Mater. Lett.* **2017**, *189*, 295.
[307] X. Qin, X. Wang, M. Rottmar, B. J. Nelson, K. Maniura-Weber, *Adv. Mater.* **2018**, *30*, 1705564.
[308] K. G. Nathan, K. Genasan, T. Kamarul, *Mar. Drugs* **2023**, *21*, 304.
[309] M. S. A. Darwish, L. M. Al-Harbi, A. Bakry, *J. Therm. Anal. Calorim.* **2022**, *147*, 11921.
[310] M. Moffitt, K. Khougaz, A. Eisenberg, *Acc. Chem. Res.* **1996**, *29*, 95.
[311] C. Allen, D. Maysinger, A. Eisenberg, *Colloids Surf. B Biointerfaces* **1999**, *16*, 3.
[312] K. Kataoka, A. Harada, Y. Nagasaki, *Adv. Drug Delivery Rev.* **2012**, *64*, 37.
[313] E. Y. Kramarenko, I. I. Potemkin, A. R. Khokhlov, R. G. Winkler, P. Reineker, *Macromolecules* **1999**, *32*, 3495.
[314] Z. Zhu, *Biomaterials* **2013**, *34*, 10238.
[315] B. Jeong, Y. Han Bae, S. Wan Kim, *Colloids Surf. B Biointerfaces* **1999**, *16*, 185.
[316] H. S. Yoo, T. G. Park, *J. Controlled Release* **2001**, *70*, 63.
[317] P. Y. Li, F. Bearoff, P. Zhu, Z. Fan, Y. Zhu, M. Fan, L. Cort, T. Kambayashi, E. P. Blankenhorn, H. Cheng, *J. Controlled Release* **2021**, *331*, 164.
[318] A. Eskandari, K. Suntharalingam, *Chem. Sci.* **2019**, *10*, 7792.
[319] Y. Chen, N. Li, B. Xu, M. Wu, X. Yan, L. Zhong, H. Cai, T. Wang, Q. Wang, F. Long, G. Jiang, H. Xiao, *Biomed. Pharmacother.* **2019**, *118*, 109257.
[320] D.-L. Fang, Y. Chen, B. Xu, K. Ren, Z.-Y. He, L.-L. He, Y. Lei, C.-M. Fan, X.-R. Song, *Int. J. Mol. Sci.* **2014**, *15*, 3373.
[321] Q. Yang, J. Zhao, A. Muhammad, L. Tian, Y. Liu, L. Chen, P. Yang, *Mater. Today Bio* **2022**, *16*, 100407.
[322] M. Puertas-Bartolomé, A. Mora-Boza, L. García-Fernández, *Polymers* **2021**, *13*, 1209.
[323] M. Zahran, A. H. Marei, *Int. J. Biol. Macromol.* **2019**, *136*, 586.
[324] H. Arami, Z. Stephen, O. Veiseh, M. Zhang, in *Chitosan for Biomaterials I*, (Eds.: R. Jayakumar, M. Prabaharan, R. A. A. Muzzarelli), Springer Berlin Heidelberg, Berlin, Heidelberg **2011**, pp. 163–184.
[325] L. A. Frank, G. R. Onzi, A. S. Morawski, A. R. Pohlmann, S. S. Guterres, R. V. Contri, *React. Funct. Polym.* **2020**, *147*, 104459.

[326] M. H. Elkomy, A. A. Ali, H. M. Eid, *J. Controlled Release* **2022**, *351*, 923.
[327] X. N. Pham, T. P. Nguyen, T. N. Pham, T. T. N. Tran, T. V. T. Tran, *Adv. Nat. Sci. Nanosci. Nanotechnol.* **2016**, *7*, 045010.
[328] D. R. Bhumkar, H. M. Joshi, M. Sastry, V. B. Pokharkar, *Pharm. Res.* **2007**, *24*, 1415.
[329] X. Jiang, Z. Du, X. Zhang, F. Zaman, Z. Song, Y. Guan, T. Yu, Y. Huang, *Front. Bioeng. Biotechnol.* **2023**, *11*, 1158749.
[330] S. Suarasan, M. Focsan, M. Potara, O. Soritau, A. Florea, D. Maniu, S. Astilean, *ACS Appl. Mater. Interfaces* **2016**, *8*, 22900.
[331] B. Gaihre, M. Khil, D. Lee, H. Kim, *Int. J. Pharm.* **2009**, *365*, 180.
[332] D. Dehaini, R. H. Fang, L. Zhang, *Bioeng. Transl. Med.* **2016**, *1*, 30.
[333] N. A. Peppas, *Adv. Drug Delivery Rev.* **2004**, *56*, 1529.
[334] J.-W. Yoo, D. J. Irvine, D. E. Discher, S. Mitragotri, *Nat. Rev. Drug Discovery* **2011**, *10*, 521.
[335] C. J. Hu, R. H. Fang, L. Zhang, *Adv. Healthcare Mater.* **2012**, *1*, 537.
[336] R. H. Fang, C.-M. J. Hu, L. Zhang, *Expert Opin. Biol. Ther.* **2012**, *12*, 385.
[337] R. H. Fang, A. V. Kroll, W. Gao, L. Zhang, *Adv. Mater.* **2018**, *30*, 1706759.
[338] Q. Hu, W. Sun, C. Qian, C. Wang, H. N. Bomba, Z. Gu, *Adv. Mater.* **2015**, *27*, 7043.
[339] R. Yang, J. Xu, L. Xu, X. Sun, Q. Chen, Y. Zhao, R. Peng, Z. Liu, *ACS Nano* **2018**, *12*, 5121.
[340] B. Yu, S. Goel, D. Ni, P. A. Ellison, C. M. Siamof, D. Jiang, L. Cheng, L. Kang, F. Yu, Z. Liu, T. E. Barnhart, Q. He, H. Zhang, W. Cai, *Adv. Mater.* **2018**, *30*, 1704934.
[341] R. H. Fang, Y. Jiang, J. C. Fang, L. Zhang, *Biomaterials* **2017**, *128*, 69.
[342] V. Kozlovskaya, J. F. Alexander, Y. Wang, T. Kuncewicz, X. Liu, B. Godin, E. Kharlampieva, *ACS Nano* **2014**, *8*, 5725.
[343] C.-M. J. Hu, L. Zhang, S. Aryal, C. Cheung, R. H. Fang, L. Zhang, *Proc. Natl. Acad. Sci.* **2011**, *108*, 10980.
[344] E. Ben-Akiva, R. A. Meyer, H. Yu, J. T. Smith, D. M. Pardoll, J. J. Green, *Sci. Adv.* **2020**, *6*, eaay9035.
[345] G. Deng, X. Peng, Z. Sun, W. Zheng, J. Yu, L. Du, H. Chen, P. Gong, P. Zhang, L. Cai, B. Z. Tang, *ACS Nano* **2020**, *14*, 11452.
[346] H.-H. Wu, Y. Zhou, Y. Tabata, J.-Q. Gao, *J. Controlled Release* **2019**, *294*, 102.
[347] K. Simons, W. L. C. Vaz, *Annu. Rev. Biophys. Biomol. Struct.* **2004**, *33*, 269.
[348] Y. Zhai, J. Su, W. Ran, P. Zhang, Q. Yin, Z. Zhang, H. Yu, Y. Li, *Theranostics* **2017**, *7*, 2575.
[349] Z. Fan, P. Y. Li, J. Deng, S. C. Bady, H. Cheng, *Nano Res.* **2018**, *11*, 5573.
[350] A. Parodi, N. Quattrocchi, A. L. van de Ven, C. Chiappini, M. Evangelopoulos, J. O. Martinez, B. S. Brown, S. Z. Khaled, I. K. Yazdi, M. V. Enzo, L. Isenhart, M. Ferrari, E. Tasciotti, *Nat. Nanotechnol.* **2013**, *8*, 61.
[351] L. Rao, Q. Meng, Q. Huang, P. Liu, L. Bu, K. K. Kondamareddy, S. Guo, W. Liu, X. Zhao, *Adv. Healthcare Mater.* **2016**, *5*, 1420.
[352] J. Su, H. Sun, Q. Meng, P. Zhang, Q. Yin, Y. Li, *Theranostics* **2017**, *7*, 523.
[353] Q. Xu, J. Wan, N. Bie, X. Song, X. Yang, T. Yong, Y. Zhao, X. Yang, L. Gan, *Theranostics* **2018**, *8*, 5362.
[354] X. Ren, R. Zheng, X. Fang, X. Wang, X. Zhang, W. Yang, X. Sha, *Biomaterials* **2016**, *92*, 13.
[355] L. Rao, Q.-F. Meng, L.-L. Bu, B. Cai, Q. Huang, Z.-J. Sun, W.-F. Zhang, A. Li, S.-S. Guo, W. Liu, T.-H. Wang, X.-Z. Zhao, *ACS Appl. Mater. Interfaces* **2017**, *9*, 2159.
[356] W.-L. Liu, M.-Z. Zou, T. Liu, J.-Y. Zeng, X. Li, W.-Y Yu, C.-X. Li, J.-J. Ye, W. Song, J. Feng, X.-Z. Zhang, *Adv. Mater.* **2019**, *31*, 1900499.
[357] D. Dehaini, X. Wei, R. H. Fang, S. Masson, P. Angsantikul, B. T. Luk, Y. Zhang, M. Ying, Y. Jiang, A. V. Kroll, W. Gao, L. Zhang, *Adv. Mater.* **2017**, *29*, 1606209.
[358] M. Mathiyazhakan, C. Wiraja, C. Xu, *Nano-Micro Lett.* **2018**, *10*, 10.
[359] Z. Chai, D. Ran, L. Lu, C. Zhan, H. Ruan, X. Hu, C. Xie, K. Jiang, J. Li, J. Zhou, J. Wang, Y. Zhang, R. H. Fang, L. Zhang, W. Lu, *ACS Nano* **2019**, *13*, 5591.
[360] W. He, J. Frueh, Z. Wu, Q. He, *Langmuir* **2016**, *32*, 3637.
[361] L. Rao, B. Cai, L.-L. Bu, Q.-Q. Liao, S.-S. Guo, X.-Z. Zhao, W.-F. Dong, W. Liu, *ACS Nano* **2017**, *11*, 3496.
[362] I. Srivastava, B. Lew, Y. Wang, S. Blair, M. B. George, B. S. Hajek, S. Bangru, S. Pandit, Z. Wang, J. Ludwig, K. Flatt, M. Gruebele, S. Nie, V. Gruev, *ACS Nano* **2023**, *17*, 8465.
[363] K. Chatterjee, S. Sarkar, K. Jagajjanani Rao, S. Paria, *Adv. Colloid Interface Sci.* **2014**, *209*, 8.
[364] B. Doan, S. Meme, J. Beloeil, in *The Chemistry of Contrast Agents in Medical Magnetic Resonance Imaging*, (Eds: A. Merbach, L. Helm, É. Tóth), Wiley, Hoboken, NJ **2013**, pp. 1–23.
[365] H. A. Sharma, *Acta Neuropsychiatr.* **2009**, *21*, 200.
[366] J. G. Pipe, *Magn. Reson. Imaging Clin. N. Am.* **1999**, *7*, 607.
[367] S. D. Serai, *Pediatr. Radiol.* **2022**, *52*, 217.
[368] M. B. Gawande, A. Goswami, T. Asefa, H. Guo, A. V. Biradar, D.-L. Peng, R. Zboril, R. S. Varma, *Chem. Soc. Rev.* **2015**, *44*, 7540.
[369] S. Caspani, R. Magalhães, J. P. Araújo, C. T. Sousa, *Materials* **2020**, *13*, 2586.
[370] G. J. Strijkers, W. J. M. Mulder, G. A. F. Van Tilborg, K. Nicolay, *Anticancer Agents Med. Chem.* **2007**, *7*, 291.
[371] L. M. Ali, P. Marzola, E. Nicolato, S. Fiorini, M. D. L. Heras Guillamón, R. Piñol, L. Gabilondo, A. Millán, F. Palacio, *Future Sci. OA* **2019**, *5*, FSO235.
[372] D. Liu, J. Li, C. Wang, L. An, J. Lin, Q. Tian, S. Yang, *Nanomedicine Nanotechnol. Biol. Med.* **2021**, *32*, 102335.
[373] Y. Luengo Morato, M. Marciello, L. Lozano Chamizo, K. Ovejero Paredes, M. Filice, in *Magnetic Nanoparticle-Based Hybrid Materials*, Elsevier, Cham **2021**, pp. 343–386.
[374] M. A. Busquets, J. Estelrich, M. J. Sánchez-Martín, *Int. J. Nanomed.* **2015**, 1727.
[375] M. Nedyalkova, B. Donkova, J. Romanova, G. Tzvetkov, S. Madurga, V. Simeonov, *Adv. Colloid Interface Sci.* **2017**, *249*, 192.
[376] A. Chicheł, J. Skowronek, M. Kubaszewska, M. Kanikowski, *Rep. Pract. Oncol. Radiother.* **2007**, *12*, 267.
[377] P. Kaur, M. D. Hurwitz, S. Krishnan, A. Asea, *Cancers* **2011**, *3*, 3799.
[378] I. M. Obaidat, V. Narayanaswamy, S. Alaabed, S. Sambasivam, C. V. V. Muralee Gopi, *Magnetochemistry* **2019**, *5*, 67.
[379] S. Dutz, R. Hergt, *Int. J. Hyperthermia* **2013**, *29*, 790.
[380] L. Yu, J. Liu, K. Wu, T. Klein, Y. Jiang, J.-P. Wang, *Sci. Rep.* **2014**, *4*, 7216.
[381] A. E. Deatsch, B. A. Evans, *J. Magn. Magn. Mater.* **2014**, *354*, 163.
[382] K. Wu, J.-P. Wang, *AIP Adv.* **2017**, *7*, 056327.
[383] H. Fatima, T. Charinpanitkul, K.-S. Kim, *Nanomaterials* **2021**, *11*, 1203.
[384] A. Majid, W. Ahmed, Y. Patil-Sen, T. Sen, in *Micro Nanomanufacturing*, Vol. *II* (Eds.: M. J. Jackson, W. Ahmed), Springer International Publishing, Cham, **2018**, pp. 413–442.
[385] J. Jose, R. Kumar, S. Harilal, G. E. Mathew, D. G. T. Parambi, A. Prabhu, Md. S. Uddin, L. Aleya, H. Kim, B. Mathew, *Environ. Sci. Pollut. Res.* **2020**, *27*, 19214.
[386] K. Wu, J. Liu, Y. Wang, C. Ye, Y. Feng, J.-P. Wang, *Appl. Phys. Lett.* **2015**, *107*, 053701.
[387] K. Wu, L. Tu, D. Su, J.-P. Wang, *J. Phys. Appl. Phys.* **2017**, *50*, 085005.
[388] X. L. Liu, Y. Yang, C. T. Ng, L. Y. Zhao, Y. Zhang, B. H. Bay, H. M. Fan, J. Ding, *Adv. Mater.* **2015**, *27*, 1939.
[389] P. Liu, P. Jonkheijm, L. W. Terstappen, M. Stevens, *Cancers* **2020**, *12*, 3525.
[390] O. Lara, X. Tong, M. Zborowski, J. J. Chalmers, *Exp. Hematol.* **2004**, *32*, 891.
[391] H. Chen, Y. Li, Z. Zhang, S. Wang, *Biomicrofluidics* **2020**, 14.

[392] D. Lin, L. Shen, M. Luo, K. Zhang, J. Li, Q. Yang, F. Zhu, D. Zhou, S. Zheng, Y. Chen, *Signal Transduct. Target. Ther.* **2021**, *6*, 404.
[393] A. S. Zamay, G. S. Zamay, O. S. Kolovskaya, T. N. Zamay, M. V. Berezovski, *Isol. Mol. Charact. Circ. Tumor Cells* **2017**, 67.
[394] L. Luo, Y. He, *Cancer Med.* **2020**, *9*, 4207.
[395] U. Das, S. Banik, S. S. Nadumane, S. Chakrabarti, D. Gopal, S. P. Kabekkodu, P. Srisungsitthisunti, N. Mazumder, R. Biswas, *Pharmaceutics* **2023**, *15*, 280.
[396] Q. Ge, J. Su, T.-S. Chung, G. Amy, *Ind. Eng. Chem. Res.* **2011**, *50*, 382.
[397] Y. Ma, X. Zhang, T. Zeng, D. Cao, Z. Zhou, W. Li, H. Niu, Y. Cai, *ACS Appl. Mater. Interfaces* **2013**, *5*, 1024.
[398] P. A. Rose, P. K. Praseetha, M. Bhagat, P. Alexander, S. Abdeen, M. Chavali, *Technol. Cancer Res. Treat.* **2013**, *12*, 463.
[399] L. E. Puluhulawa, I. M. Joni, K. M. Elamin, A. F. A. Mohammed, M. Muchtaridi, N. Wathoni, *Polymers* **2022**, *14*, 3410.
[400] S. Iravani, R. S. Varma, *Mar. Drugs* **2022**, *20*, 598.
[401] J. Liu, N. Zhang, J. Wu, P. Dong, H. Lv, Q. Wang, S. Wang, H. Yang, S. Wang, X. Li, *Int. J. Nanomed.* **2022**, 4895.
[402] Z. Wang, Z. Wu, N. Sun, Y. Cao, X. Cai, F. Yuan, H. Zou, C. Xing, R. Pei, *J. Mater. Chem. B* **2021**, *9*, 677.
[403] C. Pipatwatcharadate, P. R. Iyer, D. Pissuwan, *Pharmaceutics* **2023**, *15*, 2482.
[404] P. I. Nikitin, P. M. Vetoshko, T. I. Ksenevich, *J. Magn. Magn. Mater.* **2007**, *311*, 445.
[405] H.-J. Krause, N. Wolters, Y. Zhang, A. Offenhäusser, P. Miethe, M. H. Meyer, M. Hartmann, M. Keusgen, *J. Magn. Magn. Mater.* **2007**, *311*, 436.
[406] V. K. Chugh, K. Wu, V. D. Krishna, A. di Girolamo, R. P. Bloom, Y. A. Wang, R. Saha, S. Liang, M. C. Cheeran, J.-P. Wang, *J. Phys. Chem. C* **2021**, *125*, 17221.
[407] K. Wu, D. Su, R. Saha, J. Liu, V. K. Chugh, J.-P. Wang, *ACS Appl. Nano Mater.* **2020**, *3*, 4972.
[408] T. Q. Bui, W. L. Tew, S. I. Woods, *J. Appl. Phys.* **2020**, *128*, 224901.
[409] X. Zhang, D. B. Reeves, I. M. Perreard, W. C. Kett, K. E. Griswold, B. Gimi, J. B. Weaver, *Biosens. Bioelectron.* **2013**, *50*, 441.
[410] K. Wu, V. K. Chugh, V. D. Krishna, A. di Girolamo, Y. A. Wang, R. Saha, S. Liang, M. C. Cheeran, J.-P. Wang, *ACS Appl. Mater. Interfaces* **2021**, *13*, 44136.
[411] A. V. Orlov, J. A. Khodakova, M. P. Nikitin, A. O. Shepelyakovskaya, F. A. Brovko, A. G. Laman, E. V. Grishin, P. I. Nikitin, *Anal. Chem.* **2013**, *85*, 1154.
[412] A. V. Orlov, S. L. Znoyko, V. R. Cherkasov, M. P. Nikitin, P. I. Nikitin, *Anal. Chem.* **2016**, *88*, 10419.
[413] S. Horvat, P. Vogel, T. Kampf, A. Brandl, A. Alshamsan, H. A. Alhadlaq, M. Ahamed, K. Albrecht, V. C. Behr, A. Beilhack, *ChemNanoMat* **2020**, *6*, 755.
[414] K. Wu, V. K. Chugh, V. D. Krishna, Y. A. Wang, T. D. Gordon, M. C.-J. Cheeran, J.-P. Wang, *ACS Appl. Nano Mater.* **2022**.
[415] V. Chugh, S. Liang, P. Yari, K. Wu, J.-P. Wang, *J. Phys. Appl. Phys.* **2023**, *56*, 315001.
[416] K. Wu, J. Liu, R. Saha, D. Su, V. D. Krishna, M. C.-J. Cheeran, J.-P. Wang, *ACS Appl. Mater. Interfaces* **2020**, *12*, 13686.
[417] K. Wu, J. Liu, D. Su, R. Saha, J.-P. Wang, *ACS Appl. Mater. Interfaces* **2019**, *11*, 22979.
[418] J. Zhong, E. L. Rösch, T. Viereck, M. Schilling, F. Ludwig, *ACS Sens.* **2021**, *6*, 976.
[419] Y. Liu, W. Wu, Y. Wang, S. Han, Y. Yuan, J. Huang, X. Shuai, Z. Peng, *Biomater. Sci.* **2021**, *9*, 6673.
[420] J. S. Lee, J. Kim, Y. Ye, T. Kim, *Adv. Drug Delivery Rev.* **2022**, *186*, 114339.
[421] J. Liu, J. Shi, W. Nie, S. Wang, G. Liu, K. Cai, *Adv. Healthcare Mater.* **2021**, *10*, 2001207.
[422] X. Song, C. Liu, N. Wang, H. Huang, S. He, C. Gong, Y. Wei, *Adv. Drug Delivery Rev.* **2021**, *168*, 158.
[423] X. Yang, X. Liu, Z. Liu, F. Pu, J. Ren, X. Qu, *Adv. Mater.* **2012**, *24*, 2890.
[424] B. C. Wilson, M. S. Patterson, *Phys. Med. Biol.* **2008**, *53*, R61.
[425] J. Wang, J. Qiu, *Cancer Res Front* **2016**, *2*, 67.
[426] J. Zhou, Z. Lu, X. Zhu, X. Wang, Y. Liao, Z. Ma, F. Li, *Biomaterials* **2013**, *34*, 9584.
[427] S. B. Aboeleneen, M. A. Scully, J. C. Harris, E. H. Sterin, E. S. Day, *Nano Converg.* **2022**, *9*, 1.
[428] J. Yang, J. Choi, D. Bang, E. Kim, E.-K. Lim, H. Park, J.-S. Suh, K. Lee, K.-H. Yoo, E.-K. Kim, *Angew Chem Int Ed* **2011**, *50*, 441.
[429] V. Ball, *Front. Bioeng. Biotechnol.* **2018**, *6*, 109.
[430] Y. Liu, K. Ai, J. Liu, M. Deng, Y. He, L. Lu, *Adv. Mater.* **2013**, *25*, 1353.
[431] S. Singh, S. B. Nimse, D. E. Mathew, A. Dhimmar, H. Sahastrabudhe, A. Gajjar, V. A. Ghadge, P. Kumar, P. B. Shinde, *Biotechnol. Adv.* **2021**, *53*, 107773.
[432] L.-S. Lin, Z.-X. Cong, J.-B. Cao, K.-M. Ke, Q.-L. Peng, J. Gao, H.-H. Yang, G. Liu, X. Chen, *ACS Nano* **2014**, *8*, 3876.
[433] K. C. Black, J. Yi, J. G. Rivera, D. C. Zelasko-Leon, P. B. Messersmith, *Nanomed.* **2013**, *8*, 17.
[434] S. Hong, K. Y. Kim, H. J. Wook, S. Y. Park, K. D. Lee, D. Y. Lee, H. Lee, *Nanomed.* **2011**, *6*, 793.
[435] H. Tian, C. Deng, H. Lin, J. Sun, M. Deng, X. Chen, X. Jing, *Biomaterials* **2005**, *26*, 4209.
[436] K. Knop, R. Hoogenboom, D. Fischer, U. S. Schubert, *Angew. Chem., Int. Ed.* **2010**, *49*, 6288.
[437] O. S. Kolovskaya, T. N. Zamay, G. S. Zamay, V. A. Babkin, E. N. Medvedeva, N. A. Neverova, A. K. Kirichenko, S. S. Zamay, I. N. Lapin, E. V. Morozov, A. E. Sokolov, A. A. Narodov, D. G. Fedorov, F. N. Tomilin, V. N. Zabluda, Y. Alekhina, K. A. Lukyanenko, Y. E. Glazyrin, V. A. Svetlichnyi, M. V. Berezovski, A. S. Kichkailo, *Cancers* **2020**, *12*, 216.
[438] F. Zhan, W. Chen, Z. Wang, W. Lu, R. Cheng, C. Deng, F. Meng, H. Liu, Z. Zhong, *Biomacromolecules* **2011**, *12*, 3612.
[439] J. Xia, H. Tian, J. Chen, Z. Guo, L. Lin, H. Yang, Z. Feng, *Chin. J. Polym. Sci.* **2016**, *34*, 316.
[440] E. Larrea, C. Sole, L. Manterola, I. Goicoechea, M. Armesto, M. Arestin, M. Caffarel, A. Araujo, M. Araiz, M. Fernandez-Mercado, C. Lawrie, *Int. J. Mol. Sci.* **2016**, *17*, 627.
[441] M. Prabaharan, J. J. Grailer, S. Pilla, D. A. Steeber, S. Gong, *Biomaterials* **2009**, *30*, 6065.
[442] L. Luo, H. He, C. Li, Y. He, Z. Hao, S. Wang, Q. Zhao, Z. Liu, D. Gao, *ACS Biomater. Sci. Eng.* **2019**, *5*, 1321.
[443] H. Xiong, X. Li, P. Kang, J. Perish, F. Neuhaus, J. E. Ploski, S. Kroener, M. O. Ogunyankin, J. E. Shin, J. A. Zasadzinski, H. Wang, P. A. Slesinger, A. Zumbuehl, Z. Qin, *Angew. Chem., Int. Ed.* **2020**, *59*, 8608.
[444] F. Wang, Y.-C. Wang, S. Dou, M.-H. Xiong, T.-M. Sun, J. Wang, *ACS Nano* **2011**, *5*, 3679.
[445] P. Kaur, M. L. Aliru, A. S. Chadha, A. Asea, S. Krishnan, *Int. J. Hyperthermia* **2016**, *32*, 76.
[446] R. Hong, G. Han, J. M. Fernández, B. Kim, N. S. Forbes, V. M. Rotello, *J. Am. Chem. Soc.* **2006**, *128*, 1078.
[447] X. Liu, M. T. Swihart, *Chem. Soc. Rev.* **2014**, *43*, 3908.
[448] M. S. Yavuz, Y. Cheng, J. Chen, C. M. Cobley, Q. Zhang, M. Rycenga, J. Xie, C. Kim, K. H. Song, A. G. Schwartz, L. V. Wang, Y. Xia, *Nat. Mater.* **2009**, *8*, 935.
[449] R. M. Fratila, S. Rivera-Fernández, J. M. De La Fuente, *Nanoscale* **2015**, *7*, 8233.
[450] R. Agarwal, P. Jurney, M. Raythatha, V. Singh, S. V. Sreenivasan, L. Shi, K. Roy, *Adv. Healthcare Mater.* **2015**, *4*, 2269.
[451] I. Srivastava, P. Moitra, M. Fayyaz, S. Pandit, T. L. Kampert, P. Fathi, H. R. Alanagh, K. Dighe, M. Alafeef, K. Vuong, M. Jabeen, S. Nie, J. Irudayaraj, D. Pan, *ACS Appl. Mater. Interfaces* **2021**, *13*, 59747.
[452] J. Senior, G. Gregoriadis, *FEBS Lett.* **1982**, *145*, 109.

**Bahareh Rezaei** attained her M.Sc. in materials engineering from Isfahan University of Technology, Iran (2018). Currently, she is a Ph.D. candidate at Texas Tech University, also serving as a research assistant in the Department of Electrical and Computer Engineering. Her scholarly pursuits center on the synthesis and characterization of magnetic nanoparticles for biomedical purposes, encompassing magnetic particle imaging (MPI), magnetic resonance imaging (MRI) contrast agents, and hyperthermia treatment for cancer.

**Asma Harun** is an international student from Bangladesh who is doing her Ph.D. in the Mechanical Engineering Department, at Texas Tech University. She did her undergraduate in Bangladesh from the University of Dhaka majoring in physics (2019). She did her M.S. with a thesis (2023) at Texas Tech University in Physics under the supervision of Dr. Jerzy Blawzdziewicz focusing on particle transport by cilia arrays in biological environment. She is currently doing research with Dr. Indrajit Srivastava as her advisor and her research focuses on designing and developing biomimetic nanoparticles for image-guided cancer interventions using both modeling and experimental tools.

**Xian Wu** is a chemical engineer with 6 years of experience in process development and optimization, specializing in magnetic materials and nanoparticle characterization. Currently pursuing a Ph.D. at The Ohio State University, Xian has authored 12 publications and presented at nine conferences. Xian is skilled in computational simulations, cell culture techniques, and material characterization, proficient in various analytical and statistical analysis tools, making significant contributions to both academic and industrial research.

**Poornima Ramesh Iyer** is a first-year Ph.D. student in Chemical Engineering at Ohio State University. She holds a Master's in industrial chemistry from the National University of Singapore and Technical University of Munich, and a Bachelor's in chemical engineering from the University of Nottingham. Her research interests include nanotechnology applications such as magnetic separation and lateral flow assays.

**Shahriar Mostufa** is presently pursuing a Ph.D. in the Electrical and Computer Engineering Department at Texas Tech University. He attained a B.Sc. degree in electrical and electronic engineering from Rajshahi University of Engineering and Technology (RUET), Bangladesh, in 2022. His ongoing research endeavors encompass dynamic domains including metamaterials, nano-photonics, optical and magnetic biosensors, magnetic particle imaging, wearable electronics, and spintronics devices, affirming his engagement with cutting-edge advancements in multiple disciplines.

**Stefano Ciannella** is a Ph.D. candidate at the Department of Chemical Engineering of Texas Tech University (USA). He holds a B.Sc. degree in chemical engineering from the Federal University of Campina Grande (Brazil) and two M.Sc. degrees in chemical engineering and industrial engineering from Texas Tech University and the Federal University of Paraiba (Brazil), respectively. His current research focuses on the study of functional nanomaterials to enhance separation processes and advance water remediation.

**Ioannis Karampelas** has a total experience of more than 20 years in CFD. Ioannis obtained his B.Sc. and M.Sc. degrees in chemical engineering at the National Technical University of Athens (Greece). In 2016, he obtained his doctorate in chemical engineering at the University at Buffalo (NY, USA). Immediately after, he worked at Flow Science Inc., the developer of the CFD software package FLOW-3D. Since 2019, he is currently a Senior Simulation Engineer at NEMAK USA. His current research interests include the applications of numerical methods in biological systems and novel nanoparticle-enabled treatment methods such as photothermal cancer therapy as well as the development of novel technologies such as additive manufacturing and point-of-care devices.

**Jeff Chalmers** is the Helen Kurtz Professor at The Ohio State University, awarded the 2023 Distinguished Scholar Award. He directed the Analytical Cytometry Shared Resource from 2001 to 2020. In over 35 years at Ohio State, he received the NSF Young Investigator Award, became a Fellow of the American Institute for Medical and Biological Engineering, and the AAAS. In 2014, he received the Cell Culture Engineering Award. He has published over 200 peer-reviewed articles in bioengineering, and over 100 of these papers, 10 patents, and one book, are in the area of magnetic cell separation. Professor Chalmers received his Ph.D. from Cornell University in 1988 and his B.S. in Chemical Engineering from U.C. Berkeley and a B.A. from Westmont College in 1983.

**Indrajit Srivastava** is a tenure-track assistant professor in the Mechanical Engineering department at Texas Tech University. He earned his master's and doctorate degrees in bioengineering from the University of Illinois at Urbana-Champaign (UIUC) in 2017, and 2020 respectively focusing on carbon dots for bioimaging and diagnostics. Subsequently, he did a joint postdoc in the Departments of Bioengineering and Electrical & Computer Engineering, at UIUC which focused on developing biomimetic nanoparticles for spectroscopic- and fluorescence image-guided cancer surgery. His research group focuses on creating advanced biomaterials inspired by nature and leveraging nanoengineering design principles for fluorescence/afterglow image-guided surgery, and disease diagnostics.

**Jenifer Gomez Pastora** obtained a B.Sc. and M.Sc. in chemical engineering and a B.Sc. in industrial engineering at the University of Cantabria (Spain). In 2018, she obtained her doctorate in Chemical Engineering at the same university. Afterward, she worked as a postdoctoral researcher in the Department of Chemical and Biomolecular Engineering at Ohio State University (USA). Since 2022, she is an assistant professor of chemical engineering at Texas Tech University (USA). Her current research activities include the development of cutting-edge magnetic technologies for several biomedical and biological applications, ranging from sensing to diagnosis and treatment.

**Kai Wu** obtained his Bachelor's degree in electrical engineering in 2013 from Northwestern Polytechnical University (China). He further pursued his Ph.D. degree in electrical engineering at the University of Minnesota (USA), completing it in 2017. From 2017 to 2020, he served as a postdoctoral fellow at the University of Minnesota, followed by a role as a Researcher 5 from 2020 to 2022. Presently, he holds the position of assistant professor at Texas Tech University. His research focuses on various areas including machine learning-assisted healthcare, neuromorphic computing, magnetic biosensors, magnetic nanomaterials, and magnetic particle imaging (MPI).